CENTRO DE INVESTIGACIÓN Y DE ESTUDIOS AVANZADOS
DEL INSTITUTO POLITÉCNICO NACIONAL

UNIDAD ZACATENCO
PROGRAMA DE DOCTORADO
NANOCIENCIAS Y NANOTECNOLOGÍA

“Síntesis por métodos químicos y caracterización de partículas micro/nanométricas y películas delgadas de Cu(In,Ga)Se_2”

Tesis que presenta:
LATHA MARASAMY

Para obtener el grado de:
Doctor en Ciencias

En la especialidad de
Nanociencias y Nanotecnología

Director de tesis: **Dr. Velumani Subramaniam**

México, Distrito Federal. Marzo, 2017

Resumen

En los últimos años, el campo de la energía fotovoltaica ha sido objeto de un enorme interés de investigación debido a la creciente demanda de energía y al cambio climático. En el presente escenario, los dispositivos fotovoltaicos se fabrican principalmente con silicio cristalino o películas delgadas de materiales inorgánicos absorbentes que podrían permitir una producción a gran escala debido al bajo costo de material. Entre las capas delgadas absorbentes, Cu (In, Ga) Se_2 (CIGSe) es uno de los materiales más prometedores debido a sus altas eficiencias y espesores de película inferiores (~ 1 µm). Sin embargo, la mayor eficiencia de las celdas solares de película delgada basadas en CIGSe se han fabricado utilizando costosas técnicas de vacío. Como alternativa, las técnicas de depósito basadas en soluciones han ganado mucha atención debido a sus ventajas tales como bajo costo y alto producción de material. En esta disertación, hemos desarrollado dos enfoques para preparar el material absorbente de CIGSe, empleando soluciones basadas en partículas submicrónicas y nanopartículas.

En el primer enfoque, las películas de CIGSe se prepararon con éxito a partir de partículas submicrónicas. Hasta donde sabemos, no hay ningún estudio previo en la literatura para la síntesis de partículas submicrónicas de CIGSe de una sola fase, a través de un proceso de calentamiento “one-pot”. Las partículas submicrométricas de CIGSe se caracterizaron por XRD, Raman, FE-SEM, EDS y UV-VIS-NIR para investigar diversas propiedades. La temperatura de reacción y el tiempo de reacción juegan un papel vital en la formación de CIGSe monofásico con composición controlada. Los núcleos de CuSe actúan como semilla y juegan un papel crucial durante la formación de partículas de CIGSe submicrónicas. Con los parámetros optimizados, la cantidad de precursores se aumentó hasta 10 veces para llevar a cabo una síntesis a gran escala. Además, se investigó la influencia de la concentración de Cu sobre las diversas propiedades del CIGSe, lo cual tiene un gran impacto en la formación de fases, el tamaño de partícula, la morfología de las partículas y le ancho de banda prohibida. Las pelıculas de CIGSe se prepararon usando una formulación de tinta basada en partıculas submicrométricas, por medio de un método de doctor blade. Las concentraciones de polvo de CIGSe y las temperaturas de recocido en aire fueron optimizadas, resultando en una superficie lisa y libre de grietas con un espesor de ~ 1 μm. Las películas de CIGSe recocidas en aire a 350^{0}C se utilizaron para el proceso de selenización. El proceso de selenización se realizó a diferentes temperaturas con y sin tratamiento de NaCl. Los estudios estructurales y morfológicos mostraron un incremento en el tamaño de los cristales y granos después de la selenización. Las películas de CIGSe tratadas con NaCl mostraron propiedades eléctricas y optoelectrónicas mejoradas. La resistividad de las películas de CIGSe disminuyó y la concentración de portadores aumentó en un orden de magnitud. La película de CIGSe tratada con NaCl exhibió una alta fotoconductividad de 4.39 veces.

En el segundo enfoque, las películas de CIGSe se prepararon a partir de una solución de nanopartículas. Las nanopartículas de CIGSe se sintetizaron satisfactoriamente mediante un proceso de inyección en caliente. Se investigaron las propiedades estructurales, morfológicas, de composición y ópticas de las nanopartículas de CIGSe sintetizadas. La incorporación de Ga estuvo fuertemente influenciada por la temperatura de reacción. El tiempo de reacción juega un papel determinante en la formación de CIGSe monofásico con composición controlada. Se estudió el mecanismo de formación de nanopartículas de CIGSe monofásicos por la incorporación gradual de iones de In^{3+} y Ga^{3+} en la red cristalina β-CuSe. Las películas de CIGSe sin tratamiento se prepararon a partir de tinta de nanopartículas usando un método de revestimiento de doctor blade. Las películas de CIGSe se sometieron a un recocido en aire a 350 ^{0} C seguido de una selenización a 500^{0}C con y sin tratamiento de NaCl. Se investigaron diversas propiedades de las películas de CIGSe. Todas las películas de CIGSe mostraron bajas movilidades y alta resistividades. Por lo tanto, a partir de ambos enfoques, encontramos que las propiedades de las películas de CIGSe preparadas a partir de nanopartículas son muy inferiores a las partículas submicrónicas.

Palabras clave: CIGSe, partículas submicrónicas, nanopartículas, películas delgadas, concentración de Cu, contenido de Ga, método one-pot , doctor blade, tratamiento con NaCl, fotoconductividad.

Abstract

In recent years, the field of photovoltaics has been attracted tremendous research interest due to increasing energy demand and climate change. In the present scenario, photovoltaic devices are majorly fabricated with either crystalline silicon or thinner films of inorganic absorber materials which could allow large scale production due to their low material cost. Among other absorber thin layers, $Cu(In,Ga)Se_2$ (CIGSe) is one of the most promising material due to their high efficiencies and lower thicknesses (~1 µm). However, the highest efficiency of CIGSe thin film solar cells have been fabricated using expensive vacuum techniques. As an alternative, solution-based deposition techniques have gained much attention due to their advantages such as low-cost and high-throughput. In this dissertation, we have developed two approaches to prepare CIGSe absorber material employing solution based submicron and nanoparticles.

In the first approach, the CIGSe films were successfully prepared from as-synthesized submicron particles. To the best of our knowledge, there is no previous study in the literature for synthesizing single phase CIGSe submicron particles via a one-pot heating-up process. The synthesized CIGSe submicron particles were characterized by XRD, Raman, FE-SEM, EDS and UV-VIS-NIR analysis to investigate various properties. The reaction temperature and reaction time plays a vital role on formation single phase CIGSe with controlled composition. The CuSe nuclei acts as seed and plays a crucial role during the formation CIGSe submicron particles. With the optimized parameters, the amount of precursors were increased to 10-fold to carry out for large scale synthesis. Furthermore, the influence of Cu concentration on the various properties of CIGSe was investigated which has a great impact on phase formation, particle size, particles morphology and optical band gap energy. The CIGSe films were prepared using ink formulation of submicron particles by doctor blade method. The CIGSe powder concentrations and air annealing temperatures were optimized resulting to smooth and crack free surface with the thickness of ~ 1µm. The CIGSe films annealed at 350°C in air were used for selenization process. The selenization process was performed at different temperature with and without NaCl treatment. The structural and morphological studies showed an increment in the crystallite and grain size after selenization.

The NaCl treated CIGSe films showed enhanced electrical and opto electronic properties. Resistivity of CIGSe films decreased and carrier concentration increased by one order magnitude. The NaCl treated CIGSe film exhibited high photoconductivity of 4.39-fold.

In the second approach, the CIGSe films were prepared from nanoparticles solution. The CIGSe nanoparticles were successfully synthesized by hot injection process. The structural, morphological, compositional and optical properties of synthesized CIGSe nanoparticles were investigated. The incorporation of Ga was strongly influenced by reaction temperature. The reaction time plays a determining role on the formation of single phase CIGSe with controlled composition. We studied the formation mechanism of single phase CIGSe nanoparticles by gradual incorporation of Ga^{3+} and In^{3+} ions in the β-CuSe crystal lattice. The CIGSe films were prepared from nanoparticles ink using doctor blade coating method. The as-prepared CIGSe films were subjected to air annealing at 350°C followed by selenization at 500°C with and without NaCl treatment. Various properties of CIGSe films were investigated. All the CIGSe films showed low mobility and high resistivity. Therefore, from both the approaches, we found that the properties of CIGSe films prepared from nanoparticles are far inferior to submicron particles.

Keywords: CIGSe, submicron particles, nanoparticles, thin films, Cu concentration, Ga content, one-pot heating-up, doctor blade, NaCl treatment, Photoconductivity.

Acknowledgement

It is a great opportunity for me to work as a doctorate student in Center for Research and Advanced Studies of the National Polytechnic Institute (CINVESTAV-IPN), Zacatenco-Mexico. I had a wonderful time over the past four years and would like to express my gratitude to all those who helped me throughout my research work.

First and foremost, I would like to express my sincere gratitude to my supervisor, Dr. Velumani Subramaniam for guiding me throughout the tenure and for encouraging thoughts. His insight, constant support, valuable suggestions, and advices has helped me greatly throughout the completion of my research.

I wish to express my gratefulness to the committee members and external examiner: Dra. María de la Luz Olvera Amador, Dr. Gabriel Romero Paredes Rubio, Dr. Mauricio López Ortega, from Solid State Electronics Section (SEES), Department of Electrical Engineering, CINVESTAV-IPN and Dr. Jose Chavez Carvayar, IIM-UNAM, Mexico City for their support, encouragement, valuable time spent for meetings and scientific discussions.

I extend my sincere thanks and gratitude to Dr. Osvaldo Vigil-Galán, Dr. Fabián Andrés Pulgarín Agudelo and Ms.Miriam Nicolas Departamento de Física, Instituto Politécnico Nacional, Mexico for their support and allowing me to use their selenization furnace.

I am thankful to Dr. Jose Gerardo Cabanas Moreno, coordinator in Nanoscience and Nanotechnology program for his complete support. I wish to thank Nanoscience and Nanotechnology program secretaries especially Alma Mercedes Zamudio Martínez, Jessica Marquez Duenas, María Ofelia Muñoz Ramírez for their continuous help in many things. I would like to thank Oscar Ivan Buendia Montano, Department of Becas y Estímulos for his valuable support in processing the scholarship and conference commission documents which made me comfortable to carry out my various documentation works.

Thanks to all the professors and secretaries in SEES and nanoscience and nanotechnology for their hearty smile and care, this made me comfortable to work in these department. I would also like to thank auxiliaries, technicians and some of the professors from various departments and institutes for their collaboration for characterizing the samples. I would like to thank Dr. Jaime Santoyo Salazar (Physics), M. en I. Alvaro Ángeles Pascual, Dr. Daniel Bahena Urruibe (LANE, HRTEM analysis), Dr. Jorge Roque De La Puente (LANE, FESEM and EDS analysis), Prof. Sergio Tomas (Physics, XPS analysis), M. en C. Miguel Galván Arellano (SEES, Raman spectroscopy and I-V measurement), Miguel Ángel Luna Arias (Hall Effect measurement), Ing. Angela Gabriela López Fabián (SEES, UV-Visible-NIR spectroscopy), M. en C. Adolfo Tavira Fuentes (SEES, XRD analysis), Ing. Miguel Angel Avendaño Ibarra (SEES, Thickness measurements), Norma Iris (SEES, Thermal evaporation of Au contacts), Josué Romero Ibarra (UNAM, FE-SEM) and Marcela Guerrero (Physics, XRD powder analysis).

I would like to acknowledge for the doctorate scholarship awarded by the Consejo Nacional De Ciencia Y Tecnología (CONACYT). And, I also thank Sistema de Información Académica (SINAC) from CINVESTAV-IPN for financially supporting for the conferences like IMRC, Cancun and MRS, USA.

I wish to thank Mrs. Malathy Velumani for her continuous encouragement and care. I also want to thank my group members Dr. Pablo Itzam Reyes, Dr. Rohini Mohan, Dr. Goldie Oza, Dr. Victor Ishrayelu, M. en C. Aruna Devi Rasu Chettiar and Ravichandren Manisekaren who took part in my work by creating a unique and encouraging atmosphere. I sincerely extent my thanks to Dr. Pablo Itzam Reyes for his technical discussion. I wish to express my special thanks to my friend M. en C. Aruna Devi Rasu Chettiar; I can’t even imagine this without her support towards my academic journey.

Last but not least, I want to express my deepest gratitude to my parents and my brother who have been supporting and encouraging me all the time. With their consistent love, support, and prayers, I could be able to go through all the hardships. Above all, thanks to the Almighty for giving me strength to manage all the ups and downs throughout my life.

Contents

Page no

1. Introduction and background 1

1.1. Motivation

List of tables

List of figures

List of Acronyms/Abbreviations

Acronym	**Definition of Acronym**
PV	Photovoltaic
c–Si	Crystalline silicon
µm	Micrometer
$Cu(In,Ga)Se_2$ (CIGSe)	Copper indium gallium diselenide
CdTe	Cadmium telluride
a–Si	Amorphous silicon
$CuInSe_2$ (CISe)	Copper indium diselenide
Δ	Tetragonal distortion
ODC	Ordered defect compound
V_{oc}	Open circuit voltage
V_{Se}	Se vacancy
V_{In}	In vacancy
VBM	Valence band maximum
Na	Sodium
PL	Photoluminescence
DLTS	Deep level transient spectroscopy
V_{Cu}^{-}	Cu-vacancies
KCN	Potassium cyanide
VBM	Valence band maximum
Mo	Molybdenum
FASST	Field-Assisted Simultaneous Synthesis and Transfer
PVD	Physical vapour deposition
RTP	Rapid thermal processing
ISET	International Solar Electric Technology Inc
NaOH	Sodium hydroxide
NHE	Normal hydrogen electrode
OLA	Oleylamine

XRD	X-ray diffraction
TEM	Transmission electron microscopy
I-V	Current-voltage
SLG	Soda lime glass
Tg	Transition temperature
L	Crystallite size
FWHM	Full Width Half Maximum
RS	Raman spectroscopy
FE-SEM	Field emission scanning electron microscopy
EDS	Energy dispersive X-ray spectroscopy
HR-TEM	High resolution transmission electron microscopy
XPS	X –ray photoelectron spectroscopy
ESCA	Electron spectroscopy for chemical applications
UV-Vis-NIR	Ultraviolet-visible-near infrared
A	Absorbance
Cu	Copper
OVC	Ordered vacancy compound
A	Bond-stretching central force constant
CTE	Co-efficient of thermal expansion
An	Annealed
Se	Selenized
Au	Gold
NaCl	Sodium chloride

Chapter 1

Introduction

1.1. Motivation

One of the major environmental concerns of today is the emission of greenhouse gasses like CO_2. Climate scientists expect that the average global surface temperature could rise 0.6-2.5°C in the next fifty years, and 1.4-5.8°C in the next century, due to this emission [1]. Such an increase will have a huge impact on the environment. To avoid an even further rise in the temperature, we have to stop exhaust greenhouse gasses in the quantities we do today. The reason for a large amount of greenhouse gasses emitted into the atmosphere is that nearly 80 % of the energy generation worldwide originates from fossil fuels. In the long term, there are three main alternatives to reduce the CO_2 emissions, without reducing the global energy consumption:

1. **Nuclear power**: Today we have around 400 nuclear power plants around the world. With about 5000 the energy-demand of today could be covered.
2. **Carbon sequestration**: We could continue to use our reserves of fossil fuels if we take care of the emissions and store them in existing cavities in the earth.
3. **Sustainable energy:** By a massive effort in developing existing and new technologies for sustainable energy generation, we can generate all the energy needed with these technologies.

The first alternative is not very tempting from a risk point of view. It is also a time limited solution since the amount of uranium is finite. The second alternative might be possible but is no sustainable solution. The concept of carbon sequestration is also not tested on large scale and it is not for certain that it will work. If sustainable energy solutions could replace the existing non-sustainable energy generating technologies, it would be long term beneficial for all of us. The irradiation from the sun, reaching our globe is in relation to our energy demand, very high (in the order of 10,000 times higher). With solar cells, this irradiation can, with no material consumption, directly be converted into the highest form of energy – electricity!

1.2. Solar cells

1.2.1. Operation of solar cells

A solar cell is a device which directly converts light energy into electrical energy. A typical solar cell structure is shown in **Fig. 1.1**. The operation of a solar cell involves the following steps:

(a) Absorption of photons (solar radiation)
(b) Generation of electron-hole pairs,
(c) Separation of these electron-hole pairs by some internal mechanism and
(d) A collection of electron-hole pairs by an external circuit.

A semiconductor material can absorb photons with energy equal to or greater than the bandgap. Upon absorption of photons, the electrons in the valance band jump to the conduction band of absorber material i.e. creation of electron-hole pairs. The essential part of a solar cell (**Fig. 1.1**), is the p-n-junction. It consists of two semiconductor layers, one n-doped layer with an excess of free electrons which originate from dopant atoms which can easily free one electron, and one p-doped layer where holes i.e. absence of electrons are in excess. The holes originate from ionized dopant atoms which can easily accept one extra electron. In an n-type material, electrons act as mobile charge carriers, whereas holes act as charge carriers in the p-type material. When a junction is formed between two layers of different type of doping, diffusion makes electrons travel from the n-type side to the p-type side, while ionized dopant atoms are left. Consequently, a region depleted of free charge carriers is created and an electric field is built up by the ionized dopant atoms on the p and n-doped sides respectively. Thereby an electrostatic potential is formed between the quasi-neutral parts of the n-type and the p-type semiconductors. The electric field is the engine in the photovoltaic cell and will separate positive and negative free charge i.e. electron-hole pairs created by the absorption of light. A number of absorbed photons and thereby created electron-hole pairs will depend on the thickness of the semiconductor and its absorption coefficient. If an electron-hole-pair is created in, or within a diffusion length of the depletion region, the electron (on the p-type side) or the hole (on the n-type side) will drift in the electric field, and travel to the opposite side. In steady state condition, when the light is shining onto the solar cell, many electron-hole-pairs are generated and separated by the electric field causing a build-up of negative charge on the n-side and positive charge on the p-side. To make use of the p-n diode as a power generating solar cell, a load may be connected between the n-side and the p-side and current will flow through the load. To collect the current in an efficient way, both sides of the p-n diode must have contact layers with good ohmic contacts to the semiconductor materials. For the back side, which does not need to be optically transparent, this is made by a layer of metal, the back contact. The contact on the front side must be both electrically conducting and optically transparent and is commonly called a window layer [2,3].

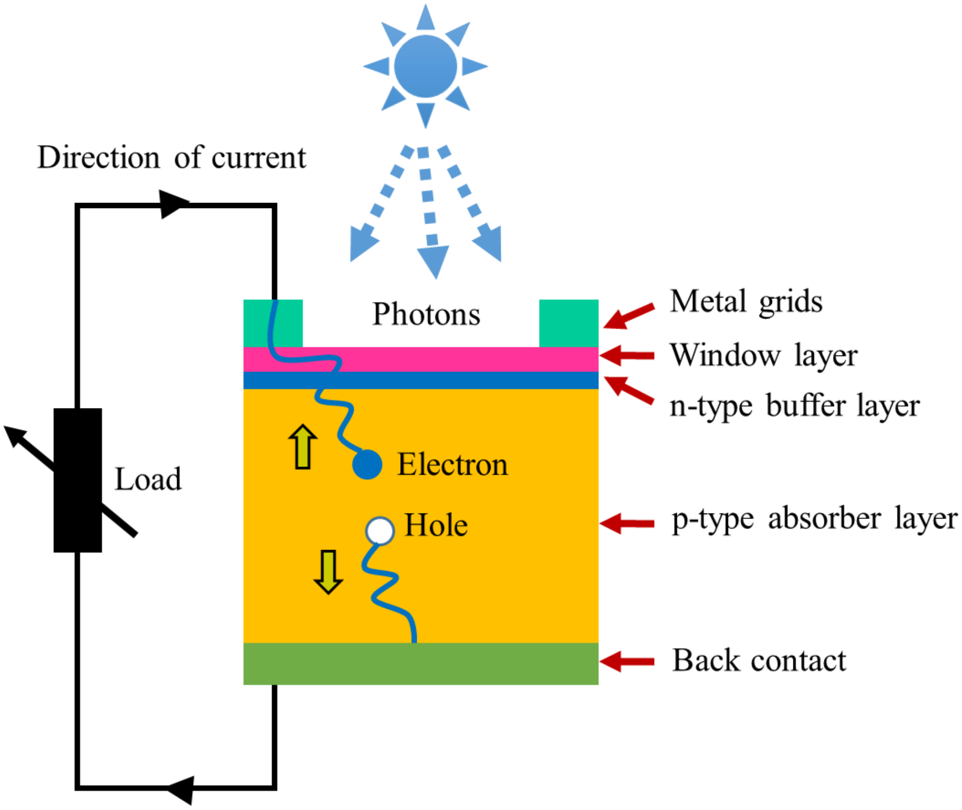

Fig. 1.1. A very simplified picture of solar cell device at work. Photons (quanta of light) from the sun travels through the window layer of the solar cell and further down into the absorber. Somewhere in the absorber, the photon may excite an electron-hole pair. The

electron and the hole will be separated by the internal electric field in the p-n junction. Due to the separation of the different charges, a voltage is built up. The more photons that are being absorbed, the more electric current will the solar cell produce when connected to a load.

1.3. Development of Photovoltaic technology

As explained in the previous section, photovoltaic is the process of converting light energy to electrical energy by generating current and voltage and the device used to perform this action are called a Solar cell. Edmund Becquerel was first reported such action when he observed the production of current and voltage by illuminating a silver chloride electrode immersed in an electrolytic solution in 1839 **[4]**. After that, it took nearly 100 years to fabricate a real solar cell when a solar cell based on a p-n junction was produced at the Bell labs in 1953 **[5]**. The efficiency of that cell was around 6% and the semiconductor used to manufacture this solar cell was single crystal Si. Since that day, many different semiconductors and different techniques are used to make solar cells and classified as First, Second and Third generation of photovoltaic (PV) technology.

The First generation of PV is based on the crystalline silicon (c–Si) semiconductor and these solar cells have not only high efficiency (25%) **[6]** but also high cost. Crystalline Si is an indirect band gap (≈ 1.17 eV) semiconductor, which means they absorb the sunlight poorly. And, it requires a thickness of the order of hundred micro-meters (µm) to absorb most of the incident photons. The c-Si-based solar cells either use monocrystalline (single crystal) Si produced by slicing wafers of around 250 thick from a high-purity single crystal ingot or multi-crystalline silicon produced by sawing a cast block of silicon.

The second-generation PV also called thin film photovoltaic is based on direct band gap semiconductors like polycrystalline copper indium gallium diselenide ($Cu(In, Ga)Se_2$), cadmium telluride (CdTe) and amorphous silicon (a–Si). Direct band gap semiconductors have a high absorption coefficient, which means most of the light is absorbed by few µm thick material. Also, these thin films can be deposited on many different substrates like glass, stainless steel etc.. These advantages can help in faster manufacturing, with less material and energy usage, which reduces the cost of manufacturing and production of the solar cells.

The third generation of PV including dye-sensitized solar cells, organic polymer-based photovoltaics, multi-junction solar cells have been emerged with the aim of providing higher efficiency while maintaining the low cost offered by second-generation solar cells. **Table 1.1** gives an overview and comparison of current PV technologies. The multi-junction solar cells with five junctions and three junctions are currently showing highest efficiencies, 38.8 and 37.9 % respectively. Presently, these solar cells find application in space for satellites. The high production cost of this complex technology limits its extensive usage for terrestrial applications. While, considering cost effective thin film technologies such as CIGSe and CdTe based solar cells has attained 22.6 and 22.1 % efficiency in laboratory scale **[7,8]**, which is equal to the efficiency of polycrystalline Si solar cells. Both, CIGSe and CdTe have temperature resistance higher than Si-based solar cells and have better performance in shades. However, thin film CIGSe solar cells have a few advantages over CdTe. Primarily, CIGSe is slightly more efficient than CdTe in converting sunlight into usable energy. Secondly, they use less amount of toxic heavy metal cadmium.

Table 1.1. Efficiency and solar cell parameters of current PV technologies **[9]**.

Classification	**Efficiency (%)**	**Area (cm^2)**	**Voc (V)**	**Jsc (mA/cm^2)**	**Fill factor (%)**	**Description**
Silicon						
Crystalline Si	25.6±0.5	143.7	0.740	41.8	82.7	Panasonic
Multicrystalline Si	21.25±0.4	242.7	0.667	39.8	80.0	Trina Solar
Thin film minimodule Si	10.5±0.3	94	0.492	29.7	72.1	CSG solar
III-V cells						
GaAs thin film	28.8±0.9	0.992	1.122	29.68	86.5	Alta devices
GaAs	18.4±0.5	4.011	0.994	23.2	79.7	RTI
InP crystalline	22.1±0.7	4.02	0.878	29.5	85.4	Spire

Thin film Chalcogenide						
CIGSe (cell)	21.0±0.6	0.992	0.757	35.70	77.6	Solibro
CIGSe (minimodule)	18.7±0.6	15.89	0.701	35.29	75.6	Solibro
CdTe (cell)	21.0±0.4	1.062	0.875	30.25	79.4	First solar
Amorphous/ microcrystalline Si						
Si (amorphous)	10.2±0.3	1.001	0.896	16.36	69.8	AIST
Si (microcrystalline)	11.8±0.3	1.044	0.548	29.39	73.1	AIST
Dye sensitised						
Dye	11.9±0.4	1.005	0.744	22.47	71.2	Sharp
Dye minimodule	10.7±0.4	26.55	0.754	20.19	69.9	Sharp
Organic						
Organic thin-film	11.0±0.3	0.993	0.793	19.40	71.4	Toshiba
Organic minimodule	9.7±0.3	26.14	0.806	16.47	73.2	Toshiba
Perovskite						
Perovskite thin film	15.6±0.6	1.020	1.074	19.29	75.1	NIMS
Multijunction						
Five junction cell (bonded)	38.8±1.2	1.021	4.767	9.56	85.2	Spectrolab
InGaP/GaAs/InGaAs	37.9±1.2	1.047	3.065	14.27	86.7	Sharp
GaInP/Si (mech.stack)	29.8±1.5	1.006	1.46	14.1	87.9	NREL
a-Si/nc-Si/nc-Si (thin-film)	13.6±0.4	1.043	1.901	9.92	72.1	AIST
a-Si/nc-Si (thin-film cell)	12.7±0.4	1.000	1.342	13.45	70.2	AIST

1.4. History of Cu(In,Ga)Se_2 (CIGSe) thin film solar cells

During the initial years of thin-film solar cells evolution, considerable efforts were made for research, development, and commercialization of Cu_2S/CdS cells. However, these efforts had to be abandoned as these cells had instability problems caused mainly by copper migration. This led to the evolution of $CuInSe_2$ thin-film solar cells. The presence of trivalent indium seems to bind the Cu tightly in the chalcopyrite lattice, suppressing the copper migration degradation mechanism that affects the Cu_2S/CdS cell. Since then, I-III-VI_2 compounds are proving to be promising materials to meet the world energy requirement. $CuInSe_2$ (CISe) and its alloys with Ga and S have shown highest conversion efficiency of 19.9% [10] and a reasonable stability. CISe has a direct bandgap of 1.02 ± 0.01 eV [11]. The band gap of CISe can be increased continuously over a wide range up to 1.68 eV by increasingly substituting Ga for In where the band gap increases as a function of Ga content [12,13]. Similarly, the band gap can also be increased by substituting S for Se up to 2.4 eV.

1.5. Material properties of CIGSe

1.5.1. Structural properties

$CuInSe_2$ and $CuGaSe_2$, the materials that form the alloy Cu(In, Ga)Se_2 (CIGSe), belong to the semiconductor I-III-VI_2 material family that crystallizes in the tetragonal chalcopyrite structure and is stable from room temperature up to 810^oC [14]. The chalcopyrite structure of CIGSe is similar to the ZnS structure (Fig. 1.2.) in which Zn atoms are replaced alternatively by Cu (I) and In (III) atoms. Each Cu and In atom has four bonds with Se (VI) atom. In turn, each Se atom has two bonds to Cu and two more to In. Since the strength of the I-VI and III-VI bonds are in general different, the ratio of lattice constants c/a is not exactly 2, where 2 is c/a of undisturbed crystal structure [15]. There is a distortion in the lattice structure which is known as tetragonal distortion (Δ) and is defined as $\Delta = 2 - c/a$. Δ present linear dependence on the Ga content, x, in the $Cu(In_{1-x}Ga_x)Se_2$. Δ is negative for $x < 0.23$ and positive for $x > 0.23$. It could be due to changes in electronegativity of In and Ga [16]. The system of Cu- chalcopyrite covers a wide bandgap of energies from 1.02 eV in $CuInSe_2$ up to 2.4 eV in $CuGaS_2$ covering most of the visible spectrum.

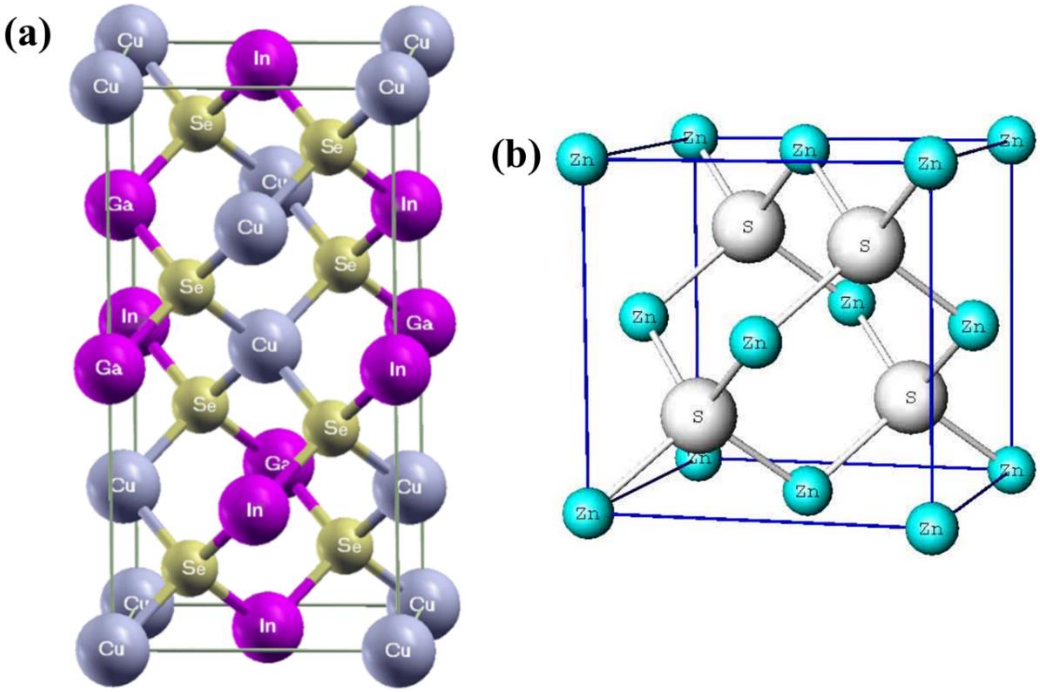

Fig. 1.2. (a) CIGSe chalcopyrite structure and (b) ZnS Zinc blend structure.

1.5.1.1. Phase diagram

It is essential to obtain α phase in CIGSe layers due to required photovoltaic characteristics of this phase. The phase diagram provides the alloy composition, the allowed deviation from stoichiometry and the process temperature for producing a good quality absorber layer. Fig. 1.3. shows a ternary elemental composition diagram of Cu, In, and Se at room temperature. CIS absorber grown with an excess supply of selenium has a composition on or near the tie line of Cu_2Se and In_2Se_3. It is interesting to note that the ordered vacancy compounds (OVC) such as $CuIn_3Se_5$, $Cu_2In_4Se_7$, and $Cu_3In_5Se_9$ lie on the same tie line and have the same chalcopyrite structure. The ordered vacancy compounds are formed by regular arrangements of point defects in the chalcopyrite crystal structure. This complex ternary diagram can be reduced to a simpler pseudo-binary phase diagram along the tie line between Cu_2Se and In_2Se_3 [17]. As can be seen from the phase diagram, the α-phase ($CuInSe_2$) lies in a very narrow range from 24 to 24.5% of copper at room temperature. At growth temperature between 500°C and 550°C, the α-phase exists in the range from 22 to 24.5 at% Cu. According to the phase diagram, the cooling off slightly Cu-poor composition indicates the presence of additional β-phase ($CuIn_3Se_5$) also known as ordered vacancy compound. The OVC is builted by ordered arrays of defect pairs of Cu vacancies and indium on copper anti-sites. Some groups have reported the formation and benefits of having such an OVC on top of the absorber layer [18]. This layer has a bandgap of 1.3 eV, which is higher than the bulk CISe bandgap of ~1 eV. Higher bandgap semiconductor at the metallurgical junction helps in increasing open circuit voltage (V_{oc}) [19]. When the absorber layer is grown in Cu-rich regime an additional phase, $Cu_{2-x}Se$ is formed. This layer is metallic in nature and has to be removed before depositing the heterojunction partner. Another phase that occurs in the phase diagram is the δ-phase called sphalerite which is stable at high temperature. A congruent solid-solid phase transition occurs at 810°C between the disordered δ-phase and the ordered chalcopyrite α-phase. The reason to grow $CuInSe_2$ and its alloys with gallium and sulfur in a copper poor regime is evident from the phase diagram (Fig. 1.4.) as the homogeneity of the α-phase extends over a range of composition towards copper poor compositions at the growth temperature while does not extend to the copper-rich side and not even the stoichiometric composition of 25 at % Cu [14].

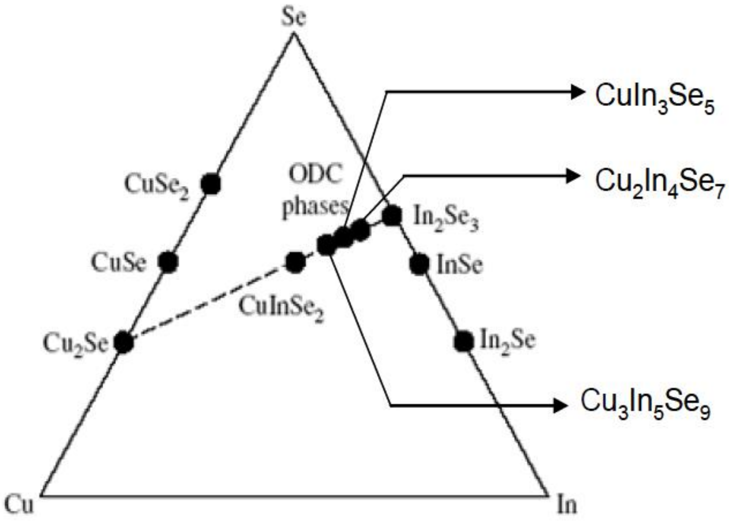

Fig. 1.3. Ternary elemental composition diagram of Cu-In-Se [17].

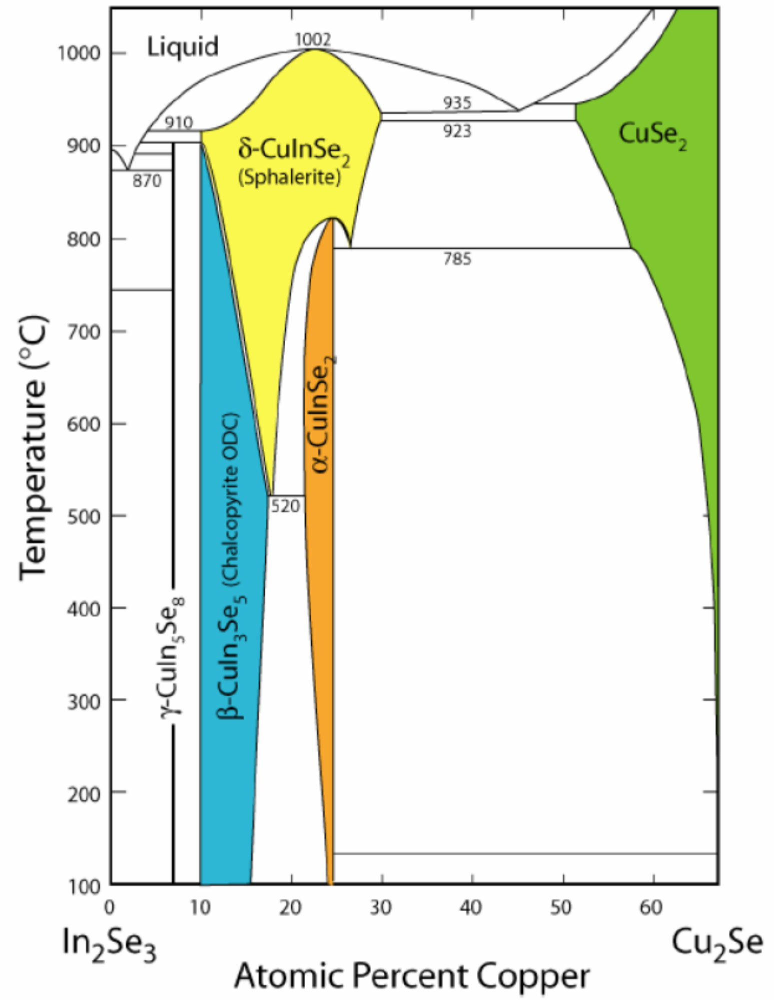

Fig. 1.4. Pseudo-binary phase diagram along the tie line between Cu_2Se and In_2Se_3 represented in terms of Cu atomic % [17].

1.5.1.2. Intrinsic defect doping of CIGSe

Small deviations from stoichiometry cause drastic changes in the electronic properties of binary compounds. The ternary compounds $CuInSe_2$, are considerably more tolerant to stoichiometric deviations. The Cu content of device-quality CISe or CIGSe absorbers varies typically between 22 and 24 at% Cu. Thus, these films are markedly Cu-poor but maintain excellent semiconducting properties. In terms of point defects, a non-stoichiometry of 1% would correspond to a defect concentration of roughly 10^{21} cm^{-3}. This is approximately five orders of magnitude higher than the acceptable density of recombination centres in a photovoltaic absorber material and still four orders of magnitude higher than the maximum net doping concentration of ~10^{17} cm^{-3} that have been indicated to be useful for the photovoltaic active part of a solar cell. The charge density in the space charge region of any photovoltaic device must not exceed 10^{17}–10^{18} cm^{-3}. Otherwise, tunnelling enhanced recombination would significantly decrease the open circuit voltage of the solar cell. In fact, in Cu-chalcopyrite semiconductors, this limit appears to be close to few times 10^{17} cm^{-3}. CIGSe absorber material in the highly efficient cells has a net charge density of few times 10^{16} cm^{-3} **[20]**.

Even if a degree of compensation of 99% is allowed, the respective densities of donors and acceptors would be only in the 10^{19} cm^{-3} range. Thus, the virtual number of defects related to off-stoichiometry has to be reduced to reasonable scale that is compatible with the good electronic quality required to build a photovoltaic device **[20]**. The most important characteristic of CIGSe material is to accommodate a large compositional deviation without an appreciable change in the electronic properties. Highly efficient solar cells can be fabricated with Cu/(In+Ga) ratio of 0.7 to slightly less than 1. This phenomenon can be explained on the basis of defect chemistry of CIS. It has been shown that the formation energy of defects such as copper vacancies V_{Cu} and defect complexes such as two copper vacancies in combination with indium on copper antisite ($2V_{Cu}$+In_{Cu}) is low **[21]**. V_{Cu} is a shallow acceptor that contributes to the p-type conductivity of CIGS. The $2V_{Cu}$+In_{Cu} defect prevents degenerate doping in the indium-rich material. Isolated In_{Cu} acts as a deep double donor while the combination with $2V_{Cu}$ has no deep level and is electrically neutral. At high concentrations of $2V_{Cu}$+In_{Cu} complexes, their formation energy is further reduced. Thus the creation of such defect complexes can compensate for Cu-poor/In-rich composition of CIGS without adverse effects on the photovoltaic properties. Doping of the CIGS semiconductor is controlled by intrinsic defects. Samples with p-type conductivity are grown if the material is copper poor and annealed under high Se vapor pressure, whereas a Cu-rich material with Se deficiency tends to be n-type **[22,23]**. Thus Se vacancy (V_{Se}) is considered to be the dominant donor in n-type CIGS and also compensating donor in p-type CIGS while V_{Cu} is dominant acceptor in Cu-poor p-type material. The cu-poor material has In_{Cu} antisite donor defects along with V_{Cu} acceptors, resulting in heavily compensated p-type material limiting the acceptor density to non-degenerate levels. In the case of excess Cu, dominant defects are Cu_{In} antisite and In vacancy (V_{In}) acceptors, both of which contribute to a highly p-type material.

1.5.2. Optical properties

1.5.2.1. Influence of Ga content

For CISe, it has been demonstrated that the absorption co-efficient can be written as [24]:

$$\propto (h\nu) = \frac{A}{h\nu}\left(h\nu - E_g\right)^{\frac{1}{2}} \quad ---\rightarrow 1.1$$

where α is the absorption coefficient at a photon energy of hυ, A is a constant and Eg is the band gap. **Equation 1.1** shows in the semiconductor CISe, the band gap is due to the direct allowed transition between parabolic bands [24]. Thus CISe is a direct band gap semiconductors and the band gap is tuned from 1.04 to 1.68 eV, depending on the Ga substitution [12,13]:

$$E_g = (1-x)E_g(CISe) + xE_g\,(CGSe) - bx(1-x) \quad ---\rightarrow 1.2$$

where x is the Ga/(In+Ga) ratio, E_g is the band gap of CISe, and CGSe and b is the optical bowing parameter. Generally, the bowing parameter lies between 0.15-0.24 eV [21]. Optical bowing coefficient results from the difference of volume deformation potential of the constituent elements and coupling of folded states through the perturbation potential, the difference between the potential of CIGSe alloy and the average potential of the constituents, ΔV. Perturbation potential is affected by the chemical difference between In and Ga atoms and by the mismatch in the size of In and Ga atoms. The theoretical studies carried out by S.H.Wei [25] has shown that the increase in bandgap upon addition of Ga is due to the upward movement of conduction band minimum resulting from the ΔV induced interband coupling within the conduction band and valance band. According to theoretical calculations, the bandgap of CIGSe for achieving highest efficiency should be 1.4 eV as spectral energy distribution of solar light is maximum at this value [26]. CIGSe attains this bandgap when Ga/(In+Ga) =0.6 [27]. However, the maximum experimental efficiency of CIGSe solar cell reported so far uses Ga/(In+Ga) =0.3 corresponding to the bandgap of 1.1 eV. The efficiency of CIGSe solar cells reduces when Ga/(In+Ga) > 0.3 [10]. The discrepancy between theoretical and experimental Ga/(In+Ga) values is not completely explained so far.

Due to its direct band gap, the absorption in the CIGSe is very high and most of the photon are absorbed by a few µm thick CIGSe. The high absorption coefficient, for example, 10^5 cm^{-1} at 1.4 eV of photon energy [28], makes CIGSe a suitable absorber layer for solar cell application.

1.5.2.2. Influence of Cu content

The impact of a variation of the Cu content in CIGSe is considered. Such a variation may affect the doping density, as well as the band structure. According to several calculations, the Cu *d* orbital forms an antibonding state with the Se *p* orbital which is responsible for the energetic level determining the maximum of the valence band [29–31]. The bandgap of the CIGSe decreases as Cu content increases. This effect has been explained by the p-d hybridization of Cu and Se atoms [32–34]. Specifically, in CIGS based materials, the interaction between Cu 3d and Se 4p states moves the energy position of the valence band maximum (VBM) toward higher energy, leading to the Eg shrinkage. In contrast, when the Cu content is low, the p-d coupling effect becomes weaker and Eg widening occurs due to the downward shift of the VBM position.

1.5.3. Role of sodium (Na)

The soda-lime glass substrate was shown to beneficially affect the conversion efficiency of the solar cells, especially in the case of CIGSe thin-film solar cells [35]. It became evident, that the Na within the soda-lime glass is responsible for this effect. During the deposition of the absorber, Na diffuses out of the substrate through the Mo layer into the absorber. It was found that this induces larger grain sizes as well as a smaller resistivity of the absorbers [36–40]. Conductivity, photoluminescence (PL) and deep level transient spectroscopy (DLTS) measurements suggest an increase of the p-type doping induced by Na, either through direct doping or indirectly by passivating donors and additionally, a passivation of trap states deep within the band gap [39,41,42]. Possible mechanisms are

Na occupying Cu-vacancies (V_{Cu}^{-}) thereby suppressing the compensating effect of In^{2+}_{Cu} which acts as a donor or the suppression of the formation of (V_{Cu}^{-} -V_{Se}^{2+}) defect complexes [39]. It is still unclear if the beneficial effect occurs due to a different absorber growth induced by Na or simply by an increased p-type doping of the absorber independent from growth.

Experiments with post absorber growth deposition of Na show a similar improvement of the solar cell performance and suggest that the change of the absorber growth conditions play a minor role compared with the effect of increased p-type doping [43,44].

Selenization of the film containing sodium results in the formation of Na_2Se_x compounds that retard the growth of the CIGS phase, thereby incorporating relatively more selenium in the film [45]. Thus, the number of compensating donors are reduced by filling selenium vacancies, V_{se} and therefore, increasing the p-type conductivity. Sodium also replaces In_{Cu} antisite defects further reducing the compensating donors [46]. Apart from reducing the compensating donor sodium also replaces copper vacancies, thereby reducing the formation of ordered defect compound. Sodium has also been shown to passivate the surface and grain boundaries by promoting incorporation of oxygen [47]. Sodium promotes of increase in grain size and preferred (112) orientation of CIGS films [48]. Although in some studies sodium did not affect the grain-size of the CIGS film or even reduced the grain size [38]. The overall effect of sodium incorporation during grain growth is an increase in efficiency by enhancements of fill factor and open circuit voltage. The addition of sodium also results in a Cu-poor film with higher charge carrier mobility. This helps in the fabrication of higher efficiency cells without potassium cyanide (KCN) treatment.

1.6. Goals and Objectives

The goals of this thesis are

- Synthesis of CIGSe particles by two different processes such as one-pot heating-up and hot injection process.
- Study the influence of grain size on the properties of CIGSe films.

- ◆ Study the influence of heat treatments and Na content on the properties of CIGSe films.

To accomplish these goals, this research work is carried out focussing on the following objectives

- ✱ Optimization of synthesis parameters for both process to obtain pure phase CIGSe particles with controlled composition.
- ✱ Formulation of CIGSe ink using particles prepared by two different processes.
- ✱ Preparation of CIGSe films by doctor blade method.
- ✱ The heat treatments performed for as-prepared as well as NaCl-treated CIGSe films for different temperatures.

1.7. Organization of thesis

The present thesis is divided into 7 chapters.

Chapter 1 illustrates the motivation of solar energy, the operation of solar cell in general, and overview of the photovoltaic technology. History of CIGSe thin film solar cells and various properties of CIGSe are presented. The influence of Na content on the properties of CIGSe solar cells is discussed.

Chapter 2 deals with the detailed literature survey of CIGSe film deposition methods including, vacuum and non-vacuum approaches. The importance of CIGSe nanoparticles, as well as particle based film preparation, are discussed.

Chapter 3 describes the experimental procedures for preparation of CIGSe particles and films. The various characterization techniques that we used to study the structural, morphological, compositional and optical and electrical properties of CIGSe particles and films are presented.

Chapter 4 explains about the synthesis of CIGSe sub-micron particles by one-pot heating-up method. The influence of reaction temperature and reaction time on CIGSe particle synthesis are investigated. The formation mechanism of CIGSe is studied in detailed. The large-scale synthesis of CIGSe powder is performed. The influence of Cu concentration on the properties of CIGSe is examined.

Chapter 5 deals with the preparation of CIGSe films using sub-micron particles synthesized by one-pot heating-up process. The CIGSe powder concentration is optimized during the ink formulation. The CIGSe films are prepared by doctor blade method. The influence of an air annealing temperature of CIGSe film is studied. The selenization process is carried out for air annealed CIGSe films with and without NaCl treatment at different temperature. The structural, morphological, compositional, optical, electrical and opto-electronic properties of CIGSe films are investigated.

Chapter 6 describes the synthesis of CIGSe nanoparticles by hot injection process and preparation of films using this nanoparticles. The nanoparticles synthesis parameters of reaction temperature and reaction time are optimized. The formation mechanism of CIGSe is examined. The CIGSe films are prepared by doctor blade method, followed by air annealing and selenization. Various properties of CIGSe films are studied.

Chapter 7 gives the summary and conclusions drawn from the various investigations carried out on CIGSe particles and films. Finally, the scope for future work is proposed.

References

[1] http://yosemite.epa.gov/oar/globalwarming.nsf/content/index.html.

[2] R.H. Bube, Photoelectronic properties of semiconductors, Great Britain, Cambridge University Press, 1992.

[3] A. Luque, S. Hegedus, Handbook of photovoltaic science and engineering, Edited by A. Luque, S. Hegedus, England, John Wiley & Sons Ltd, 2003.

[4] Report of the Basic Research workshop on Solar Energy Utilization April 18-21,2005. URL:http://www.sc.doe.gov/bes/reports/files/SEU_rpt.pdf.

[5] D.M. Chapin, C.S. Fuller, G.L. Pearson, A new silicon p-n junction photocell for converting solar radiation into electrical power, J. Appl. Phys. 25 (1954) 676–677. doi:10.1063/1.1721711.

[6] M.A. Green, K. Emery, Y. Hishikawa, W. Warta, Solar cell efficiency tables (version 36), Prog. Photovoltaics Res. Appl. 18 (2010) 346–352. doi:10.1002/pip.1021.

[7] P. Jackson, R. Wuerz, D. Hariskos, E. Lotter, W. Witte, M. Powalla, Effects of heavy alkali elements in Cu(In,Ga)Se_2 solar cells with efficiencies up to 22.6%, Phys. Status Solidi - Rapid Res. Lett. 10 (2016) 583–586. doi:10.1002/pssr.201600199.

[8] http://www.rechargenews.com/solar/867748/first-solar-sets-221-percent-cdte-efficiency-record.

[9] M. A. Green, K.Emery, Y. Hishikawa, W. Warta, E. D. Dunlop, Solar cell efficiency tables (version 48), Prog. Photovoltaics Res. Appl. 24 (2016) 905–913. doi: 10.1002/pip.2788/full.

[10] I. Repins, M.A. Contreras, B.Egaas, C. DeHart, J. Scharf, C. L. Perkins, B.To, R. Noufi, 19.9%-efficient ZnO/CdS/$CuInGaSe_2$ Solar Cell with 81.2% Fill Factor, Prog. Photovoltaics Res. Appl. 16 (2008) 235–239. doi: 10.1002/pip.822/full.

[11] C. Rincon, J. Gonzalez, Temperature dependence of the bandgap in $CuInSe_2$, Sol. Cells. 16 (1986) 357–362. doi:10.1016/0379-6787(86)90095-5.

[12] A. Ben Marai, J. Ben Belgacem, Z. Ben Ayadi, K. Djessas, S. Alaya, Structural and optical properties of $CuIn_{1-x}Ga_xSe_2$ nanoparticles synthesized by solvothermal

route, J. Alloys Compd. 658 (2016) 961–966. doi:10.1016/j.jallcom.2015.10.287.

[13] J. Li, Z. Jin, T. Liu, J. Wang, D. Wang, J. Lai, H. Du, L. Cui, Ternary and quaternary chalcopyrite $Cu(In_{1-x}Ga_x)Se_2$ nanocrystals: organoalkali-assisted diethylene glycol solution synthesis and band-gap tuning, CrystEngComm. 15 (2013) 7327. doi:10.1039/c3ce40813b.

[14] B.J. Stanbery, Copper Indium Selenides and Related Materials for Photovoltaic Devices, Crit. Rev. Solid State Mater. Sci. 27 (2002) 73–117. doi:10.1080/20014091104215.

[15] S.C. Abrahams, Piezoelectric nonlinear optic $CuGaSe_2$ and $CdGeAs_2$:Crystal structure, chalcopyrite microhardness, and sublattice distortion, J. Chem. Phys. 61 (1974) 1140. doi:10.1063/1.1681987.

[16] D. Abou-Ras, R. Caballero, C.A. Kaufmann, M. Nichterwitz, K. Sakurai, S. Schorr, T. Unold, H.W. Schock, Impact of the Ga concentration on the microstructure of $Culn_{1-x}Ga_xSe_2$, Phys. Status Solidi - Rapid Res. Lett. 2 (2008) 135–137. doi:10.1002/pssr.200802059.

[17] T. Haalboom, T. Gödecke, F. Ernst, M. Ruhle, R. Herberholz, H.W. Schock, C. Beilharz and K.W. Benz, “Phase Relation and Microstructure in Bulk Materials and Thin Films of the Ternary System Cu-In-Se”, Proceedings of the 11th International Conference on Ternary and Multinary compounds, ICTMC-11, University of Salford, 249, 1997.

[18] D. Schmid, M. Ruckh, F. Grunwald, H.W. Schock, Chalcopyrite/defect chalcopyrite heterojunctions on the basis of $CuInSe_2$, J. Appl. Phys. 73 (1993) 2902–2909. doi:10.1063/1.353020.

[19] A. Niemegeers, M. Burgelman, R. Herberholz, U. Rau, D. Hariskos, Model for Electronic Transport in $Cu(In,Ga)Se_2$ Solar Cells, Prog. Photovolt. Res. Appl. 6, 407±421. 421 (1998) 407–421. doi:10.1002/(SICI)1099-159X(199811/12)6:6<407::AID-PIP230>3.0.CO;2-U.

[20] D. Metastabilities, Role of Defects and Defect Metastabilities for the Performance and Stability of $Cu(ln,Ga)Se_2$ Based Solar Cells, Energy. 39 (2000) 389–394.

[21] S.H. Wei, S.B. Zhang, A. Zunger, Effects of Ga addition to $CuInSe_2$ on its electronic, structural, and defect properties, Appl. Phys. Lett. 72 (1998) 3199–3201.

doi:10.1063/1.121548.

[22] P. Migliorato, J.L. Shay, H.M. Kasper, S. Wagner, Analysis of the electrical and luminescent properties of $CuInSe_2$, J. Appl. Phys. 46 (1975) 1777–1782. doi:10.1063/1.321782.

[23] R. Noufi, R. Axton, C. Herrington, S.K. Deb, Electronic properties versus composition of thin films of $CuInSe_2$, Appl. Phys. Lett. 45 (1984) 668–670. doi:10.1063/1.95350.

[24] H. Newman," Optical properties and electronics band structure of $CuInSe_2$." Sol. Cells 16, 317 (1986).

[25] S. Wei, A. Zunger, Band offsets and optical bowling of chalcopyrite and Zn-based II-IV alloys, J. Appl. Phys. 78 (1995) 3846.

[26] C.J. Chen, PHYSICS OF SOLAR ENERGY - CHEN.pdf, (2011) 326.

[27] M.A. Contreras, L.M. Mansfield, B. Egaas, J. Li, M. Romero, R. Noufi, E. Rudiger-Voigt, W. Mannstadt, Improved energy conversion efficiency in wide bandgap Cu(In, Ga)Se_2 solar cells, 37th IEEE Photovolt. Spec. Conf. PVSC 2011. (2011) 26–31. doi:10.1109/PVSC.2011.6185837.

[28] L. Kazmerski " Optical properties and grain boundary effects in $CuInSe_2$", J.Vac. Sci. Technol., A1, 395 (1983)

[29] S.B. Zhang, S.-H. Wei, A. Zunger, H. Katayama-Yoshida, Defect physics of the $CuInSe_2$ chalcopyrite semiconductor, Phys. Rev. B. 57 (1998) 9642–9656. doi:10.1103/PhysRevB.57.9642.

[30] C. Persson and A. Zunger, Anomalous Grain Boundary Physics in Polycrystalline $CuInSe_2$: The Existence of a Hole Barrier, Phys. Rev. Lett.. 91 (2003) 266401-1. doi: 10.1103/PhysRevLett.91.266401.

[31] C. Persson, A. Zunger, Compositionally induced valence-band offset at the grain boundary of polycrystalline chalcopyrites creates a hole barrier, Appl. Phys. Lett. 87 (2005) 1–3. doi:10.1063/1.2132537.

[32] S. Minoura, K. Kodera, T. Maekawa, K. Miyazaki, S. Niki, Dielectric function of Cu (In,Ga)Se_2 -based polycrystalline materials, 63505 (2013) 22–25.

[33] J.E. Jaffe, A. Zunger, Electronic structure of the ternary chalcopyrite semiconductors $CuAlS_2$, $CuGaS_2$, $CuInS_2$, $CuAlSe_2$, $CuGaSe_2$, and $CuInSe_2$, Phys.

Rev. B. 28 (1983) 5822–5847. doi:10.1103/PhysRevB.28.5822.

[34] J.E. Jaffe, A. Zunger, Theory of the band-gap anomaly in ABC_2 chalcopyrite semiconductors, Phys. Rev. B. 29 (1984) 1882–1906. doi:10.1103/PhysRevB.29.1882.

[35] M. Bodegard and L. Stolt. Influence of sodium on the Grain structure of $CuInS_2$ films for photovoltaic applications. In 12th European Photovoltaic Solar Energy Con-ference, 1994

[36] J. Holz, F. Karg, and H. von Philipsborn. The effect of substrate impurities on the electronic conductivity in cis thin films. In 12th European Photovoltaic Solar Energy Conference, 1994.

[37] K. Granath, M. Bodegård, L. Stolt, Effect of NaF on Cu(In,Ga)Se_2 thin film solar cells, Sol. Energy Mater. Sol. Cells. 60 (2000) 279–293. doi:10.1016/S0927-0248(99)00089-6.

[38] D. Rudmann, G. Bilger, M. Kaelin, F.J. Haug, H. Zogg, A.N. Tiwari, Effects of NaF coevaporation on structural properties of Cu(In,Ga)Se_2 thin films, Thin Solid Films. 431–432 (2003) 37–40. doi:10.1016/S0040-6090(03)00246-3.

[39] R. Kimura, T. Mouri, T. Nakada, S. Niki, Y. Lacroix, T. Matsuzawa, K. Takahashi, and A. Kunioka. Photoluminescence Properties of Sodium Incorporated in $CuInSe_2$ Thin Films. Jpn. J. Appl. Phys., 38 (1999) L289–L291. doi: 10.1143/JJAP.38.L289/meta.

[40] M.U. Lammer, U. Klemm, M. Powalla, Sodium co-evaporation for low temperature Cu(In,Ga)Se_2 deposition, Thin Solid Films. (2001) 33–36.

[41] B. M. Keyes, F. Hasoon, P. Dippo, A. Balcioglu, and F. Abulfotuh. Influence of Na on the electro-optical properties of Cu(In,Ga)Se_2. In Conference Record Of The Twenty Sixth IEEE Photovoltaic Specialists Conference, pages 479–482. IEEE 1997.

[42] J. Schroeder David, A. A. Rockett, Electronic effects of sodium in epitaxial $CuIn_{1-x}Ga_xSe_2$, J. Appl. Phys. 82 (1997).

[43] D. Rudmann, Effects of sodium on growth and properties of Cu(In,Ga)Se_2 thin films and solar cells, Thesis. (2004) 1–187. doi:10.3929/ethz-a-004796411.

[44] D. Rudmann, D. Bŕmaud, H. Zogg, A.N. Tiwari, Na incorporation into

Cu(In,Ga)Se_2 for high-efficiency flexible solar cells on polymer foils, J. Appl. Phys. 97 (2005) 1–6. doi:10.1063/1.1857059.

[45] D. Braunger, S. Zweigart and S.W. Schock, “The Influence of Na and Ga on the Incorporation of the Chalcogen in Polycrystalline Cu(In,Ga)$(S,Se)_2$ Thin-Films for Photovoltaic Applications”, 2nd World Conference of Photovoltaic Solar Energy Conversion, Vienna, 1113, 1998.

[46] S. H. Wei, S. B. Zhang, A. Zunger, Effects of Na on the electrical and structural properties of $CuInSe_2$, J. Appl. Phys. 85 (1999) 7214-18. doi: 10.1063/1.370534.

[47] D. Braunger, D. Hariskos and S.W. Schock, “Polycrystalline Cu(In,Ga)Se_2 Solar Cells”, 2nd World Conference of Photovoltaic Solar Energy Conversion, Vienna, 511, 1998.

[48] M.A. Contreras, B. Egaas, P. Dippo, J. Webb, J. Granata, K. Ramnathan, S. Asher, A. Swartzlander and R. Noufi, “On the Role of Na and Modifications to Cu(ln,Ga)Se_2 Absorber Materials Using Thin-MF (M=Na, K, Cs) Precursor Layers”, conference proceedings of 26th IEEE Photovoltaic Specialists Conference, Anaheim, IEEE Press, Piscataway, 359, 1997.

Chapter 2

Deposition methods of CIGSe thin films

In this chapter, a brief review of CIGSe deposition methods are discussed which broadly classified as vacuum and non-vacuum. Vacuum methods including co-evaporation, sputtering, molecular beam epitaxy, close-space chemical vapor transport and field-assisted simultaneous synthesis and transfer are discussed. Classifications of non-vacuum methods such as nanoparticles based approach, hydrazinium precursors, sol-gel, pyrolysis, and electrodeposition are discussed in detail. Reviewing all the techniques is beyond the scope of film deposition based on CIGSe nanoparticles solution which has used in this work.

2.1. Vacuum methods

2.1.1. Co-evaporation

Cu(In, Ga)Se_2 (CIGSe) thin films prepared by co-evaporation process from elemental sources showed the highest efficiencies for thin film photovoltaic devices. In 1980, Mickelsen and Chen **[1]** prepared 5.7% polycrystalline $CuInSe_2$ (CISe) PV devices using a so-called Boeing bilayer co-evaporation process which simultaneously evaporation of elemental copper and indium metals under selenium vapor. To avoid the interaction between selenide and gold back contact at high temperature, the deposition process started with the deposition of low-resistivity small-grain Cu-rich CISe at 350^0C and ended with excess indium deposition rate at 450^0C. Based on Boeing bilayer co-evaporation process, Gabor et al. **[2]** advanced this approach to form a so-called three-stage co-evaporation process which started deposition with ~90% indium and gallium with excess Se at 250-300^0C which were followed by copper selenide deposition and finally capped with the rest ~10% indium and gallium at >540^0C. The finished CIGSe film after three stages is slightly indium-rich.

Based on Cu-Se binary phase diagram **[3]**, $Cu_{2-x}Se$ could exist in a liquid phase with excess Se at high temperature (>523^0C). In the three-stage evaporation process, $Cu_{2-x}Se$

was formed at the second stage and acts as a flux agent helping the recrystallization of CIGSe grains. Two factors were found to contribute to the solar cell efficiency using this process [2]. The surface of CIGSe films is extremely smooth with very less roughness (< 50nm). The less roughness of CIGSe films result in less surface area contributing to the junction area and consequently reduced the recombination happened at the junction interface. However, a problem of smoother films is to increase the light reflection on CIGSe films. Another factor beneficial to solar cell efficiency is the gallium gradient as a function of depth in the CIGSe films. The gallium concentration increases towards the back of the film. Such notch structure provided quasi-electric fields sweeping free electrons from CIGSe neutral region to the junction. In the aspect of process control, the deposition in the three-stage co-evaporation process is commonly monitored by mass spectroscopy which provides precise control on the deposition rate of each element [4]. So far, CIGSe solar cells fabricated by three stage co-evaporation process showed 22.6% energy conversion efficiency which is the highest record for thin film polycrystalline solar cells [5,6].

2.1.2. Sputtering and chalcogenization

Though three stage co-evaporation process has shown the best efficiencies in laboratory devices [5,7] and is one of the common method used in the manufacturing of commercial CIGSe modules [8], there are several drawbacks existing in this process. The uniformity of deposited CIGSe films by three stage co-evaporation process over a large area does not satisfy the requirement for highly efficient modules due to the limitation of the geometry of evaporation sources [9]. Low production throughput and poor simultaneous control of all evaporation sources are barriers delaying the commercial development of co-evaporation process [9]. By high deposition rate and uniformity, sputtering is a common physical vapor deposition method widely used in the manufacturing of CIGSe films. Usually, it involves two separated steps including material deposition and selenization are desired to synthesize CIGSe absorber. Selenization could be conducted during or after sputtering process.

Marudachalam et al. [10] used DC magnetron sputtering to deposit metal precursor layer in a sequence of Cu-Ga-In on Molybdenum (Mo)-coated soda lime glass substrates which were selenized under the atmosphere of $H_2Se/Ar/O_2$ gas mixture for 90 min. A post-reaction heat treatment under the Ar atmosphere for 60-90 min was used to selenized CIGSe films which were converted to single phase CIGSe after 600°C treatment. This three-layer structure showed 13% efficiency. Dhere et al. [11] used Cu-Ga alloy and indium targets instead of individual metal targets in a sequence of CuGa/In/CuGa/Selenization/In/CuGa/Selenization to solve the problem of low-melting-temperature of gallium and deleterious interaction between indium and gallium. The two-selenization strategy and Ga addition near the Mo contact have significant improvement to the adhesion of CIGSe films to the Mo back contact. This approach showed 9.02% efficiency. To further shorten the deposition process and control the uniformity of metallic precursor films, Cu-In-Ga ternary alloy targets are successfully developed to fabricate CIGSe thin film solar cells with an efficiency of 8% [12]. Further efficiency increased up to 13% by using High Power Impulse Magnetron Sputtering instead of regular DC sputtering in presence of selenium atmosphere [13]. One issue of this two-step sputtering process is the gallium accumulation near Mo back contact irrespective of a different kind of target used [10,12]. This leads to the phase separation which needs special treatments to recrystallize the films to form single phase CIGSe.

In addition to metallic targets, quaternary chalcogenide targets are able to use for CIGSe solar cells. RF sputtered films from single phase CIGSe targets exhibited binary selenides which were converted to single phase CIGSe by the post-selenization process and it showed 7.95% efficiency [14]. Frantz et al. [9] have fabricated CIGSe thin film solar cells with 8.9% efficiency without selenization during or after sputtering achieving. Deposition of Cu-Ga and metal precursor stacking layer of DC-sputtering and precursor layers was first selenized with H_2Se gas followed by sulfurization with H_2S gas in a furnace to form a CIGSSe. This device showed 22.3% efficiency [15] which is very close to co-evaporation process.

2.1.3. Other vacuum techniques

In addition to the co-evaporation and sputtering process, molecular beam epitaxy and close-space chemical vapor transport are other vacuum-based methods that have been used for the synthesis of CIGSe film [16]. Single crystalline CIGSe films grown by molecular beam epitaxy performed not as good as the polycrystalline films. Even though high-quality p-type CIGSe films were obtained by close-space chemical vapor transport, this technique uses corrosive HI as a transport agent which is too corrosive for many materials. Due to these drawbacks, these two methods are rarely used to deposit CIGSe films in practice.

Field-Assisted Simultaneous Synthesis and Transfer (FASST) process is a two-stage reactive transfer printing method developed by Heliovolt [17]. In the first step, copper selenide and indium selenide are deposited by physical vapor deposition (PVD) on Mo-coated glass substrates and calcium fluoride-coated substrates, respectively. In the second step, these two films are brought to contact closely and go through rapid reaction under pressure and electrostatic field. The final films are transferred to Mo substrates and calcium fluoride-coated substrates can be reused for many times with proper cleaning. Due to the imposed pressure and electrostatic field, the reaction between these two precursors is fast. That might reduce the thermal budget. The resulted CIGSe films showed a (220)/(204) preferred orientation which is different from the preferred (112) orientation by other methods. Using this technique, 12% efficiency was achieved.

2.2. Non-vacuum methods

2.2.1. Nanoparticles based solution

Nanoparticles are one of the most attractive materials in the scientific world due to their unique properties from bulk materials. In this section, several approaches based on nanoparticles for the deposition of CIGSe films were reviewed.

2.2.1.1. Metal nanoparticles

Copper and indium metal nanoparticles have been used to prepare metal precursor layer and then followed by post selenization in either Se or H_2Se gas to form CISe absorber films [18]. Ideally, this method must be very promising due to lower melting temperatures of indium and energetic nature of both elements which might be beneficial for forming dense films in a short time. However, the formation of indium oxide during spray deposition in ambient atmosphere contaminates CISe films [18].

2.2.1.2. Binary chalcogenides nanoparticles

Nano solar Inc. **[19]** has been used binary copper selenide and indium/gallium selenides as starting materials to fabricate CIGSe thin film solar cells which showed 14% efficiency. These selenide nanoparticles are dispersed in a various organic solution which might contain ingredients including solvents, surfactants, binders, emulsifiers, thickening agents, film conditioners, anti-oxidants, flow and leveling agents, plasticizers, and preservatives **[20]**. The actual recipe is not disclosed in the literature but must assure the appropriate properties which allow the formulation of an ink to be printed. With proper adjustment of the rheology of ink and thermal properties, the ink was printed by typical wet coating techniques onto substrates. $Cu_{2-x}Se$ has a relatively lower melting temperature of 523°C, is used to assist the growth of large and dense CIGSe films. Rapid thermal processing (RTP) was the most critical step to convert porous nanoparticle films into large sized densely packed grains. The main advantage of RTP over conventional slow-rate heating processes is it's high ramping rate (typically 10-20°C/sec) which can suppress the selenium loss during annealing and melt down the fluxing agent of $Cu_{2-x}Se$ before it totally reacts with indium/gallium selenides to form CIGSe which has higher melting temperature about 1000°C. The liquid or quasi-liquid phase of $Cu_{2-x}Se$ having very high flow ability compared to a solid phase which might fill the voids between particles and densify of the films. The choice of substrates influences the grain size and composition of selenized CIGSe. Na is the magic element controlling the migration of gallium across CIGSe films. By manipulating the Na concentration in CIGSe films, the gallium profiles can be flat at high Na content or notch shape at low Na content **[19]**. The finished solar cell has decent characteristics with 14% efficiency for aperture area. Considering the similar core-shell strategy, Yoon et al. **[21]** synthesized Cuse/InSe nanoparticles and it showed only ~1% efficiency which is much lesser than the result from Nano solar Inc.

2.2.1.3. Metal oxides nanoparticles

Metal oxides are abundant forms of metal compounds exists on the earth. Using metal oxides to synthesize chalcopyrite CIGSe may reduce the cost of raw material and potentially the final PV modules. International Solar Electric Technology Inc. (ISET)

[22,23] and Unisun **[24]** are the two pioneers exploring the area of converting metal oxides into CIGSe films. In ISET's method, with fixed Cu/(In+Ga) ratio of elements (copper, indium, and gallium) were dissolved by acid to obtain a homogeneously mixed aqueous solution of Cu, In and Ga compounds. Then, these metal ions are co-precipitated by adding sodium hydroxide solution (NaOH) resulting in a mixture of metal hydroxides which are dried at 450°C to obtain fine oxides powder. The size of the oxide particles is controlled by the pH value of reaction mixture and delivery rate of NaOH during hydrolysis. Usually, the average diameter of nanoparticles is ~250 nm with tight distribution. The ink was formulated by dispersing the powder in water and surfactants by ball milling technique. The obtained oxides paste can be deposited on Mo-coated substrates by various wet coating techniques. An H_2 reduction reaction is conducted on oxide films which are reduced and converted to metal layers, followed by a selenization or sulfurization process to convert the metal films into CIGSe films. Unisun **[24]** used oxide nanoparticles as starting materials as well, but the synthesizing method is not clear. However, the reduction reaction by H_2 was not included in Unisun's process. Solar cells showed 13.6% and 11.7% efficiency in the laboratory by ISET and Unisun, respectively. Two major issues of this oxide nanoparticle approach could counterbalance its advantage in low cost, compositional uniformity and easy handling. Copper oxide, indium oxide, and gallium oxide are very stable at room temperature as well as high temperature. The good stability makes the ink easily preserved, but hinders the reduction of metal oxides to pure metals. Thermodynamically, the reduction reaction of copper oxide at 500°C is favorable, while the reduction of indium and gallium oxides is not favorable even at 500°C **[22]**. This difficulty makes the reduction reaction very difficult to complete and residual oxides are likely to remain in the films. Elemental metals go through dissolution, precipitation, and reduction back to metal forms in the ISET approach. From the perspective of mass and energy consumption, this process is not mass and energy efficient at all, that is saying extra energy and materials are consumed and certainly increase the manufacturing cost.

2.2.1.4. Ternary/quaternary nanoparticles

It is a straightforward to use ternary/quaternary chalcopyrite particles as 'bricks' to directly build bulk chalcopyrite materials. Guo et al. [25] and Panthani et al. [26] have used hot injection method to synthesize successfully chalcopyrite phase of $CuInSe_2$ and $CuInS_2$ nanoparticles. These nanoparticles can be dispersed in various non-polar solvents like hexane, toluene etc. to form stable ink for printing [26]. After deposited on substrates, the organic solvents are evaporated by annealing in an inert atmosphere (e.g. Ar) at 500°C. Afterwards, selenization at 500°C is applied to the nanoparticles films to densify and recrystallize the films [25]. KCN etching is used to remove Cu_xSe phases and adjust the composition to indium-rich phase. The obtained solar cell with conventional structures shows 3% efficiency with relatively small V_{oc} [25]. Small sized grains and large grain boundary are the main issues for these solar cells.

CISe has a high melting temperature above 1000°C which hinders the recrystallization of CISe nanoparticles when the selenization is performed at 500°C. Guo et al. synthesized $CuInGaS_2$ nanoparticles using similar chemistry and converted $CuInGaS_2$ nanoparticle films into $Cu(In_{1-x}Ga_x)(S_{1-y}Se_y)$ films by selenization. This new strategy offers two benefits. Firstly, the bandgap of $CuInSe_2$ is about 1eV which is lower than the optimal bandgap of 1.14eV for maximum efficiency based on calculation [27]. Gallium and sulfur are used as doping elements to increase the bandgap of CISe which would enhance the solar cell performance. Secondly, due to the larger atomic size of selenium, the replacement of sulfur by selenium during selenization helps the recrystallization of nanoparticles and expand the lattice to eliminate void space between nanoparticles to achieve dense films with larger grain size. The efficiency of CIGSSe solar cells increased to 6% by using this new selenization strategy **[28][29]**. By adding Na soaking prior to selenization, the efficiency could increase to 12% **[30]**. In Guo's approach, the nanoparticle films have vanished the nano-structured feature during selenization. Instead of 'melting' nanocrystals together, Panthani et al. **[26]** used the nanoparticle films to make the solar cell directly without selenization, which preserves the nanoparticle feature. However, due to the high recombination through defects and impurities, the solar cell performance is much lower than the selenized samples [31].

2.2.2. Hydrazinium precursor based solution

An ideal solution-based method for the preparation of CIGSe thin films is dissolving CIGSe compound into solvents that can be easily evaporated by mild thermal annealing leaving pure CIGSe films. Regular solvents such as water, alcohols, and acetone do not have the ability to break down the crystal network of metal or ceramics. Hydrazine is an extremely polar liquid with similar physical properties as water, possesses the unique reducing nature to dissolve certain metal selenides and sulfides at high concentrations with extra chalcogens. Commonly, Cu_2S, Ga_2Se_3, In_2Se_3, S and/or Se were dissolved separately in hydrazine with continuous stirring and afterward mixed all together to form precursor inks. N_2 and H_2 gasses were released during dissolution. The advantage of this approach is the flexibility to conveniently and precisely modify the CIGSe film composition simply by varying the amount of each component used in the solution. The formed inks can be deposited onto substrates by various deposition techniques such as spin casting and/or dip coating, followed by annealing on a hot plate to get rid of volatile N_2H_4. Due to the weak bond between hydrazine and metal chalcogenides, the obtained CIGSe films do not suffer from contamination of solvent and surfactant residues which is a common issue for many solution-based methods. Using this approach, 15.2% of efficiency was achieved for CIGSSe solar cells [32]. Since hydrazine is a highly toxic and flammable species, it is rather hard to transfer this technique to a large-scale industrial production. The effort has been made to find alternative benign solvents with appropriate polar and reducing properties to replace hydrazine. However, no good results have been reported so far.

2.2.3. Sol-gel and spray pyrolysis

The sol-gel method is another common technique used in the field of material science for the preparation of bulk and thin films materials. Typical precursors are metal salts and metal alkoxides. Oliveira et al. [33] deposited CIGSe films using copper (II) acetate monohydrate, indium (III) acetate and gallium (III) acetylacetonate which is dissolved in ethanol along with complex agent diethanolamine. Kaelin et al. [34] used copper nitrate hemi pentahydrate, indium chloride and gallium nitrate hydrate dissolved in methanol with ethyl cellulose as a binder to fabricate solar cells with 6.7% efficiency [34]. The disadvantage of this method is the thick carbon layers formed between CIGSe films and back contact layer. These impurity carbon layers behave as potential recombination centers and barriers for the collection of photocurrent. The binder ethyl cellulose for modifying the rheology of the inks is the major source of carbon residue. Without binders, some of the coating techniques such as spin coating, doctor blading could result in rough films with serious cracking issues. Spray pyrolysis is another way to deposit CIGSe precursor films without binders. The fabrication procedure is more similar to the sol-gel method. During spraying, the substrates are subject to continuous heating which simultaneously transforms the metal precursors to oxides under air or sulfides/selenides with sulfur/selenium precursors in precursor inks. Sulfurization or selenization are utilized to recrystallize the obtained films. Hossain et al prepared CIGSSe by spray pyrolysis using an aqueous solution of $CuCl_2.2H_2O$, $InCl_3$, $GaCl_3$ and thiourea at 300-350°C followed by selenization at 500°C for 10 min. The CIGSSe solar cell showed 10.5% efficiency by this approach [35].

2.2.4. Electrodeposition

Electrodeposition is a fully developed technology for the mass production of metallic film coatings in industry. However, the application of electrodeposition in semiconductor films is limited since it’s much harder to control the semiconductor properties compared to metallic properties [36]. Several deposition strategies are used to synthesize ternary or quaternary chalcopyrite films. The simplest strategy is to deposit elemental layers (i.e. Cu, In, Ga, Se) from single elemental solutions one by one. The resulted elemental stack layers are then subjected to selenization for the conversion of precursor films to CISe/CIGSe films [37]. The electrodeposition potentials over normal hydrogen electrode (NHE) for Cu, In, Ga, Se are 0.35V, -0.34V, -0.53V and 0.75V, respectively [36]. It is easy to electro-deposit Cu and Se by reduction but very difficult for In and Ga depositions due to their negative potential values and the side reaction of reduction of the proton. Special efforts are needed to obtain good quality films.

Instead of multiple depositions, Herrero et al. [38] deposited Cu-In alloy in a single bath with a negative potential smaller than that of In. Cu_xSe, In_2Se_3, and Ga_2Se_3 have positive electrodeposition potential vs. NHE and can be deposited easier than the metallic films [37]. By mixing metal and Se precursors in solutions, binary selenides can be deposited in sequence on substrates and transformed to ternary or quaternary compounds with an extra annealing step. Bhattacharya [39] electro-deposited $CuInSe_2$ films from a single bath containing all three elements. The deposition process is controlled by the ratio between selenium and copper ionic species in an acidic and In-rich environment. The as-deposited films showed a mixture of several phases in nanocrystalline or amorphous states. In addition to CISe, binary phases were present in the films and transformed to ternary phases easily due to their reactive properties. Due to the poor electronic properties of as-deposited films, extra steps are necessary to recrystallize the films. Selenization is a common method to improve the crystallinity of CISe/CIGSe films. Guillemoles et al. [40] fabricated CISSe solar cells with 11% efficiency using precursor films by electrodeposition followed by sulfurization. Bhattacharya et al. [41] utilized physical vapor deposition to adjust the composition of electrodeposited films to indium-rich phase and recrystallize the CIGSSe grains resulting in cells with a 15.4% efficiency.

Table 2.1 Chalcopyrite absorber layer deposited from various non-vacuum based approaches such as nanoparticles, hydrazinium precursor, sol-gel, spray pyrolysis and electrodeposition.

Year	**Absorber**	**PCE (%)**	**Deposition and solvent**	**Post-treatment**	**Description**	**Ref**
			Nanoparticles based solution			
2008	$CuInSe_2$	2.82	Drop-casting	450–550°C (selenization in a Se/Ar atmosphere)	$CuInSe_2$ NPs (CuCl, $InCl_3$ and Se in oleylamine (OLA)	[25]
2009	$Cu(In_{1-x}Ga_x)(S_{1-y}Se_y)_2$	5.5	Drop-casting, toluene	500°C (selenization in a graphite box)	$Cu(In_{1-x}Ga_x)S_2$ NPs (metal-chlorides and S in OLA)	[29]
2015	$Cu(In,Ga)(S,Se)_2$	15	Doctor-blading, hexanethiol	500°C (selenization in a graphite box)	$Cu(In_{1-x},Ga_x)S_2$ NPs (metal(acac) salts and S in OLA)	[42]
2010	$CuInSe_2$	3.1	Spray-coating	-	$CuInSe_2$ NPs (metal-chlorides	[31]

					and Se in a mixture of OLA and TBP)	
2000	$CuInSe_2$	10.56	Spray-coating, aqueous dispersion	440°C (selenization in a H_2Se/N_2 atm.)	Sub-micron sized Cu–In alloy particles (melt atomization technique)	[43]
2003	$CuIn_{1-x}Ga_xSe_2$	13.6	Printing	420–450°C (reduction and selenization in H_2/N_2 and H_2Se/N_2 gas)	A mixture of oxide NPs (chemical approach)	[23]
2011	$CuInSe_2$	7.0	Doctor-blading	550°C (selenization in a Se/N_2 atm.)	Citrate-capped $Cu_{11}In_9$ NPs ($NaBH_4$-assisted chemical reduction)	[44]
2012	$CuInSe_2$	8.2	Drop-casting	530°C (selenization)	NPs of $CuInSe_2$, CuSe, $Cu_{2-x}Se$, and In_2O_3 (microwave-assisted synthesis)	[45]
Hydrazinium precursor based solution						
2008	Cu(In, Ga)(S, $Se)_2$	10.3	Spin-coating	Annealing with inert gas (400-525°C)	Solution of Cu_2S, In_2Se_3, Ga_2Se_3 and Se in hydrazine	[46]
2012	Cu(In, Ga)(S, $Se)_2$	15.2	Spin-coating	Annealing with inert gas (540°C)	Solution of In_2Se_3 with Se, Cu_2S with S	[32]

					and Ga in hydrazine	
Sol-gel and pyrolysis						
2005	$Cu(In,Ga)Se_2$	6.7	Doctor-blading, sol gel	550°C (selenization)	Precursor pastes of $Cu(NO_3)_2$, $InCl_3$, $Ga(NO_3)_3$, hydrate in metanol and ethylcellulose	[34]
2014	$Cu(In,Ga)(S, Se)_2$	10.5	Spray pyrolysis	500°C (selenization)	Aqueous solution of ($CuCl_2.2H_2O$, $InCl_3$, $GaCl_3$ and thiourea	[35]
Electrodeposition						
2009	$CuIn(S, Se)_2$	11	Electrodeposition	n.a.	Copper, Indium, and Selenium species in an acidic sulfate solution	[47]
1999	$CuIn_{1-x}Ga_xSe_2$	15.4	Electrodeposition + PVD	~40°C (selenization)	For electrodeposition, $CuCl_2$, $InCl_3$, H_2SeO_3, $GaCl_3$, and LiCl dissolved in deionized water. Deposition of In, Ga, and Se by PVD at 560±10°C (substrate temperature)	[41]

Table 2.1 shows the chalcopyrite absorber layer deposited from various non-vacuum based approaches such as nanoparticles, hydrazinium precursor, sol-gel, spray pyrolysis and electrodeposition. The highest efficiency of 15, 15.2 and 15.4% from quaternary CIGS nanoparticles, hydrazinium precursor and hybrid deposition (electrodeposition and PVD) respectively. All these three approaches showed very similar solar cell performance. Among them, quaternary nanoparticles are a very promising strategy by considering cost effective and toxicity issues.

2.3. CIGSe nanoparticles synthesis methods

In recent years, numerous synthesis methods have been reported for synthesis of CIGSe nanoparticles, such as ball milling, hot-injection, and solvothermal method. The ball milling is a widely-used method for grinding materials to extremely fine powder [48]. Typical ball mills contain a cylinder rotating around a horizontal axis which is partially filled with the material to be ground and the ground medium (hard materials such as a ceramic ball, stainless steel balls etc.). The materials are ground to fine powder by an internal cascading effect. The rotating speed should be smaller than the critical speed after which the ability to grind decreases because the ground medium starts to move along with cylinders at the same pace. High-quality ball mills can reduce particle size to the nanometer scale, resulting in the extremely large surface area which may become very reactive. To prevent particles from agglomeration, surfactants or organic solvents are added during grinding. For CIGSe application, ball mills have been used to grind different precursor materials, such as chalcogenides **[49][50]** and metal oxides **[22][23]**. The chemical reaction can also be introduced during grinding to synthesize CIGSe nanoparticles from pure element powders [51]. However, no working devices were reported by this method.

Hot injection method developed by Murray et al. [52] in 1993 for the synthesis of monodispersed cadmium chalcogenides quantum dots is one of the most popular methods to make nanoparticles. A multi-necked flask mounted on a heating mantle is filled by solvents which have been de-gassed by inert gas and connected to vacuum/inert gas by schlenk line. After the solvents are heated to a certain temperature, the reagents are injected into the flask and the reaction starts quickly. To control the size and agglomeration of nanoparticles, surfactants must be added to cap the surface of nanoparticles and stop the further reaction and the interaction between particles. The selection of surfactants strongly depends on the type of precursors and the desired properties of nanoparticles. Surfactants are usually long carbon chain hydrocarbons with nucleophilic groups such as oleic acid, oleylamine, trioctylphosphine etc. The nucleophilic groups attach to the surface of nanoparticles via coordinate bonds. By adjusting the strength of coordinate bonds and the temperature of solvents, the size and shape of nanoparticles can be controlled precisely. The CIGS nanoparticles **[25][29]** are synthesized by hot injection of elemental sulfur in oleylamine into oleylamine solution containing copper (II) acetylacetonate, indium (III) acetylacetonate, and gallium (III) acetylacetonate at 285°C for 30 mins. Hexane and ethanol are added to the mixture to flocculate the nanoparticles after the temperature decreases to 60°C. CIGSe nanoparticles are separated from the reaction mixture by centrifuge and can be redispersed in non-polar solvents. The injection of solution at high temperature leads to difficulty in controlling the monomer transfer which limits the large-scale synthesis.

Solvothermal synthesis is another important solution-based approach to synthesize CIGSe nanoparticles. The reaction temperature can be lower than the hot injection method since autoclaves are commonly employed to provide relatively high pressure over the reactants. For CISe synthesis [53,54], metal salts such as copper/indium chlorides and selenium powder are added to autoclaves with solvents and surfactants. The sealed autoclaves are heated at temperature <200°C for several hours, then cooled to room temperature naturally. The obtained nanoparticles are collected by centrifuge and redispersed in non-polar solvents. The biggest disadvantage of the solvothermal method is its longer reaction time compared to the hot injection method.

To synthesize metal chalcogenides, the simplest way is the precipitation reaction of metal cations and chalcogenide anions. However, the reaction rate of precipitation is too fast to yield nanoparticles at room temperature. To slow down the reaction rate and control the particle size formed in solution, the low-temperature condition must be used. Schulz et al. [55] mixed CuI, InI_3, and GaI_3 dissolved in pyridine with Na_2Se in methanol at a reduced temperature under an inert atmosphere to produce selenides colloids which were amorphous by X-ray diffraction (XRD) and transmission electron microscopy (TEM).

In this research work, we propose a facile one-pot heating-up method to synthesis CIGSe particles for the first time. This method has several advantages such as facile synthesis, economical, one-step process and lesser reaction time than solvothermal method. The detailed experimental procedure for one-pot heating-up method is given in **Chapter 3**. Also, we synthesized CIGSe powder by hot injection method at low temperature and experimental procedure is given in **Chapter 4**.

References

[1] R.A. Mickelsen, W.S. Chen, High photocurrent polycrystalline thin-film CdS/CuInSe$_2$ solar cella, Appl. Phys. Lett. 36 (1980) 371–373. doi:10.1063/1.91491.

[2] A.M. Gabor, J.R. Tuttle, D.S. Albin, M.A. Contreras, R. Noufi, A.M. Hermann, High-efficiency CuIn$_x$Ga$_{1-x}$Se$_2$ solar cells made from (In$_x$,Ga$_{1-x}$)$_2$Se$_3$ precursor films, Appl. Phys. Lett. 65 (1994) 198–200. doi:10.1063/1.112670.

[3] H.R.A.U.A.N.D.A. RABENAU, Vapour Pressure Measurements in the Copper-Selenium System, J. Solid State Chem. 1,5 15-5 18. 2 (1970) 515–518.

[4] B.J. Stanbery, Copper Indium Selenides and Related Materials for Photovoltaic Devices, Crit. Rev. Solid State Mater. Sci. 27 (2002) 73–117. doi:10.1080/20014091104215.

[5] P. Jackson, D. Hariskos, E. Lotter, S. Paetel, R. Wuerz, R. Menner, W. Wischmann. M. Powalla, New world record efficiency for Cu(In,Ga)Se$_2$ thin-film solar cells beyond 20%, Prog. Photovolt: Res. Appl. 19 (2011) 894–897. doi: 10.1002/pip.1078/pdf.

[6] P. Jackson, R. Wuerz, D. Hariskos, E. Lotter, W. Witte, M. Powalla, Effects of heavy alkali elements in Cu(In,Ga)Se$_2$ solar cells with efficiencies up to 22.6%, Phys. Status Solidi - Rapid Res. Lett. 10 (2016) 583–586. doi:10.1002/pssr.201600199.

[7] I. Repins, M. Contreras, M. Romero, Y. Yan, W. Metzger, J. Li, S. Johnston, B. Egaas, C. Dehart, J. Scharf, B.E. McCandless, R. Noufi, Characterization of 19.9%-efficient CIGS absorbers, Conf. Rec. IEEE Photovolt. Spec. Conf. (2008). doi:10.1109/PVSC.2008.4922628.

[8] https://www-osapublishing-org.access.biblioteca.cinvestav.mx/oe/browse.cfm.

[9] J.A. Frantz, R.Y. Bekele, V.Q. Nguyen, J.S. Sanghera, A. Bruce, S.V. Frolov, M. Cyrus, I.D. Aggarwal, Cu(In,Ga)Se$_2$ thin films and devices sputtered from a single target without additional selenization, Thin Solid Films 519 (2011) 7763–7765. doi: S0040609011012703.

[10] M. Marudachalam, H. Hichri, R. Klenk, R.W. Birkmire, W.N. Shafarman, J.M. Schultz, T. Cu, Preparation of homogeneous Cu(InGa)Se$_2$ films by selenization of

metal precursors in H_2Se atmosphere, Renew. Energy. 67 (1995) 3978–3980.

[11] N.G. Dhere, K.W. Lynn, $CuIn_{1-x}Ga_xSe_2$ thin film solar cells by two-selenizations process using Se vapor, Sol. Energy Mater. Sol. Cells. 41–42 (1996) 271–279. doi:10.1016/0927-0248(95)00146-8.

[12] H.R. Hsu, S.C. Hsu, Y.S. Liu, Improvement of Ga distribution and enhancement of grain growth of $CuInGaSe_2$ by incorporating a thin CuGa layer on the single CuInGa precursor, Sol. Energy. 86 (2012) 48–52. doi:10.1016/j.solener.2011.09.005.

[13] A. Halbe, P. Johnson, S. Jackson, R. Weiss, U. Avachat, A. Welsh and A. P. Ehiasarian, Mater. Res. Soc. Symp. Proc., 2010, 1210.

[14] J.H. Shi, Z.Q. Li, D.W. Zhang, Q.Q. Liu, Z.Z. Sun, S.M. Huang, Fabrication of Cu(In, Ga)Se_2 thin films by sputtering from a single quaternary chalcogenide target, Prog. Photovoltaics Res. Appl. 19 (2011) 160–164. doi:10.1002/pip.1001.

[15] G. Rosa, A. Bosio, D. Menossi, N. Romeo, How the starting precursor influences the properties of polycrystalline $CuInGaSe_2$ thin films prepared by sputtering and selenization, Energies. 9 (2016). doi:10.3390/en9050354.

[16] A. N. Y. Samaan, R. Vaidhyanathan and R. Noufi, Growth and characterization of polycrystalline $CuInSe_2$ thin films, Solar Cells, 16 (1986) 181 - 198. doi: 0379678786900839.

[17] L. Eldada, M. Taylor, B. Sang, S. McWilliams, R. Oswald, B.J. Stanbery, Nanoengineered CIGS Thin Films for Low Cost Photovoltaics, Proc. SPIE. 7039 (2008) 70390M–70390M–8. doi:10.1117/12.796877.

[18] M. Kaelin, D. Rudmann, F. Kurdesau, T. Meyer, H. Zogg, A.N. Tiwari, CIS and CIGS layers from selenized nanoparticle precursors, Thin Solid Films. 431–432 (2003) 58–62. doi:10.1016/S0040-6090(03)00194-9.

[19] N. Inc, in 17th International Photovoltaic Science and Engineering Conference, Tokyo, Japan, 2007.

[20] B. M. Sager, D. Yu and M. R. Robinson, Nanosolar Inc., US, 2008, p. 15.

[21] S. Yoon, T. Yoon, K.S. Lee, S. Yoon, J.M. Ha, S. Choe, Nanoparticle-based approach for the formation of CIS solar cells, Sol. Energy Mater. Sol. Cells. 93 (2009) 783–788. doi:10.1016/j.solmat.2008.09.061.

[22] V.K. Kapur, M. Fisher, R. Roe, Nanoparticle oxides precursor inks for thin film Copper Indium Gallium Selenide (CIGS) solar cells, Mater. Res. Soc. Symp. - Proc. 668 (2001) H2.6. doi:10.1557/PROC-668-H2.6.

[23] V.K. Kapur, A. Bansal, P. Le, O.I. Asensio, Non-vacuum processing of $CuIn_{1-x}Ga_xSe_2$ solar cells on rigid and flexible substrates using nanoparticle precursor inks, Thin Solid Films. 431–432 (2003) 53–57. doi:10.1016/S0040-6090(03)00253-0.

[24] C. Eberspacher, K. Pauls and J. Serra, in 28th IEEE Photovoltaic Specialists Conference, Anchorage, Alaska, 2000, p. 517.

[25] Q. Guo, S.J. Kim, M. Kar, W.N. Shafarman, R.W. Birkmire, E. a Stach, R. Agrawal, H.W. Hillhouse, Development of $CuInSe_2$ Nanocrystal and Nanoring Inks for Low-Cost Solar Cells., Nano Lett. 8 (2008) 2982–2987. doi:10.1021/nl802042g.

[26] M.G. Panthani, V. Akhavan, B. Goodfellow, J.P. Schmidtke, L. Dunn, A. Dodabalapur, P.F. Barbara, B.A. Korgel, Synthesis of $CuInS_2$, $CuInSe_2$, and $Cu(In_xGa_{1-x})Se_2$ (CIGS) nanocrystal “inks” for printable photovoltaics, J. Am. Chem. Soc. 130 (2008) 16770–16777. doi:10.1021/ja805845q.

[27] W. Shockley, H.J. Queisser, Detailed balance limit of efficiency of p-n junction solar cells, J. Appl. Phys. 32 (1961) 510–519. doi:10.1063/1.1736034.

[28] Q. Guo, G.M. Ford, H.W. Hillhouse, R. Agrawal, Selenization of copper indium gallium disulfide nanocrystal films for thin film solar cells, Conf. Rec. IEEE Photovolt. Spec. Conf. (2009) 002126–002129. doi:10.1109/PVSC.2009.5411426.

[29] Q. Guo, G.M. Ford, H.W. Hillhouse, R. Agrawal, Sulfide nanocrystal inks for dense $Cu(In_{1-x}Ga_x)(S_{1-y}Se_y)_2$ absorber films and their photovoltaic performance, Nano Lett. 9 (2009) 3060–3065. doi:10.1021/nl901538w.

[30] Q. Guo, G.M. Ford, H.W. Hillhouse, R. Agrawal, A generalized and robust method for efficient thin film photovoltaic devices from multinary sulfide nanocrystal inks, Conf. Rec. IEEE Photovolt. Spec. Conf. (2011) 003522–003526. doi:10.1109/PVSC.2011.6186708.

[31] V. a Akhavan, M.G. Panthani, B.W. Goodfellow, D.K. Reid, B. a Korgel, Thickness-limited performance of $CuInSe_2$ nanocrystal photovoltaic devices., Opt.

Express. 18 Suppl 3 (2010) A411–A420. doi:10.1364/OE.18.00A411.

[32] T. K. Todorov, O. Gunawan, T.Gokmen, D. B. Mitzi, Solution-processed Cu(In,Ga)(S,Se)$_2$ absorber yielding a 15.2% efficient solar cell, Prog. Photovolt: Res. Appl. 21 (2013) 82–87. doi: 10.1002/pip.1253/epdf.

[33] L. Oliveira, T. Todorov, E. Chassaing, D. Lincot, J. Carda, P. Escribano, CIGSS films prepared by sol-gel route, Thin Solid Films. 517 (2009) 2272–2276. doi:10.1016/j.tsf.2008.10.104.

[34] M. Kaelin, D. Rudmann, F. Kurdesau, H. Zogg, T. Meyer, A.N. Tiwari, Low-cost CIGS solar cells by paste coating and selenization, Thin Solid Films. 480–481 (2005) 486–490. doi:10.1016/j.tsf.2004.11.007.

[35] M.A. Hossain, Z. Tianliang, L.K. Keat, L. Xianglin, R.R. Prabhakar, S.K. Batabyal, S.G. Mhaisalkar, L.H. Wong, Synthesis of Cu(In,Ga)(S,Se)$_2$ thin films using an aqueous spray-pyrolysis approach, and their solar cell efficiency of 10.5%, J. Mater. Chem. A. 3 (2015) 4147–4154. doi:10.1039/C4TA05783J.

[36] D. Lincot, J.F. Guillemoles, S. Taunier, D. Guimard, J. Sicx-Kurdi, A. Chaumont, O. Roussel, O. Ramdani, C. Hubert, J.P. Fauvarque, N. Bodereau, L. Parissi, P. Panheleux, P. Fanouillere, N. Naghavi, P.P. Grand, M. Benfarah, P. Mogensen, O. Kerrec, Chalcopyrite thin film solar cells by electrodeposition, Sol. Energy. 77 (2004) 725–737. doi:10.1016/j.solener.2004.05.024.

[37] G. Hodes,T.Engelhard, D. Cahen, Electroplated CuInS$_2$ and CuInSe$_2$ layers: preparation and physical and photovoltaic characterization, Thin Solid Films, 128 (1985) 93-106. doi: 0040609085903384.

[38] J. Herrero, J. Ortega, Electrodeposition of CuIn alloys for preparing CuInS$_2$ thin films, Sol. Energy Mater. 20 (1990) 53–65. doi:10.1016/0165-1633(90)90017-U.

[39] R. N. Bhattochary, Solution growth and electrodeposited CulnSe$_2$ thin films, J. Electrochem. Soc. 130 (1983) 2041–2044. doi: 130/10/2040.full.pdf.

[40] J.F. Guillemoles, J.P. Connolly, O. Ramdani, O. Roussel, D. Guimard, V. Bermudez, N. Naghavi, P.P. Grand, L. Parissi, J. Kurdi, J. Kessler, O. Kerrec, D. Lincot, Solution processing route to high efficiency CuIn(S,Se)$_2$ solar cells, J. Nano Res. 4 (2008) 79–89. doi:10.4028/www.scientific.net/JNanoR.4.79.

[41] R.N. Bhattacharya, W. Batchelor, J.F. Hiltner, J.R. Sites, Thin-film CuIn$_{1-x}$Ga$_x$Se$_2$

photovoltaic cells from solution-based precursor layers, Appl. Phys. Lett. 75 (1999) 1431. doi:doi:10.1063/1.124716.

[42] S.M. McLeod, C.J. Hages, N.J. Carter, R. Agrawal, Synthesis and characterization of 15% efficient CIGSSe solar cells from nanoparticle inks, Prog. Photovolt: Res. Appl. 2015; 23:1550–1556. doi: 10.1002/pip.2588/epdf.

[43] G. Norsworthy, C.R. Leidholm, A. Halani, V.K. Kapur, R. Roe, B.M. Basol, R. Matson, CIS film growth by metallic ink coating and selenization, Sol. Energy Mater. Sol. Cells. 60 (2000) 127–134. doi:10.1016/S0927-0248(99)00075-6.

[44] C. Kind, C. Feldmann, A. Quintilla, E. Ahlswede, Citrate-capped Cu11In9 nanoparticles and its use for thin-film manufacturing of cis solar cells, Chem. Mater. 23 (2011) 5269–5274. doi:10.1021/cm2024668.

[45] S. Jeong, B.-S. Lee, S. Ahn, K. Yoon, Y.-H. Seo, Y. Choi, B.-H. Ryu, An 8.2% efficient solution-processed $CuInSe_2$ solar cell based on multiphase $CuInSe_2$ nanoparticles, Energy Environ. Sci. 5 (2012) 7539. doi:10.1039/c2ee21269b.

[46] D.B. Mitzi, M. Yuan, W. Liu, A.J. Kellock, S. Jay Chey, V. Deline, A.G. Schrott, A high-efficiency solution-deposited thin-film photovoltaic device, Adv. Mater. 20 (2008) 3657–3662. doi:10.1002/adma.200800555.

[47] J.-F. Guillemoles, P. Cowache, A. Lusson, K. Fezzaa, F. Boisivon, J. Vedel, D. Lincot, One step electrodeposition of $CuInSe_2$: Improved structural, electronic, and photovoltaic properties by annealing under high selenium pressure, J. Appl. Phys. 79 (1996) 7293. doi:10.1063/1.361446.

[48] Ball Mill, http://en.wikipedia.org/wiki/Ball_mill.

[49] T. Arita, N. Suyama, Y. Kita, S. Kitamura, T. Hibino H. Takada, K. Omura, N. Ueno, and M. Murozono, in Conference Record of the IEEE Photovoltaic Specialists' Conference, 1988, Vol. 20, p. 1650.

[50] A. Vervaet, M. Burgelman, I. Clemminck and M. Casteleyn, in 10th European Photovoltaic Solar Energy Conference, Lisbon, Portugal, 1991, p. 900.

[51] T. Wada, Y. Matsuo, S. Nomura, Y. Nakamura, A. Miyamura, Y. Chiba, A. Yamada, M. Konagai, Fabrication of $Cu(In,Ga)Se_2$ thin films by a combination of mechanochemical and screen-printing/sintering processes, Phys. Status Solidi Appl. Mater. Sci. 203 (2006) 2593–2597. doi:10.1002/pssa.200669652.

[52] C.B. Murray, D. Norris, M.G. Bawendi, Synthesis and characterization of nearly monodisperse CdE (E= S, Se, Te) semiconductor nanocrystallites, J. Am. Chem. Soc. 115 (1993) 8706–8715. doi:10.1021/ja00072a025.

[53] B. Li, Y. Xie, J. Huang, Y. Qian, Synthesis by a solvothermal route and characterization of $CuInSe_2$ nanowhiskers and nanoparticles, Adv. Mater. 11 (1999) 1456-1459. doi: 10.1002/(SICI)1521-4095(199912)11:17<1456::AID ADMA1456>3.0.CO;2-3/epdf.

[54] X. Gou, F. Cheng, Y. Shi, L. Zhang, S. Peng, J. Chen, P. Shen, Shape-controlled synthesis of ternary chalcogenide $Znln_2S_4$ and $Culn(S,Se)_2$ nano-/microstructures via facile solution route, J. Am. Chem. Soc. 128 (2006) 7222–7229. doi:10.1021/ja0580845.

[55] D.L. Schulz, C.J. Curtis, R. a Flitton, H. Wiesner, J. Keane, R.J. Matson, M. Kim, P. a Parilla, R. Noufi, D.S. Ginley, Cu-In-Ga-Se Nanoparticle Colloids as Spray Deposition Precursors for $Cu(In,Ga)Se_2$ Solar Cell Materials, J. Electron. Mater. 27 (1998) 433–437. doi:10.1007/s11664-998-0173-5.

Chapter 3

Experimental and characterization techniques

In this chapter, we have described the various experimental methods and characterizations techniques in detail which was used to carry out the present research work. The chapter explains the preparation of CIGSe powder, ink formulation, deposition and annealing of films. The various properties of CIGSe powders and films were investigated using characterization techniques such as XRD, Raman, FE-SEM, TEM, EDS, XPS, UV-VIS-NIR, hall measurement and current-voltage (I-V) characteristics.

3.1. Experimental details

CIGSe film preparation using particle-based approach was performed as shown in **Fig. 3.1** and it involves several steps as follows:

1. Synthesize of CIGSe (powder) particles,
2. Formulation of ink using CIGSe particles,
3. Preparation of CIGSe films, and
4. Annealing of CIGSe films.

Fig. 3.1. Different steps involve in CIGSe film preparation process.

3.1.1. Synthesis of CIGSe particles (Step 1)

To synthesis CIGSe particles, we have employed two different process such as,

- One-pot heating up process and
- Hot injection process which we have explained in detail as below.

3.1.1.1. Synthesis of CIGSe submicron particles by one-pot heating-up process

The $CuIn_{0.7}Ga_{0.3}Se_2$ (CIGSe) submicron particles was synthesized via a facile one-pot heating-up process as shown in **Fig. 3.2**. In this typical procedure, 1 mmol of CuCl (99.995%), 0.7 mmol of $InCl_3$ (99.999%), 0.3 mmol of $GaCl_3$ (99.999%) and 2 mmol of elemental selenium (99.99%) were added into 10 mL of oleylamine (technical grade 70%) at room temperature **[1]**. The above mixture was heated to 240°C under nitrogen atmosphere and at this temperature the reaction time was maintained for 4 h. Once the reaction was terminated, the temperature of the solution was reduced to room temperature. When the temperature was reached to 100°C, 10 ml of chloroform (99.99%) was added to quench the reaction and 5 ml of ethanol (99.99%) was then added to precipitate the solution which was centrifuged at 4000 rpm for 20 min. The supernatant was discarded which contains unreacted precursor, solvent and by-products. The CIGSe powder was washed with ethanol and chloroform (1:1) ratio and centrifuged at 4000 rpm for 2 min **[1,2]**. This process was repeated for several times in order to get high-purity product. Then, the final product was dried at 90°C for 2 h in the oven and then used for further characterizations.

- The above experiment was repeated for various reaction temperatures such as 260, 280 and 300°C keeping the reaction time of 4h.
- The experiment was also repeated for different reaction time (1, 2, 4 and 6h) at 260°C.
- Furthermore, formation mechanism of CIGSe was studied in three steps by means of varying temperature and time such as 140°C for 1h (1st step), 210°C for 1h (2nd step) and 260°C for 4h (3rd step).

- Moreover, CIGSe powder was synthesized in gram-scale at 260°C for 4h.
- CIGSe powder was synthesized by varying Cu concentration in the solution such as 0.4, 0.6, 0.8, 1.0 and 1.2 mmol.

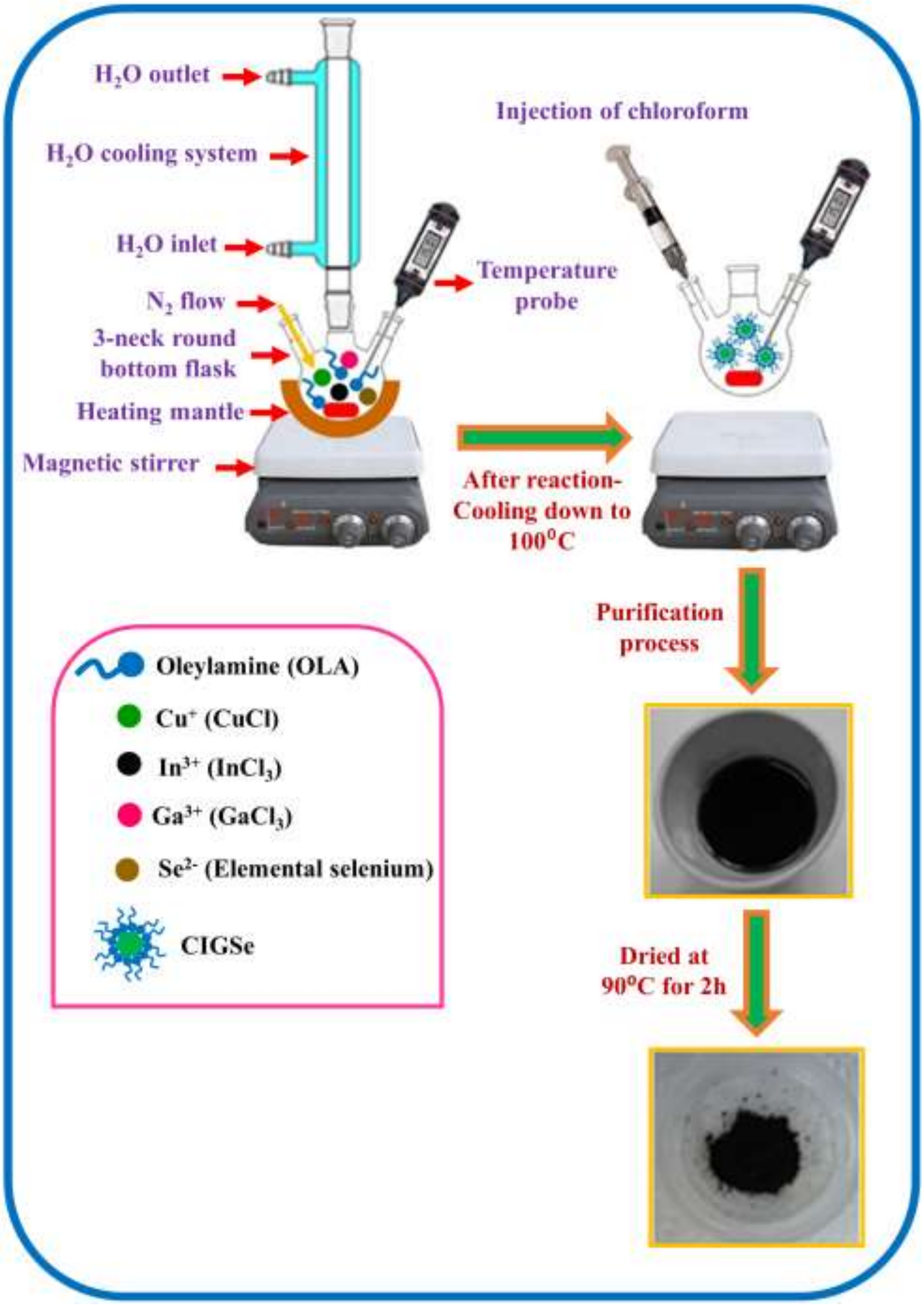

Fig. 3.2. Experimental procedure of CIGSe submicron particles synthesis by one-pot heating-up process.

3.1.1.2. Synthesis of CIGSe nanoparticles by hot injection process

We used hot injection process to synthesis the $CuIn_{0.7}Ga_{0.3}Se_2$ (CIGSe) nanoparticles as shown in **Fig. 3.3**. A typical procedure of CIGSe nanoparticles synthesis follows: 1 mmol of CuCl, 0.7 mmol of $InCl_3$, 0.3 mmol of $GaCl_3$ and 5 mL of oleylamine were mixed at room temperature and then sonicated for 2h at 40°C; afterward, we observe the precursors have completely dissolved. This solution was marked as solution A. Separately, 2 mmol of elemental selenium was added into 5 mL of oleylamine at room temperature. Then, the mixture heated to 200°C for 1h under N_2 atmosphere. Over the course of an hour, the solution gradually changed from colourless, to orange, and to brownish red because of the dissolution of Se powder in oleylamine. This solution, labelled as solution B. Once the Se, from solution B, was completely dissolved, the temperature decreased to 180°C and kept at that temperature. And then, the solution A was injected into solution B and the reaction was carried out at 180°C for 4h.

When the reaction was completed, the solution temperature was decreased to room temperature. To quench the reaction, 10 ml of chloroform was added to solution when the temperature was reached to 100°C. 5 ml of ethanol was then added to precipitate the solution and it was centrifuged at 4000 rpm for 20 min. The final solution was purified using the similar process as mentioned in **section 3.1.1.1**. Then, the final product was dried at 90°C for 2 h in the oven and then used for further characterization.

- The above experiment was repeated for several reaction temperatures such as 260, 240, 220 and 200°C with constant reaction time of 4h.
- At regular intervals, aliquots were withdrawn from 0 min to 24h at a constant temperature of 180°C to study the formation mechanism of CIGSe nanoparticle.

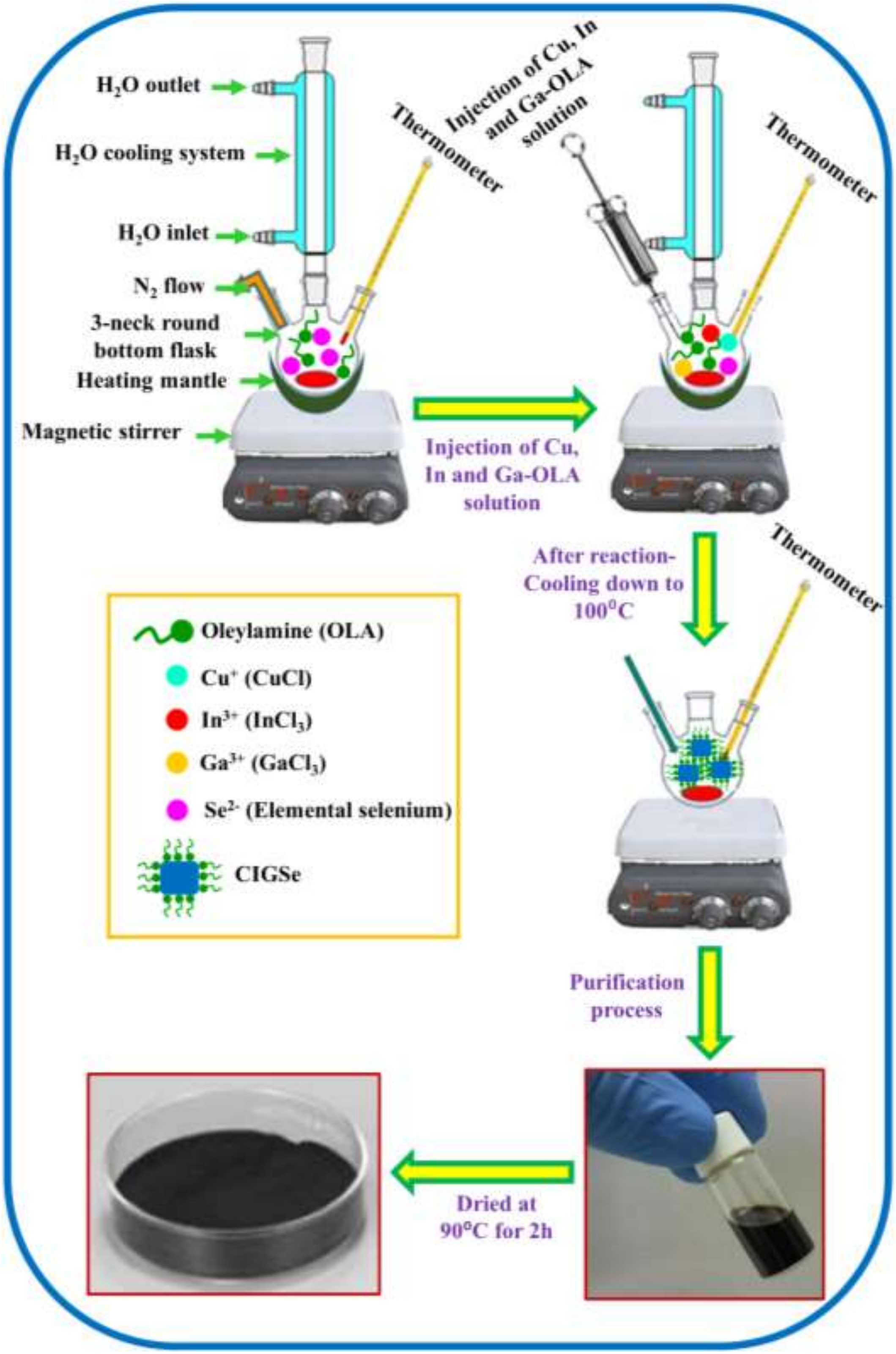

Fig. 3.3. Experimental procedure of CIGSe nanoparticles synthesis by hot injection process.

3.1.2. Formulation of CIGSe ink (Step 2)

Ink was formulated by dispersing the synthesized CIGSe powder in hexanethiol [3] (purity; 95%) as shown in Fig. 3.4. The important parameter of the CIGSe powder concentration was varied such as 100, 75 and 50 mg in 500 µL of hexanethiol. The aim of varying the CIGSe powder concentration was to get the film thickness around 1-1.5 µm with crack-free surface.

Fig. 3.4. Formulation of CIGSe ink.

3.1.3. Preparation of CIGSe films (Step 3)

3.1.3.1. Substrate

The temperature stability, thermal expansion coefficient and chemical stability are the most important properties of substrate material. Temperature stability is necessary to carry out deposition process at high temperature. A small mismatch in thermal expansion coefficient between substrate and film is needed to the thermal stress of deposited films. Chemical stability of substrate is important to prevent interdiffusion of material between film and substrate. Soda lime glass (SLG) is the standard substrate has been used in high-efficiency CIGSe solar cells [4]. SLG is relatively economical, chemically stable, and relatively hard and exhibits smooth surface. It has sufficient glass transition temperature (Tg) of 563°C [5] and thermal expansion coefficient of 9.5 ppm/K [6]. Another advantage of SLG is that Na from SLG diffuse into CIGSe film during the deposition process and improves the morphological and electrical properties [7,8].

3.1.3.2. Cleaning of substrate

The condition of the substrate before film deposition is very necessary for proper film adhesion. Also, substrate cleaning has significant role on the film growth characteristics **[9]**. The substrate cleaning process involves quite several steps as follows.

- Initially, substrates were cleaned ultrasonically with soap solution for 5 min.
- Ultrasonically agitated in distilled water for 10 min. Shock waves created in the solvent rendered the possible removal of residues.
- Thoroughly rinsed with ethyl alcohol in an ultrasonic bath for 10 min, which is followed by ultrasonic agitation in distilled water for 5 min.
- Subjected to ultrasonic agitation in acetone for 10 min to remove any other dirt followed by ultrasonic agitation in distilled water for 5 min.
- Surface treatment of the cleaned substrates was carried out in a solution of H_2SO_4 (> 95%, Aldrich) and H_2O_2 (50%, Botica Moderna) (2:1) for 2 to 3 min.
- Finally, the substrates were dried in nitrogen gas before film preparation.

3.1.3.3. Deposition of CIGSe ink by doctor blade method

The process of CIGSe film preparation as shown in **Fig. 3.5**. Prior to the film preparation, an adhesive scotch tape was used to cover the sides of the substrate which act as spacers. Film was deposited only in the scotch tape free area. Typically, a small amount of CIGSe ink (~15 µL) was dropped at one edge of SLG substrates (1” by 2” size). A quartz glass rod with diameter of 5 mm was used to sweep the CIGSe ink towards over the substrate. Typically, two coating were applied with alternative sweeping direction to obtain uniform films.

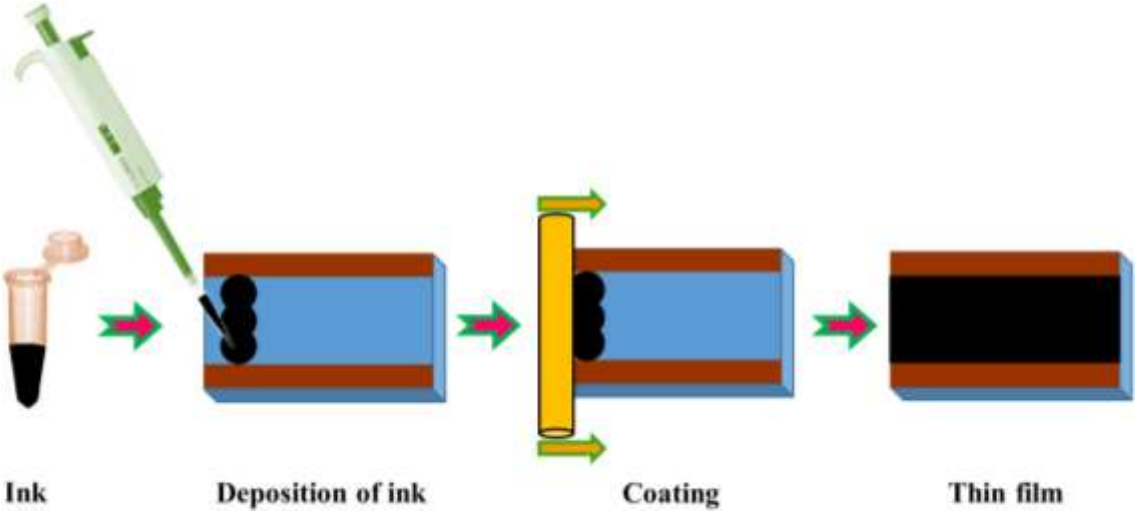

Fig. 3.5. Process of CIGSe film preparation.

3.1.4. Annealing of CIGSe films (Step 4)

3.1.4.1. Air annealing

As-prepared CIGSe films are subjected to annealing in two steps.

(i) Air annealing (at low temperature), and

(ii) Annealing under Ar/Se atmosphere called selenization process (at high temperature).

The CIGSe films were annealed in an ambient atmosphere at different temperatures 350 and 400^{o}C for 1 min. The furnace used for air annealing is shown in **Fig. 3.6**. The furnace consists of a quartz tube to place the sample, a resistive heater and a temperature controller.

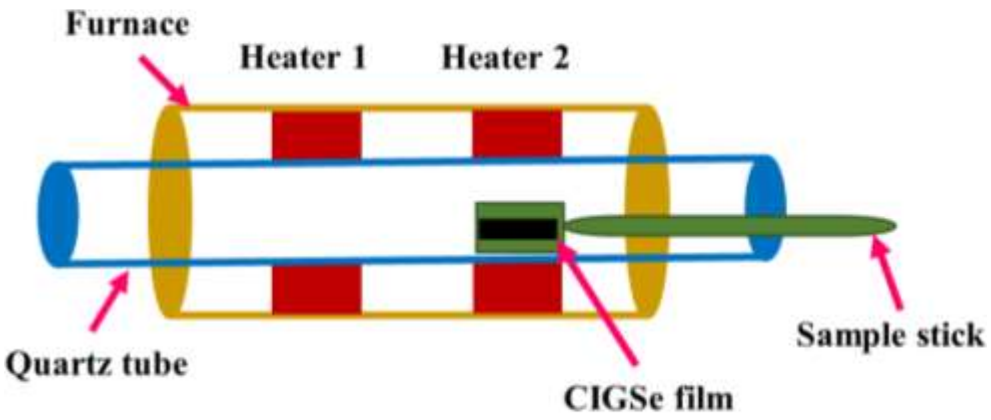

Fig. 3.6. Air annealing of CIGSe film.

3.1.4.2. Annealing under Ar/Se atmosphere

The selenization process was done in Ar/Se atmosphere using partially closed graphite box. The Se powder (50 mg) was introduced into the graphite box along with CIGSe film and loaded into the furnace. Fig. 3.7 shows the photograph of furnace and graphite box. The selenization process was done at 500°C for 20 mins. The selenization temperature was varied such as 500, 525 and 550°C by keeping the constant time of 20 mins.

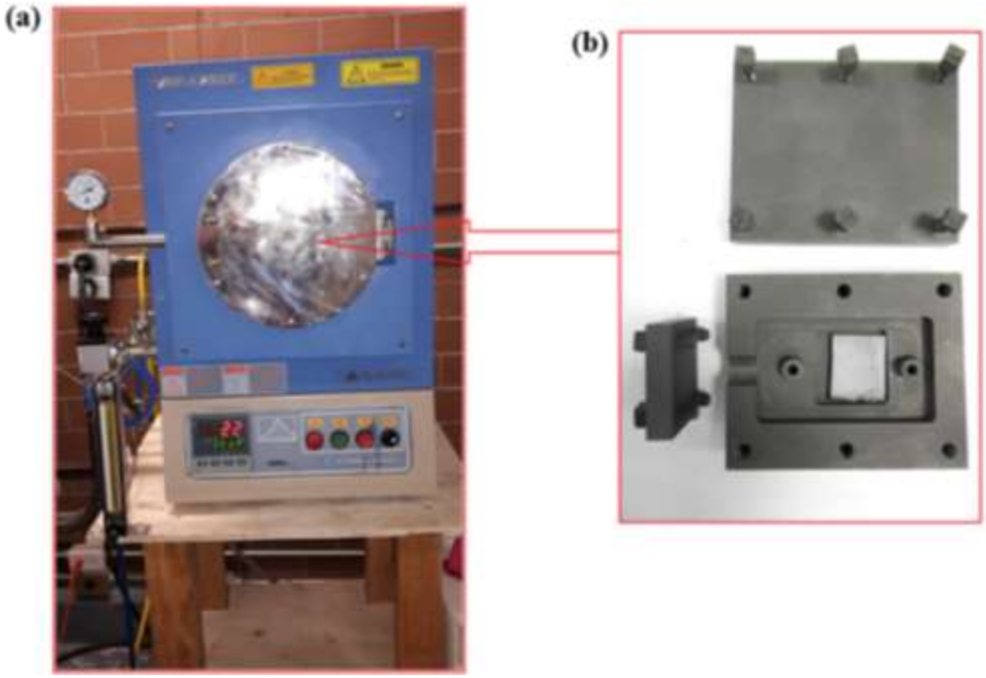

Fig. 3.7. Photograph a) selenization furnace and (b) graphite box.

3.2. Characterization techniques used in our studies

3.2.1. X-ray diffraction (XRD)

X-ray diffraction is a key technique to determine the phase and crystalline structure of materials. In XRD experiment, X-rays impinge upon the atomic planes involved in crystals and are scattered constructively to build patterns which account for the symmetry and the lattice dimensions. We can view the interaction of X-rays with a crystal due to reflection from the atomic planes as shown in Fig. 3.8.

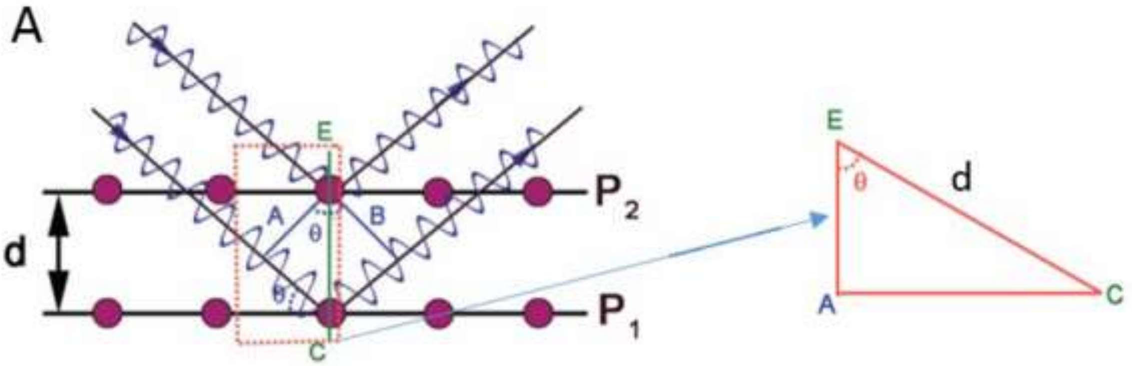

Fig. 3.8. Diffraction of X-ray with constructive interference, d is the distance between the diffraction planes.

Scattered X-rays 1 and 2 will be completely in phase if the Bragg relation is satisfied

$$n\lambda = 2d\, sin\Theta \qquad ---\rightarrow 3.1$$

where, n is the order of diffraction, λ is the wavelength of X-ray radiation, d is the interplanar distance and θ is the angle of incidence.

Crystallite size (L) is calculated from X-ray diffraction spectra using Scherrer formula [10]

$$L = \frac{K\lambda}{\beta\, cos\Theta} \qquad ---\rightarrow 3.2$$

where, K is a constant (0.9), λ is the X-ray wavelength (1.5406 Å), β is the Full Width Half Maximum (FWHM) and Θ is the diffraction angle.

The lattice constants ***a*** and ***c*** are calculated using the following formula: [11]

$$\frac{1}{d^2} = \frac{h^2+k^2}{a^2} + \frac{l^2}{c^2} \quad ----\rightarrow 3.3$$

In present work, CIGSe powder and films were analysed using Xpert-Pro Pananalytical X-ray Diffractometer from SEES which is shown in Fig. 3.9. XRD analysis was performed with CuKα (λ=1.5406 Å) in the θ-2θ mode with step size of 0.039.

Fig. 3.9. Photograph of Xpert- Pro Pan analytical X-ray diffractometer.

3.2.2. Raman spectroscopy (RS)

The Raman spectroscopy (RS) is one of the marvellous tools to determine single or polytype structures and secondary phases of the materials. The significance difference between RS and XRD is that the RS provides resonance bands for even amorphous materials, whereas X-ray powder diffraction does not. The spectroscopy works on inelastic scattering mechanism that when the laser beam strikes the sample, the atoms will get resonance to create modes in the crystal. If there are several resonance atoms misplaced that is, defects, the Raman spectrum may not give any bands corresponding to those missing atoms, unlike photoluminescence. However, it is exceptional for ordered vacancy compound (OVC) because its pattern is periodic with resonance atoms.

A typical experimental Raman spectroscopy used by several investigators is given in **Fig. 3.10**. The prism filters the laser beam from some other unwanted emission bands. The filtered laser beam is polarized by polarization rotator (Fresnel rhombus) and then focused on the sample through the short distance lens. The scattered light by the sample is collected through the same lens that is so-called back scattering configuration. The polarization analyser focuses the scattered light onto the entrance of the slit that is close to the M1 monochromator. The system is combination of M1,M2, and M3 monochromators in which M1 disperses the spectral lines of scattered light and then which are focused onto the edge slit close to the M2 to avoid stray light of laser beam that is called subtractive mode. The M2 monochromator restrains dispersion action of M1. The M1 and M2 obviously avoid the stray light in the main stream. The M3 monochromator does the spectral dispersion for the liquid nitrogen cooled CCD camera, which records the spectra with variation of frequency.

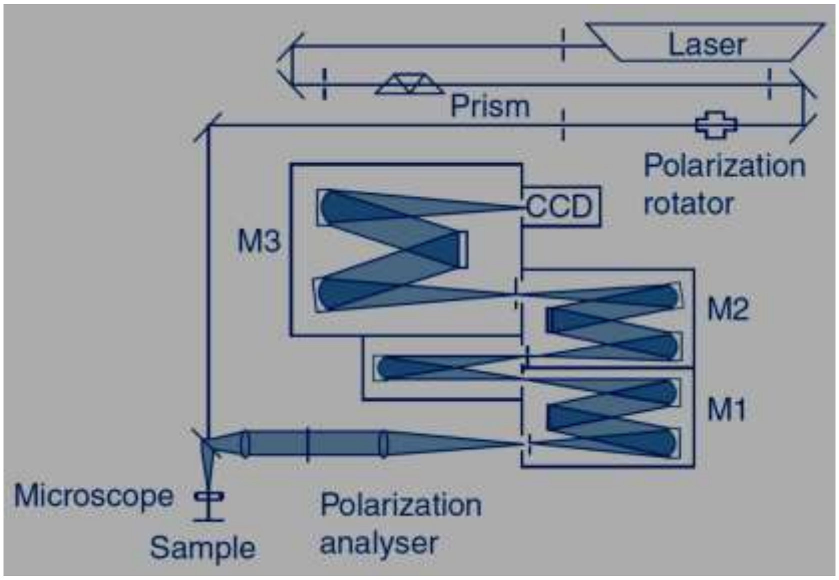

Fig. 3.10. A typical Raman spectroscopy experimental setup [12].

Tetragonal chalcopyrite structure of $CuInSe_2$ has 3 acoustic and 21 optical phonon modes. The phonon modes are represented by $\Gamma_{ac}=1B_2+1E$ for acoustic modes and $\Gamma_{opt}=1A_1+2A_2+3B_1+3B_2+6E$ for optical modes. Among optical modes, A_1, B_1, B_2 and E modes are Raman active. B_2 and E modes are infrared active if the incident radiation is polarised parallel and perpendicular to the tetragonal C-axis of the crystal. A_2 phonon modes are inactive. Different modes of $CuInSe_2$ (CISe) and $CuGaSe_2$ (CGSe) are tabulated in Table 3.1. Optical modes of CIGSe lies between that of CISe and CGSe depending on Ga/(In+Ga).

Table 3.1. Different optical phonon modes of CISe and CGSe.

Modes	CISe [13]	CGSe [14]
A_1	169	180
B_1^3	81	90
B_1^2	149	108
B_1^1	206	128
B_2^3	67/68	81/102
B_2^2	173/182	200/202

B_2^1	197/210	259/261
E^6	60/60	62.5/73
E^5	69/69	80.5/83.5
E^4	132/132	117/121
E^3	171/174	141/142
E^2	193/197	183/193
E^1	199/211	252/277

In the present work, Raman dispersion studies were made in Horiba–Jobin Yvon equipment as shown in **Fig. 3.11**, model LabRAM HR800 with He-Ne laser operated at 632 nm of 20 mW. To avoid heating of the sample and to filter plasma frequencies a D0.6 filter was employed which reduces power to 5 mW.

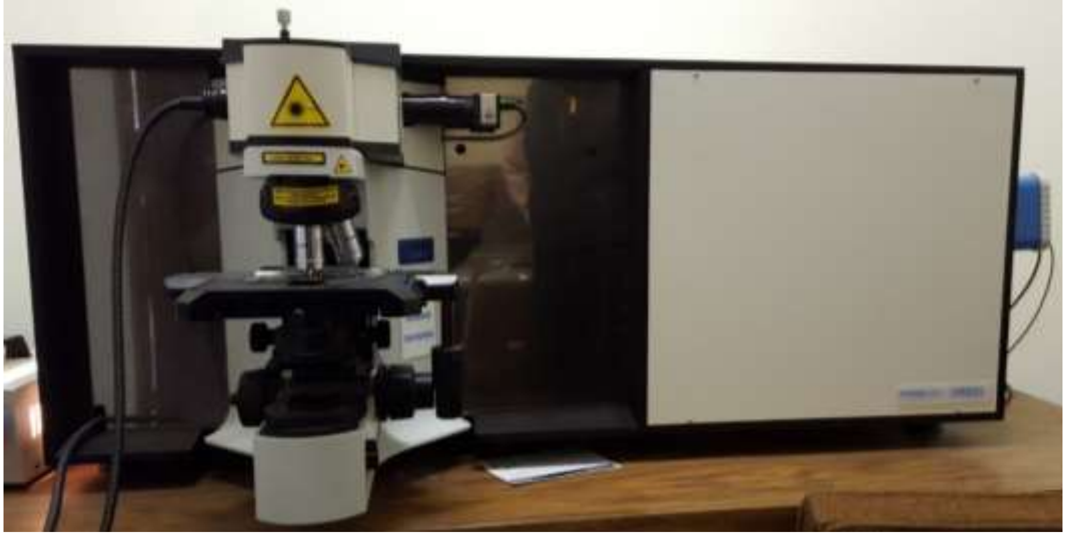

Fig. 3.11. Horiba–Jobin Yvon LabRAM HR800 equipment.

3.2.3. Field emission scanning electron microscopy (FE-SEM)

FE-SEM is a useful technique for the direct observation of surfaces, employed to predict the growth mechanisms leading to reminiscent structures. In a FE-SEM analysis, the areas or micro-volumes to be examined are irradiated with a fine electron beam produced by the electron gun and focussed by electron lenses as shown in Fig. 3.12. Scanning coils deflect this beam and sweeps it over the film surface. A cathode ray tube is scanned synchronously with the electron beam. Brightness of display tube is modulated by the signal which arises from interactions of the beam with film surface. The strength of this signal is thus translated into image contrast.

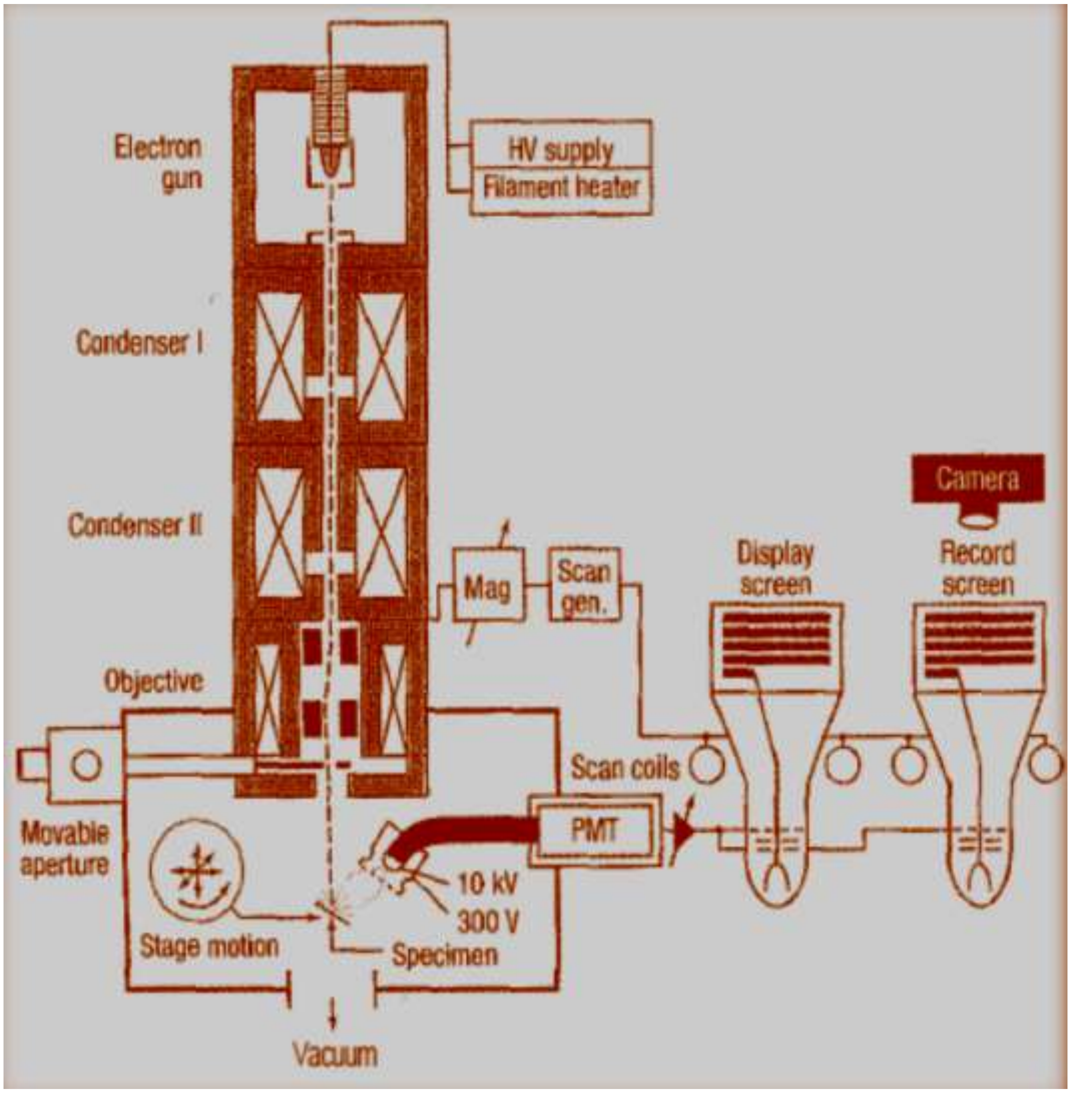

Fig. 3.12. Schematic diagram of FE-SEM.

The types of signals produced when electron beam impinges on specimen surface include secondary electrons, Auger electrons, characteristic X-rays and photons of various energies as shown in Fig. 3.13 (a). These signals are obtained from specific emission volumes within the samples as indicated in **Fig. 3.13 (b)**, which ultimately determines surface topography, crystallography, composition, etc.

In the present work morphology of the CIGSe powder and films surface and cross sectional images were analysed by a Carl Zeiss AURIGA FE-SEM workstation as shown in **Fig. 3.14**.

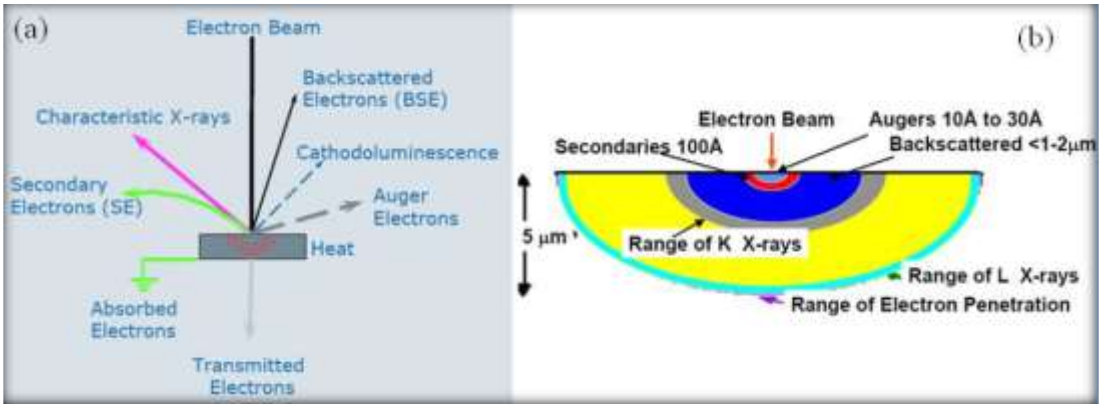

Fig. 3.13. (a) Electron beam interaction with specimen and
(b) Different signals from different volume of the sample by electron beam interaction.

Fig. 3.14. Carl Zeiss AURIGA FE-SEM workstation.

3.2.4. Energy dispersive spectroscopy (EDS)

Composition of all the deposited layers were determined using Bruker energy dispersive spectroscopy (EDS) system attached to a secondary electron microscope. An acceleration voltage of 10 kV was routinely used, which resulted in a penetration depth of ~1 μm into CIGSE films. EDS helps to determine the elemental contents in sample. In this technique, an energetic beam of electrons is allowed to be incident on the film. These incident electrons interact inelastically with both the inner shell electrons and outer shell electrons of the atoms of thin sample material generating X-rays as represented in Fig. 3.15. Outer shell electrons generate soft X-rays due to this interaction whereas innermost shells generate characteristic X-rays, which depend on energies of these shells and hence are characteristic of atoms radiating these X-rays. Hence by analysing the energy of these characteristic X-rays, typical of which are K_α, K_β, L_α, L_β etc., information about the type of atoms present in the sample and their concentration can be determined.

In this work, the composition of CIGSe powder and films are obtained using Bruker Ser 5010 X flash EDS detector used with Carls Zeiss HRSEM Auriga microscope from LANE. The EDS analysis of CIGSe powder and films are carried out at operating voltage of 15 kV.

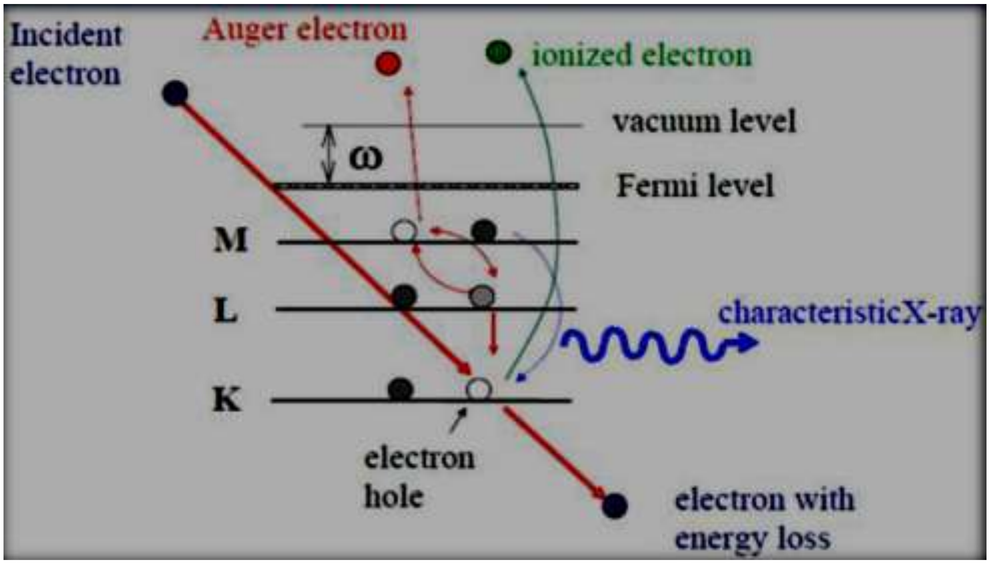

Fig. 3.15. Characteristic X-rays generation through interaction of electrons.

3.2.5. High resolution transmission electron microscopy (HR-TEM)

High resolution transmission electron microscopy (HR-TEM) is a powerful technique to probe the matter at its ultimate atomic level and nanoscale resolutions. Moreover, the technique associates also electron diffraction tool able to probe the crystallography such space group of the involved structure. Also, HR-TEM investigations provide explicit images of the system organization in nanoparticles, clusters, thin films etc.

The transmission electron microscope uses high energy electrons (typically 100 keV to 300 keV), generated by an electron gun through either heating (thermionic emission) or the application of an electric field (field emission) followed by acceleration through the applied accelerating voltage. HR-TEM observations were obtained using JEOL-ARM200F as shown in Fig. 3.16. It incorporated with a spherical aberration corrector for electron optic system as standard, has achieved a high-angle annular dark field-scanning transmission electron microscopy (HAADF-STEM) image resolution of 0.08 nm, the highest in the world among the commercial transmission electron microscopies.

Fig. 3.16. JEOL ARM200F.

3.2.6. X-Ray photoelectron spectroscopy (XPS)

X –ray photoelectron spectroscopy (XPS), or electron spectroscopy for chemical applications (ESCA), is a non-destructive spectroscopic technique for studying the surface of solids. Thus, this technique probes the composition of the samples on few nanometers close to the surface and possesses very high resolution to detect the involved elements even with very low concentrations (~ at 0.1 atomic percent abundance) except hydrogen. In XPS experiments, when a sample is placed in the path of X-rays beam with defined energy, all the electrons of atomic species with binding energies less than the energy of the X-rays are ejected, with a kinetic energy dependent on the incident X- ray and the binding energy of the atomic orbitals. The kinetic energies of these photoelectrons are measured by an energy analyser in a high resolution electron spectrometer to determine the concentrations of the elements present as shown in Fig. 3.17.

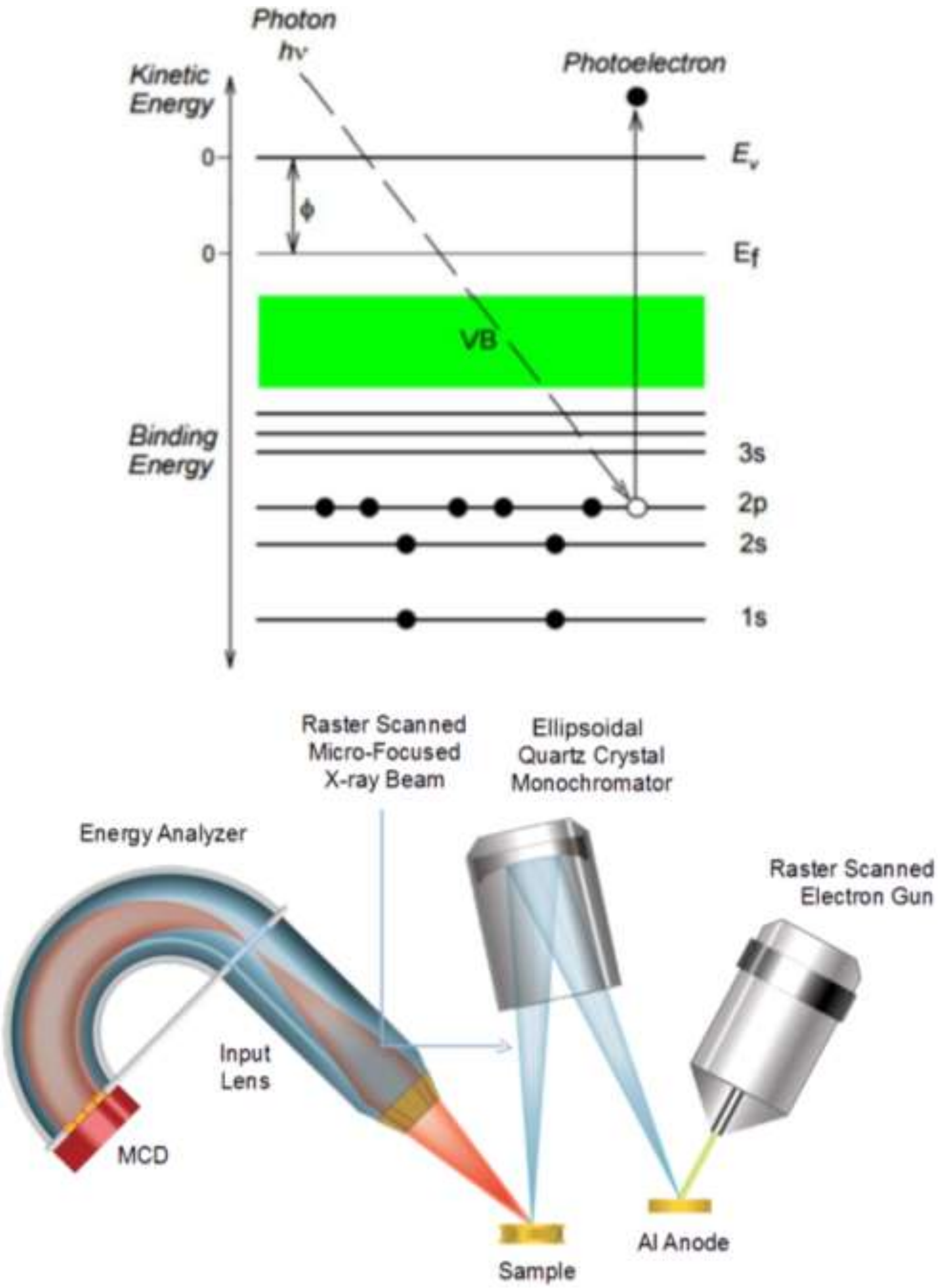

Fig. 3.17. Scheme showing the principles of x-ray photoelectron spectroscopy (XPS) [15].

The binding energy is indicative of a specific element and a particular structural feature of electron distribution. The electron binding energy of each of the emitted electrons can be determined by using an equation that is based on the work of Ernest Rutherford.

$$\mathrm{E}_{\mathrm{BE}} = h\nu - \mathrm{E}_{kinetic} - \phi \qquad ---\rightarrow \ 3.4$$

The relation between the binding energy and the kinetic energy is given by the **equation (3.4)** with E_b the binding energy of the electron, E_k its kinetic energy, hν is the X-ray photon energy and ϕ the spectrometer work function (constant for a given analyzer) **[15]**. The obtained information from XPS investigations are the following:

i. Elemental composition of the surface (top 0–10 nm usually)
ii. Eventual surface contaminant elements
iii. Chemical bonding and electronic states of the surface atoms
iv. Homogeneity of elemental composition across the top surface (or line profiling or mapping)
v. Homogeneity of elemental composition as a function of ion beam etching (or depth profiling)

The ability of this technique is used to study the enabled surfaces for bulk systems, thin films and nanostructures.

In this work, the XPS analysis was performed using a K-Alpha X-ray Photoelectron Spectrometer (XPS) System (Surface Analysis, Thermo Scientific). Monochromated, Microfocused Al Kα was used as an X-ray source type. The binding energy of C1s carbon was used for calibration.

3.2.7. Ultraviolet-visible-near infrared (UV-Vis-NIR) spectroscopy

Analysis of optical absorption spectra is one of the most productive tools for understanding and developing the band structure and energy gap of both crystalline and amorphous non-metallic materials. A double beam spectrometer arrangement is shown **Fig. 3.18**. A light source emits near ultra-violet, visible and near infrared covering the range from about 300 to 2500 nm. The combined output of the source is focused on to a diffraction grating. The slit only allows light of a very narrow range of wavelengths through into the rest of the spectrometer. By gradually rotating the diffraction grating, we can allow light from the whole spectrum through into the rest of the instrument.

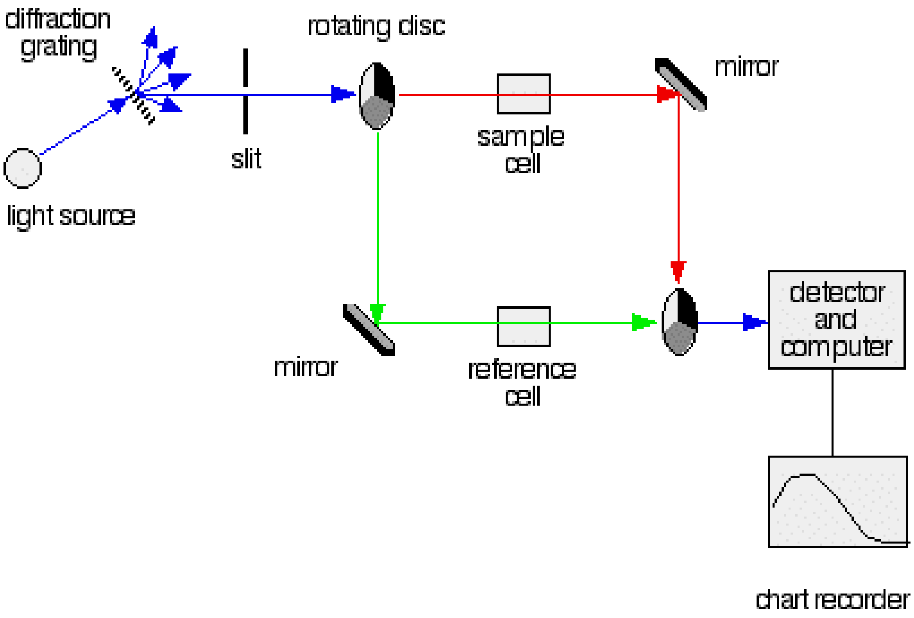

Fig. 3.18. Block diagram of double beam spectrophotometer.

The sample and reference cells are identical holders to hold different kind of samples. Detector converts the incoming light into a current, higher the current the greater the intensity of light. For each wavelength of light passing through the spectrometer, intensity of the light passing through the reference cell is measured. This is usually referred to as *I*o. Intensity of the light passing through the sample cell is also measured for that wavelength as *I*. If *I* is less than *I*o, then obviously the sample has absorbed some of the light. Absorbance of the sample (*A*) is given by:

$$A = log_{10}\frac{I_0}{I} \quad - - - \rightarrow 3.5$$

From the transmittance spectrum of a film, absorbance coefficient is calculated using the following expression,

Absorption coefficient

$$\propto = \frac{1}{t}\, ln \frac{1}{T} \quad - - - \rightarrow 3.6$$

where, t is the thickness of the film and T is the transmittance.

The type of bandgap of material is determined from the transition probability given by

$$\propto h\nu^{p} = A\left(h\nu - E_g\right) \quad - - - \rightarrow 3.7$$

Where A is a constant and p is a variable

If, p=2, the transition between the bands are allowed direct band gap transitions.
If p =2/3, the transition is prohibited direct band gap.
If p=1/2, the transition is allowed indirect band gap.
If p=1/3, the transition is prohibited indirect band gap.

To find bandgap of a direct bandgap semiconductor material, a graph of hυ over $(\alpha h\upsilon)^2$ has to be plotted and then a straight line to this is fitted. The constant of this equation is Eg. But in the case of indirect bandgap material a graph of hυ over $(\alpha h\upsilon)^{1/2}$ has to be plotted and do the same to get Eg.

In the present work, UV-visible-NIR absorption spectra of CIGSe films are analysed as a function of wavelength 400-2000 nm using JASCO V-670 UV-Vis-NIR spectrophotometer from SEES as shown in **Fig. 3.19**. Spectral distributions of transmittance are determined at room temperature. Substrate absorption was corrected by introducing an uncoated clean glass in the reference beam.

Fig. 3.19. JASCO V-670 UV-VIS-NIR Spectrophotometer.

3.2.8. Van der pauw method and hall studies

For measuring electrical resistivity, Van der Pauw [16] technique was employed. The Van der Pauw technique, due to its convenience, it is widely used in the semiconductor industry to determine the resistivity of uniform samples. As originally devised by Van der Pauw, one uses an arbitrarily shape, thin-plate sample containing four very small ohmic contacts placed on the periphery, preferably in the corners, of the plate. A schematic of a rectangular Van der Pauw configuration is shown in Fig. 3.20. Objective of the resistivity measurement is to determine the sheet resistance R_S. Van der Pauw demonstrated that, there are actually two characteristic resistances R_A and R_B, associated with the corresponding terminals as shown in Fig. 3.20. To obtain the two characteristic resistances, one applies a *dc* current I into contact 1 and out of contact 2 and measures the voltage V_{43} from contact 4 to contact 3 as shown in Fig. 3.20. Next, one applies the current I into contact 2 and out of contact 3 while measuring the voltage V_{14} from contact 1 to contact 4. R_A and R_B are calculated by means of the following expressions:

$$R_A = V_{43}/I_{12} \text{ and } R_B = V_{14}/I_{23} \dashrightarrow 3.8$$

R_A and R_B are related to the sheet resistance R_S through the Van der Pauw equation:

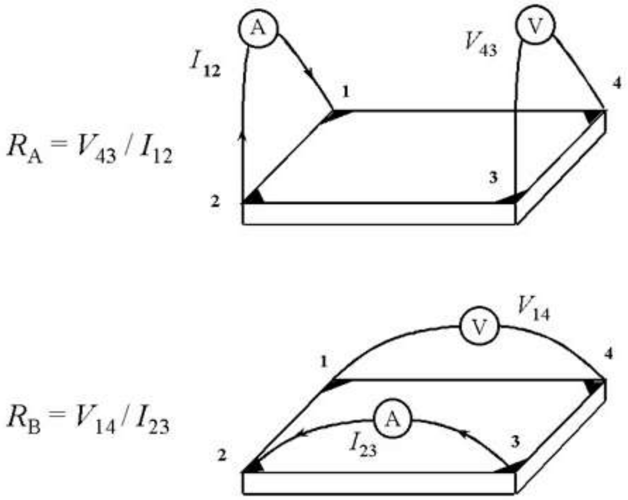

Fig. 3.20. Schematic of a Van der Pauw configuration used in the determination of the two characteristic resistances R_A and R_B.

$$exp\left(-\frac{\pi R_A}{R_S}\right) + \left(-\frac{\pi R_B}{R_S}\right) = 1 \quad ----\rightarrow 3.9$$

which can be solved numerically for R_S. The bulk electrical resistivity ρ can be calculated using the following relation if thickness (d) of the sample is known,

$$\rho = R_S d \quad ----\rightarrow 3.10$$

Hall Effect can be used to determine the signs of current carriers in metals and semiconductors. Hall coefficient is defined as **[17]**

$$R_H = \frac{E_y}{j_x H} \quad ----\rightarrow 3.11$$

where Ey, jx, and H are electric field, electric current density, and magnetic field strength, as shown in **Fig. 3.21 [18]**. If $R_H < 0$, then it indicates that the Ey is along $-y$ direction, and electric current carriers are negative particles (essentially they are electrons); if $R_H>0$, however, it indicates that Ey is along y direction, and electric current carriers are positive particles, which are called holes. By applying Drude model, we can write R_H as:

$$R_H = -\frac{1}{nec} \quad ---\rightarrow 3.12$$

where n, e, c are electric charge density, electron charge and speed of light respectively. Lower the carrier concentration, greater the magnitude of Hall coefficient. Measuring R_H is an important way of measuring the carrier concentration [17].

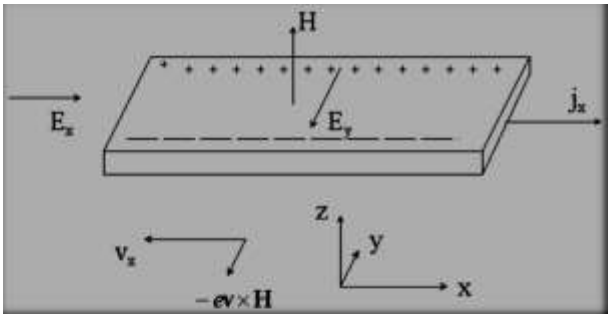

Fig. 3.21. Schematic of Hall effect experiment.

Hall measurement system Lakeshore 8407 with an applied magnetic field of 15 KG at room temperature has been used to analyse conductivity type, carrier concentration, mobility carrier and resistivity of CIGSe films (**Fig. 3.22**). To measure Hall effect, 100 nm thick circular gold contacts are deposited onto the CIGSe film by thermal evaporation method.

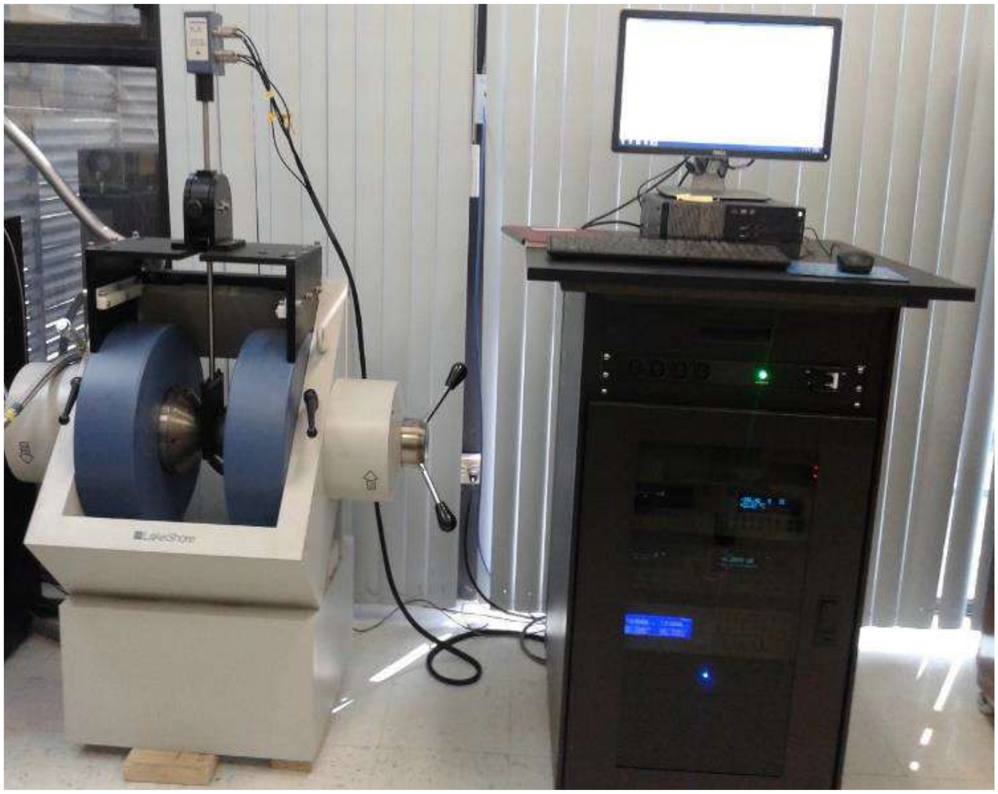

Fig. 3.22. Lakeshore 8407 Hall measurement system.

3.2.9. Current-voltage (I-V) characteristics

I-V characteristics of CIGSe films under dark and illumination are obtained using Keithley 4200-SCS semiconductor characterization system (Fig. 3.23) by applying voltage from -10 to +10V. To perform I-V measurement, 100 nm thick Au contacts are deposited on the CIGSe film by thermal evaporation technique. The sample is placed on the sample holder and contacts were made to connect two probes. Photocurrent is measured by illuminating the films using a light source of 300 W.

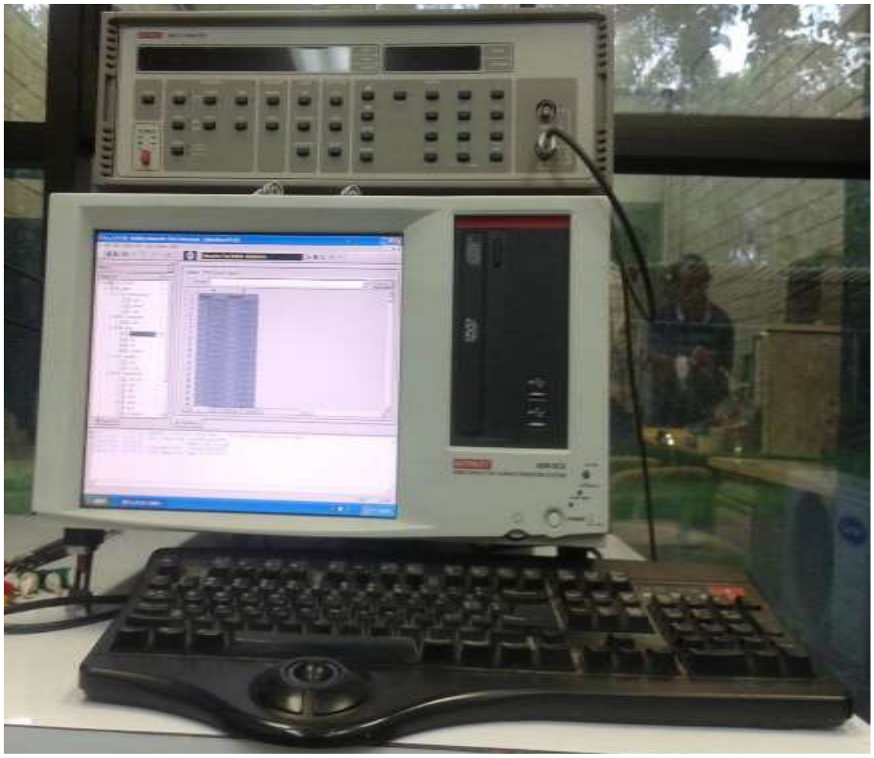

Fig. 3.23. Keithley 4200-SCS semiconductor characterization system.

References

[1] M. Latha, R.A. Devi, S. Velumani, G. Oza, P. Reyes-Figueroa, M. Rohini, I.G. Becerril-Juarez, J. Yi, Synthesis of $CuIn_{1-x}Ga_xSe_2$ Nanoparticles by Thermal Decomposition Method with Tunable Ga Content, J. Nanosci. Nanotechnol. 15 (2015) 8388–8394. doi:10.1166/jnn.2015.11473.

[2] M.G. Panthani, V. Akhavan, B. Goodfellow, J.P. Schmidtke, L. Dunn, A. Dodabalapur, P.F. Barbara, B. a. Korgel, Synthesis of $CuInS_2$, $CuInSe_2$, and $Cu(In_xGa_{1-x})Se_2$ (CIGS) nanocrystal "inks" for printable photovoltaics, J. Am. Chem. Soc. 130 (2008) 16770–16777. doi:10.1021/ja805845q.

[3] S. M. McLeod, C. J. Hages, N. J. Carter, R. Agrawal, Synthesis and characterization of 15% efficient CIGSSe solar cells from nanoparticle inks, Prog. Photovolt: Res. Appl. 23 (2015) 1550–1556. doi: 10.1002/pip.2588/full.

[4] A. Bosio, N. Romeo, A. Podestà, S. Mazzamuto, V. Canevari, Why $CuInGaSe_2$ and CdTe polycrystalline thin film solar cells are more efficient than the corresponding single crystal, Cryst. Res. Technol. 40 (2005) 1048–1053. doi:10.1002/crat.200410484.

[5] https://en.wikipedia.org/wiki/Soda-lime_glass.

[6] F. Kessler, D. Rudmann, Technological aspects of flexible CIGS solar cells and modules, Sol. Energy. 77 (2004) 685–695. doi:10.1016/j.solener.2004.04.010.

[7] Q. Guo, G. M. Ford, R. Agrawal, H. W. Hillhouse, Ink formulation and low-temperature incorporation of sodium to yield 12% efficient $Cu(In,Ga)(S,Se)_2$ solar cells from sulfide nanocrystal inks, Prog. Photovolt: Res. Appl. 21 (2013) 64–71. doi: 10.1002/pip.2200/full.

[8] L. Kronik, D. Cahen, H. Schock, Effects of sodium on polycrystalline $Cu(In,Ga)Se_2$ and its solar cell performance, Adv. Mater. 10 (1998) 31–+. doi:10.1002/(SICI)1521-4095(199801)10:1<31::AID-ADMA31>3.0.CO;2-3.

[9] K. Seshan, "Ion Beam Deposition", in Handbook of Thin Film Deposition Processes and Techniques, William Andrew, NY (2002). doi: 9780815514428.

[10] A. Monshi, M.R. Foroughi, M.R. Monshi, Modified Scherrer equation to estimate more accurately nano-crystallite size using XRD, World J. Nano Sci. Eng. 2 (2012)

154. doi:10.4236/wjnse.2012.23020.

[11] A. Ben Marai, J. Ben Belgacem, Z. Ben Ayadi, K. Djessas, S. Alaya, Structural and optical properties of $CuIn_{1-x}Ga_xSe_2$ nanoparticles synthesized by solvothermal route, J. Alloys Compd. 658 (2016) 961–966. doi:10.1016/j.jallcom.2015.10.287.

[12] Subba Ramaiah Kodigala, “Thin Films and Nanostructures $Cu(In_{1-x}Ga_x)Se_2$ Based Thin Film Solar Cells”, vol. 35, Academic Press 2010. doi: 9780123736970.

[13] J. Łażewski, H. Neumann, K. Parlinski, G. Lippold, B.J. Stanbery, Lattice dynamics of CuAu-ordered $CuInSe_2$, Phys. Rev. B. 68 (2003) 144108. doi:10.1103/PhysRevB.68.144108.

[14] D. Papadimitriou, N. Esser, C. Xue, Structural properties of chalcopyrite thin films studied by Raman spectroscopy, Phys. Status Solidi. 242 (2005) 2633–2643. doi:10.1002/pssb.200541132.

[15] D. Briggs, C. D. Wanger, W. M. Riggs, L. E. Davis, J. F. Moulder and G. E.Muilenberg Perkin-Elmer Corp., Handbook of X-ray Photoelectron Spectroscopy, Physical Electronics Division, Eden Prairie, Minnesota, USA, 1979. 190 pp. Surf. Interface Anal. 3 (1981). doi: 10.1002/sia.740030412/abstract.

[16] L.J. van der Pauw, A method of measuring the resistivity and hall coefficient of discs of arbitrary shape, Philips Res. Reports. 13 (1958) 1–9. doi:citeulike-article-id:8438442.

[17] C. Kittel, “Introduction to Solid State Physics”, John Willey & Sons, Inc. USA, 7th edition: 1995, pp. 164. doi: http://www.unige.ch/sciences/physique/tp/tpi/Liens/Protocoles/Complements/Charls%20Kittel%20Intro%20Solid%20State%20Physics.pdf

[18] L. Ma, Q. Zhao, C. Chen, Holes in Hall Effect, Lat. Am. J. Phys. Educ. Vol. 3 (2009) 48. doi: http://www.lajpe.org/jan09/08_Lianxi_Ma.pdf.

Chapter 4

Synthesis of CIGSe submicron particles by one-pot heating-up process

In this chapter, we discuss about the synthesis of Cu(In,Ga)Se_2 (CIGSe) submicron particles by a facile one-pot heating-up process, where we studied the effect of reaction parameters such as reaction temperature and reaction time. Besides, the reaction mechanism of CIGSe was studied. Moreover, we tested the suitability of our strategy for large-scale production of CIGSe powder by carrying out of gram-scale synthesis. Furthermore, the effect of copper concentration was investigated. Various properties of CIGSe was examined using characterization techniques such as XRD, Raman, FE-SEM, TEM, EDS and UV-VIS-NIR.

4.1.Synthesis of CIGSe submicron particles

CIGSe submicron particles were synthesized by optimizing the most important reaction parameters such as reaction temperature and reaction time. The prime motive of this optimization is to get single phase CIGSe with less reaction time while maintaining stoichiometric composition. We have successfully synthesized CIGSe submicron particles at 260°C with reaction time of 4h.

4.1.1. Influence of reaction temperature

The structural analysis of synthesized CIGSe samples with different reaction temperature is shown in **Fig. 4.1**. The observed peaks from the **Fig. 4.1(a)** correspond to (112), (103), (211), (213), (220) and (312) planes which are consistent with chalcopyrite crystal structure of CIGSe **(JCPDS 35-1102)** for all the samples. As the reaction temperature increases, all the observed diffraction peaks shifted to lower 2Ɵ values. We can see the peak shift clearly from the **Fig. 4.1(b)** which shows the magnified view of (112) plane for different reaction temperature. The observed lower 2Ɵ peak shift is due to decrement in the Ga content which evidenced from EDS composition analysis **(Fig.**

4.4). As can be seen in Fig. 4.2, A_1 mode peak of chalcopyrite CIGSe was observed at around 173.61 cm^{-1} which arises due to vibration of Se atoms with motionless neighboring cations of Cu, In, and Ga [1]. As the reaction temperature increases, the A_1 mode peak is shifted towards lower wavenumber due to decreases in Ga content which is in good agreement with XRD analysis as discussed previously. Additionally, the B_2/E mode of CIGSe peak was observed for all the samples which represents the vibration of anions and cations together [2]. The peak observed at 258 cm^{-1} [3–5] correspond to CuSe phase which is due to Cu-rich composition in the sample prepared at 240°C as can be seen in Fig. 4.4 (b).

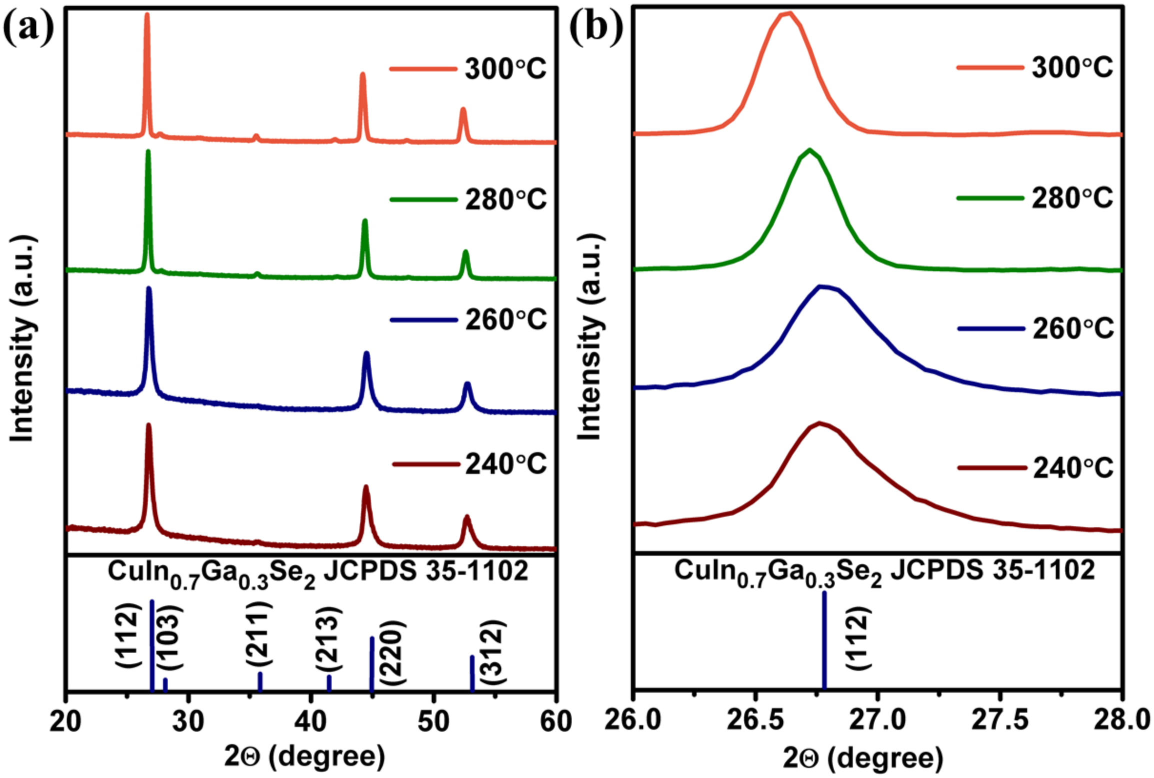

Fig. 4.1. CIGSe samples synthesized at different reaction temperature (a) XRD pattern and (b) Magnified view of (112) plane.

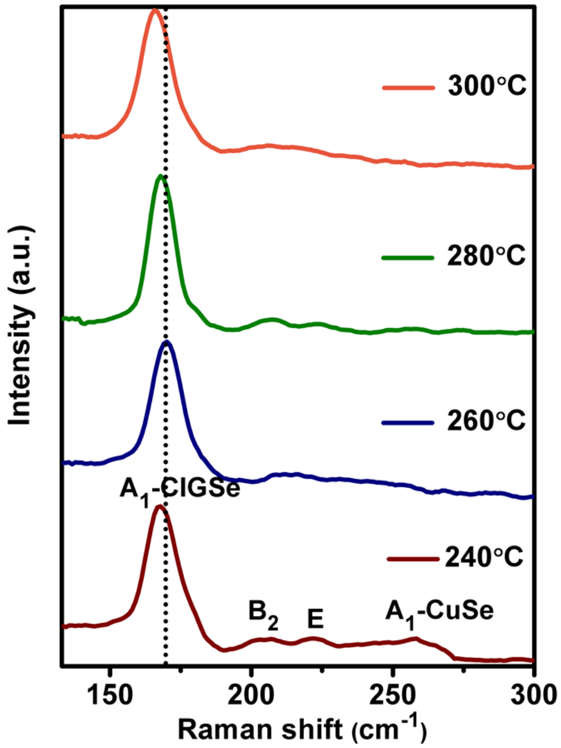

Fig. 4.2. Raman spectra of CIGSe samples synthesized at different reaction temperature.

The lattice constants ***a*** and ***c*** were calculated from the XRD data for different reaction temperature using the following formula: [6]

$$\frac{1}{d^2} = \frac{h^2+k^2}{a^2} + \frac{l^2}{c^2} \quad \dashrightarrow (1)$$

where h, k, and l are miller indices, ***a*** and ***c*** are lattice constants and d is the inter-plane distance.

The inter-plane distance was calculated using Bragg's diffraction equation:

$$d = \frac{n\lambda}{2\sin\theta} \quad \dashrightarrow (2)$$

where n is a positive integer, λ is wavelength (1.5405 Å) and ϴ is Bragg's angle.

With increases in the reaction temperature, lattice constants ***a*** and ***c*** increased linearly as shown in Fig. 4.3. The increases in the lattice parameters are due to substitution of bigger ionic size of In (0.62 Å) for smaller ionic size of Ga (0.47 Å) which enlarges the unit volume of the cell.

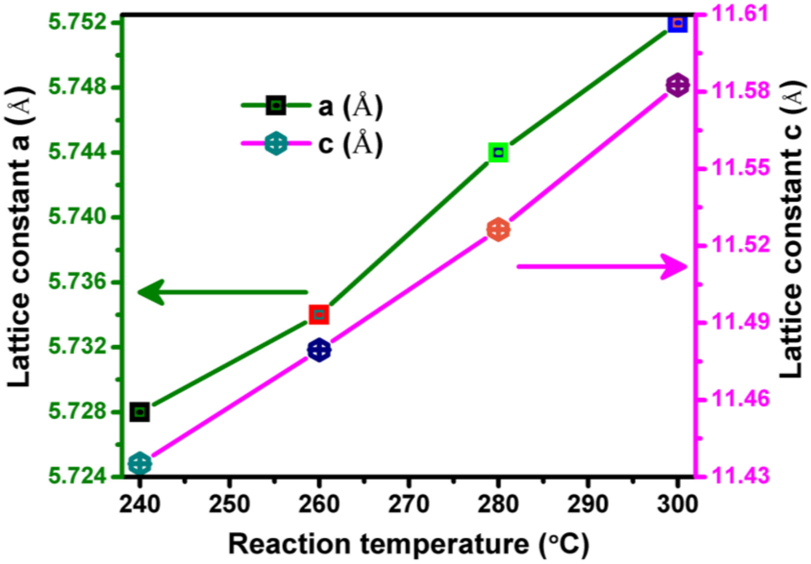

Fig. 4.3. Variation in the lattice constants ***a*** and ***c*** as a function of reaction temperature.

The EDS composition of synthesized CIGSe samples with different reaction temperature is shown in **Fig. 4.4(a)**. With increases in the reaction temperature, the Ga and Cu contents decreased while In and Se contents increased. When the reaction temperature was less than 260^{0}C, the Cu-rich composition was obtained which could be due to high reactivity of Cu at low temperatures. Further increasing the reaction temperature, Ga-poor composition attained due to evaporation of Ga. **Fig. 4.4(b)** shows the compositional ratios of Cu/(In+Ga) and Ga/(In+Ga). The Ga/(In+Ga) and Cu/(In+Ga) ratio were decreased as the reaction temperature increases. Therefore, the sample prepared at 260^{0}C showed stoichiometric composition which is very close to the targeted value.

UV-VIS-NIR absorption spectra of synthesized CIGSe samples with different reaction temperature is shown in **Fig. 4.4(c)**. From which, the absorption initiates at the near infrared region and increased gradually in the UV-Visible region for all the samples **[7,8]**. In addition to that, there is a redshift towards higher wavelength as the reaction temperature increases. The Tauc relation is used to calculate the optical band gap by extrapolating the $(\alpha h\nu)^2$ vs hν as shown in Fig. 4.4(d). The calculated band gap values of the synthesized CIGSe samples were 1.38, 1.25, 1.16 and 1.02 eV for 240, 260, 280 and 300^0C respectively. This behaviour could be due to decrement in the Ga content which is in good agreement with structural and compositional results. The band gap of 1.25 eV obtained at 260^0C, is suitable for solar cell applications [9][10].

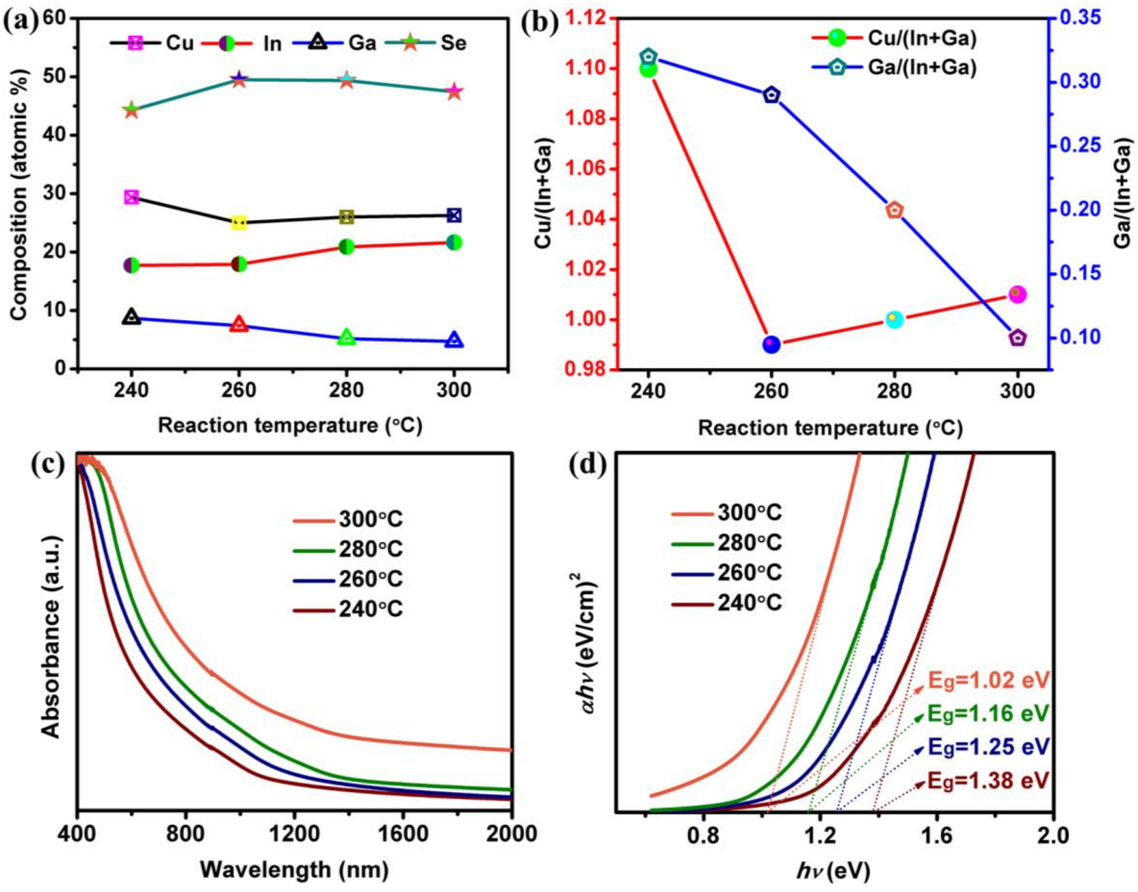

Fig. 4.4. CIGSe samples synthesized at different reaction temperature (a) EDS composition (b) corresponding Cu/(In+Ga) and Ga/(In+Ga) ratios, (c) UV-VIS-NIR absorption spectra and (d) Corresponding band gap spectra.

FE-SEM micrographs of synthesized CIGSe samples at different reaction temperature are shown in Fig. 4.5. With increases in the reaction temperature, morphology of the particles changed from hexagonal flake-like (up to 280^0C) to prism like shape (300^0C).

Besides, the particles size decreased from 1.3 to 0.4 μm, due to increases in the nucleation rate which is responsible for the smaller particle size [11]. The changes in the morphology from hexagonal flake to prism could be due to variation in the composition. Kim et al. [12] have also observed that the morphology of CIGSe particles was changed from spherical to tube-like shape by changing the composition. From the above results, we conclude that the CIGSe sample synthesized at 260^{0}C showed pure phase, stoichiometric, hexagonal flake-like shape with band gap energy of 1.25 eV.

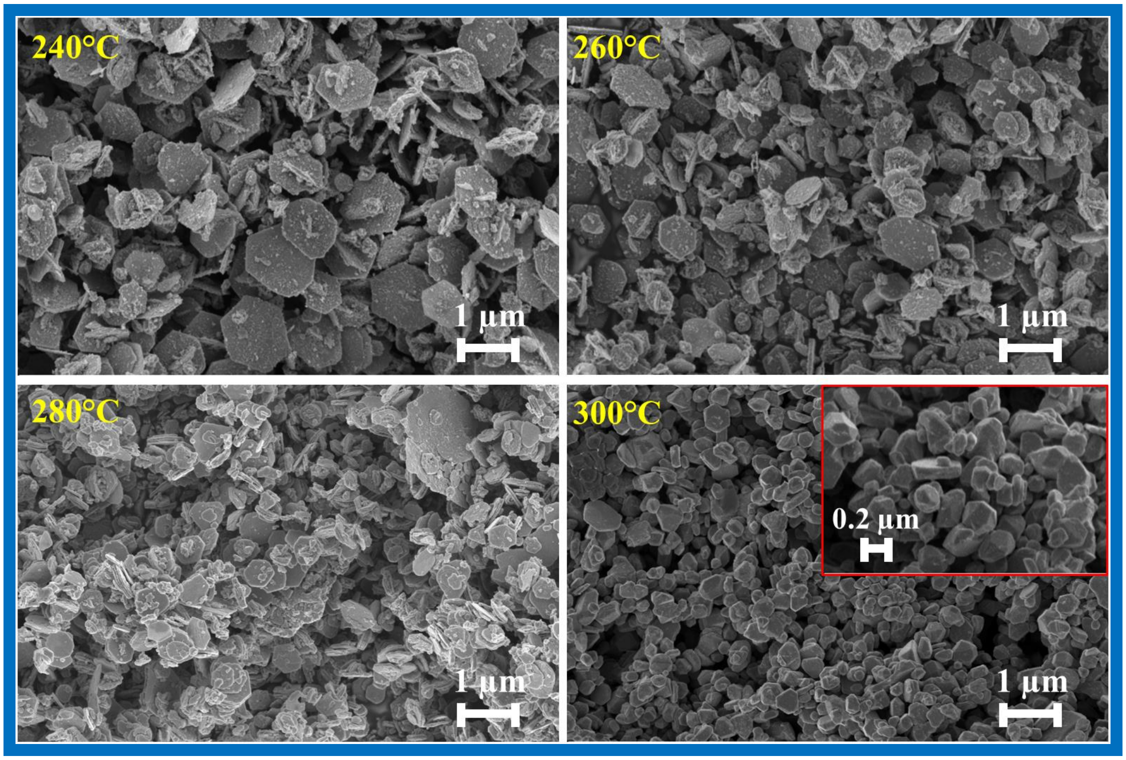

Fig. 4.5. FE-SEM micrographs of synthesized CIGSe samples at different reaction temperature.

4.1.2. Influence of reaction time

The CIGSe sample synthesized at 260°C showed pure phase, stoichiometric composition and band gap energy of 1.25 eV, as we discussed in the previous section. So, we have taken this condition for further experiments. Herein, the reaction time was varied from 1 to 6h to study their influences on the structural, compositional, optical and morphological properties of CIGSe. The XRD spectra of CIGSe samples synthesized at 260°C for different reaction time are shown in **Fig. 4.6(a)**. From the spectra, the chalcopyrite crystal structure of CIGSe peaks was observed which matches well with **JCPDS 35-1102**. With increases in the reaction time, the diffraction peaks shifted towards higher 2ϴ values which is due to increment in the Ga content as evidenced from EDS analysis **[Fig. 4.9(a)]**. To see the peak shift clearly, magnified view of (112) plane is shown in **Fig. 4.6(b).** Raman spectra **(Fig. 4.7)** showed the A_1 mode peak which represents the vibration of Se atoms with cations are being at rest **[1]**. In addition to that, B_2/E modes of CIGSe was observed which arises due to the vibration of anion and cations together **[2]**. As the reaction time increases, the Raman peaks were shifted towards higher wavenumber which is in good accordance with the XRD results as discussed earlier. Further increasing the reaction time to 6h, significant difference was not observed in the peak position.

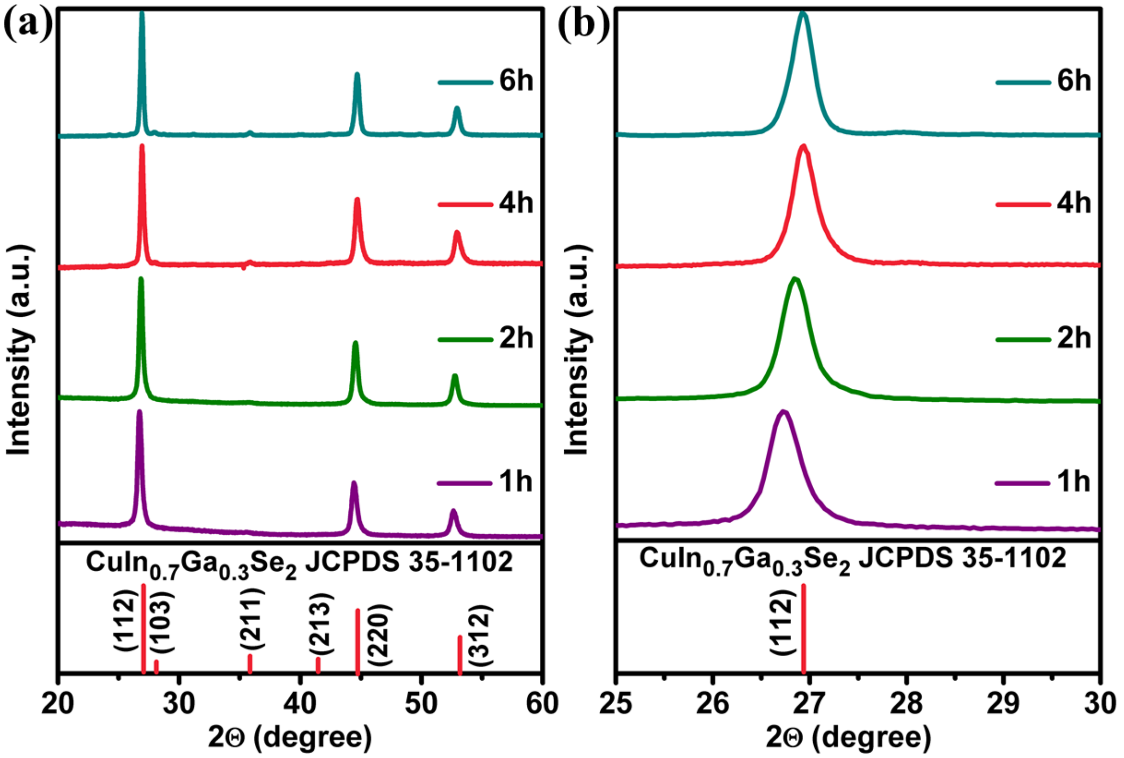

Fig. 4.6. CIGSe samples synthesized at different reaction time (a) XRD pattern and (b) Magnified view of (112) plane.

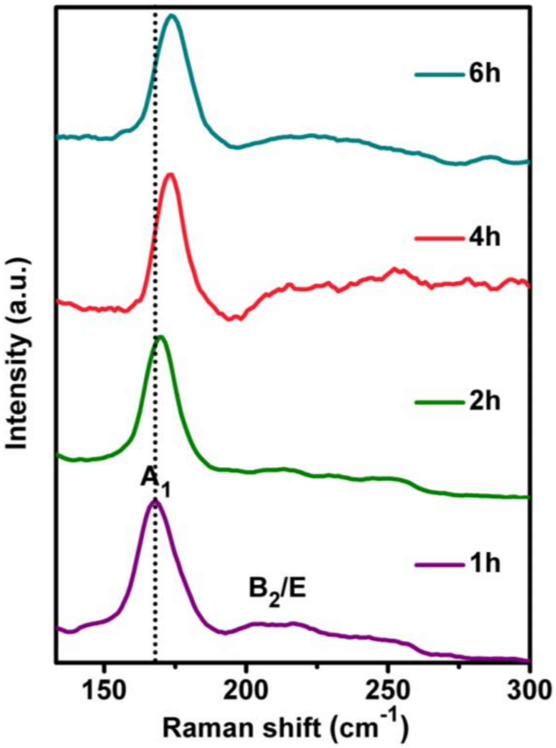

Fig. 4.7. Raman spectra of CIGSe samples synthesized at different reaction time.

The lattice constants ***a*** and ***c*** were calculated using the formula as described in the previous section. As can be seen in **Fig. 4.8**, the lattice constants ***a*** and ***c*** were decreased linearly as a function of reaction time, which is in good agreement with Vegard's law. The decreases in the lattice constants is due to substitution of the smaller ionic radius of Ga (0.47 Å) for the bigger ionic radius of In (0.62 Å) which leads to shrinkages in the unit volume **[6,13]**.

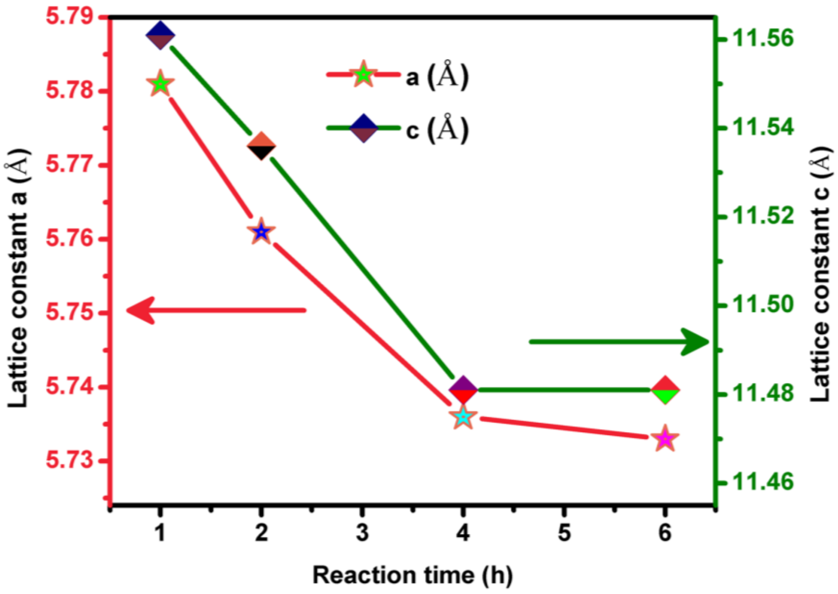

Fig. 4.8. Variations in the lattice constants ***a*** and ***c*** as a function of reaction time.

EDS composition of CIGSe samples synthesized at different reaction time are shown in **Fig. 4.9(a)**. As the reaction time proceeds, In and Se content decreased while Cu and Ga content increased. The Ga/(In+Ga) and Cu/(In+Ga) ratios were increased with increases in the reaction time as shown in the **Fig. 4.9(b)**. The composition obtained at 4h is very close to the targeted value. The optical absorption spectra of synthesized CIGSe samples at different reaction time are shown in **Fig. 4.9(c)**. The absorption started in the near infra-red region and gradually raised towards UV-Visible region for all the samples. There is a blue shift towards lower wavelength which indicates the increment in the Ga content as the reaction time increases **[8]**. The band gap was calculated using Tauc plot by extra plotting the hν versus $(\alpha h\nu)^2$ as shown in **Fig. 4.9(d)**. The calculated band gap values for 1, 2, 4 and 6h were 1.01, 1.19, 1.25 and 1.29 eV respectively. As the reaction time increases, the band gaps were increased which is due to increment in the Ga content **[6,8]**. The sample prepared at 4h showed a band gap of 1.25 eV and this is ideal value for absorber layer in CIGSe thin film solar cell applications **[10]**.

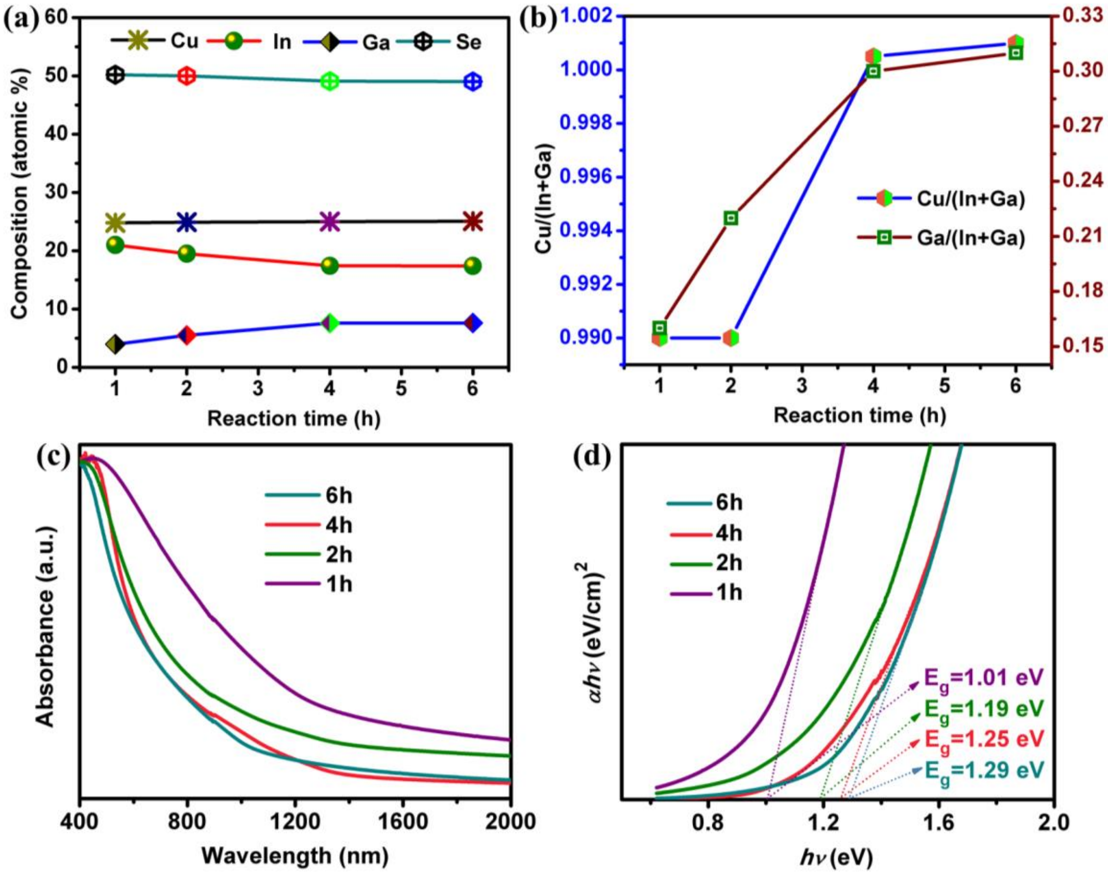

Fig. 4.9. a) EDS composition, b) Ga/(In+Ga) and Cu/(In+Ga) ratios, c) UV-VIS-NIR absorption spectra and d) Corresponding band gap spectra.

FE-SEM micrographs of CIGSe samples synthesized at different reaction time are shown in **Fig. 4.10**. When the reaction time was at 1h, irregular shape of the particles were observed with size varies from 50 to 300 nm. By prolonging the reaction time to 2h, the particles started to aggregate in order to reduce an interfacial energy and grew in bigger size from 100 to 500 nm. Hexagonal flake-like shape of the particles with size ranges from 0.7 to 1 µm was obtained at 4h. Further increases in reaction time up to 6h, the size of the hexagonal flakes were increased from 1 to 1.2 µm. According to the FE-SEM micrographs observations, the Ostwald ripening process could be proposed for the formation of CIGSe hexagonal flakes. Firstly, small sized irregular particles in relatively wide size ranges were formed and these small particles could serve as seeds to form micro-particles at the expense of smaller particles through the Ostwald ripening **[14,15]**. On the basis of structural, compositional, morphological and optical analysis; the CIGSe sample synthesized at 260^{0}C for 4h showed pure phase, hexagonal flake-like shape, stoichiometric and band gap energy of 1.25 eV among other conditions.

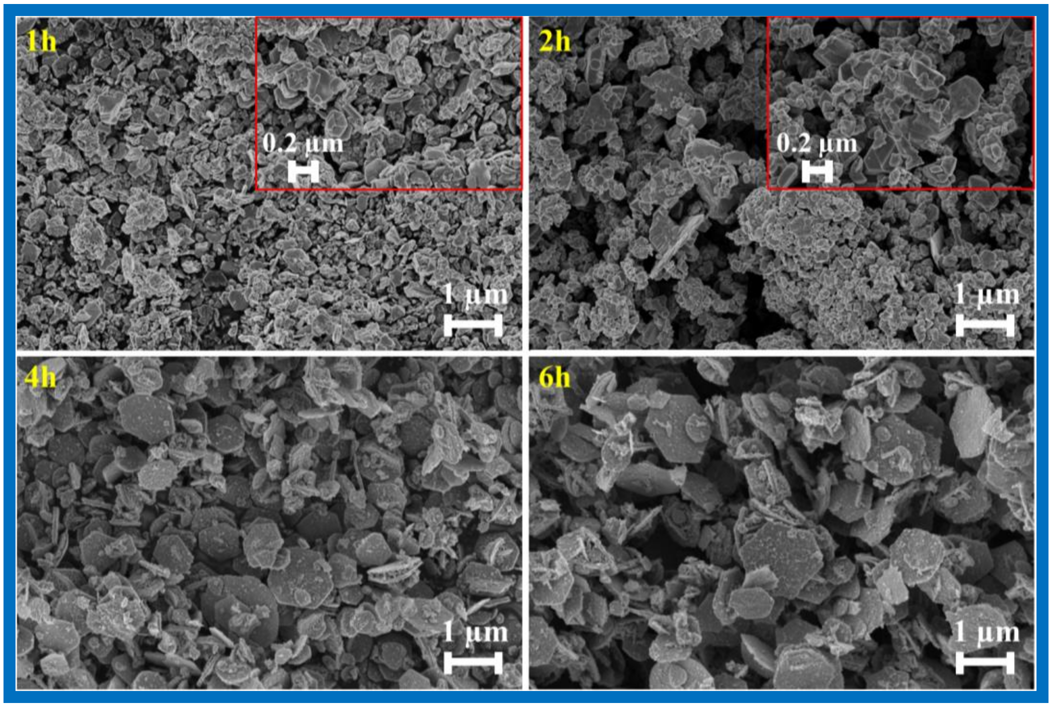

Fig. 4.10. FE-SEM micrographs of synthesized CIGSe samples with different reaction time.

4.1.3. Reaction mechanism of CIGSe

In order to study the growth mechanism, CIGSe samples were synthesized at different reaction steps such as 1st step (140°C for 1h), 2nd step (210°C for 1h) and 3rd step (260°C for 4h). XRD patterns of samples synthesized at different reaction steps are shown in Fig. 4.11(a). In the first step (140ºC), all the observed peaks were well indexed with the orthorhombic crystal structure of β-CuSe (JCPDS 27-0184) [16]. During the second step (210ºC), a mixed phase formation of CIGSe and β-CuSe were observed. A broad peak at about 27^o splitted into two constituents as 26.9 and 27.9^o which attributed to (112) plane of CIGSe and β-CuSe respectively. Also, (312) plane of CIGSe was observed at 53.1^o. In the third step (260ºC), the splitted broad peak appeared as a single narrow peak which is well indexed with (112) plane of CIGSe. Consequently, β-CuSe peaks vanished completely and formation of the single phase chalcopyrite crystal structure of CIGSe was confirmed by the presence of (112), (220) and (312) planes **(JCPDS 35-1102) [17]**. The sharp and well-defined peaks revealed the high crystalline quality of CIGSe. According to XRD results, the sequences of phase transformations of this process are β-CuSe, mixture of β-CuSe as well as CIGSe and CIGSe. Hence, the XRD results confirm that β-CuSe acts as a preliminary product to form a single phase CIGSe.

Raman spectra of the samples obtained at different reaction steps are shown in **Fig. 4.11(b)**. In the first step (140°C), a peak observed at 258.49 cm^{-1} is ascribed to A_1 mode of β-CuSe **[3–5]**. During the second step (210°C), two peaks at around 174.28 and 258.32 cm^{-1} were observed which correspond to A_1 mode of CIGSe and CuSe respectively **[1,3–5]**. Hence, the results further proves the mixed phase formation. In the third step (260°C), the β-CuSe peak was expelled and formation of single phase CIGSe was confirmed due to the presence of A_1 mode peak at 174.68 cm^{-1} **[1]**. A_1 mode represents the vibration of Se anions in the x-y plane regardless of static neighboring cations (Cu, In and Ga). The obtained Raman results are in good accordance with the XRD results as discussed earlier **Fig. 4.11(a)**.

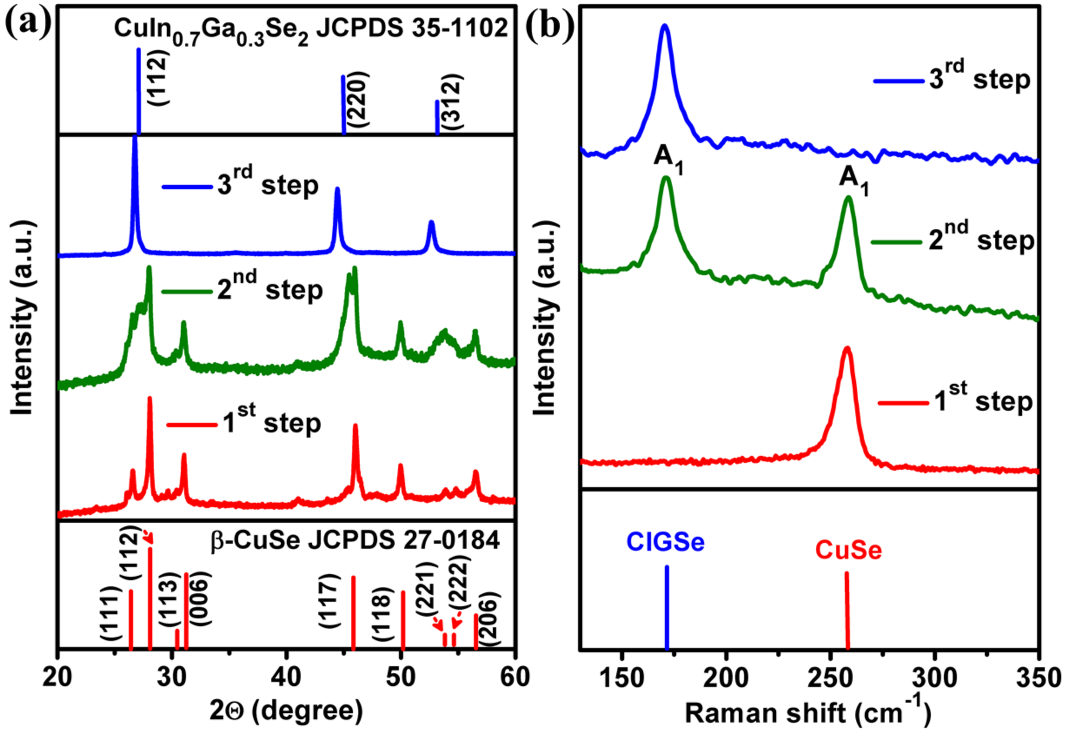

Fig. 4.11. CIGSe samples synthesized at different reaction steps (a) XRD pattern, (b) Raman spectra.

FE-SEM micrographs of CIGSe samples synthesized at different reaction step is shown in Fig. 4.12. As the reaction steps increases, the shape of the particles were changed from quasi hexagonal to proper hexagonal. Besides, particle sizes were increased from 0.12 to 1.2 µm due to Ostwald ripening [14,15]. EDS composition of CIGSe samples synthesized at different reaction step are shown in Fig. 4.13. The sample synthesized at 140°C showed the absence of In and Ga content which is due to the formation of CuSe phase at this temperature as we observed from the structural analysis (Fig. 4.11). When the reaction temperature was 210°C, Cu-rich composition was obtained. As reaction temperature increased to 260°C, the composition of CIGSe is very close to the targeted value.

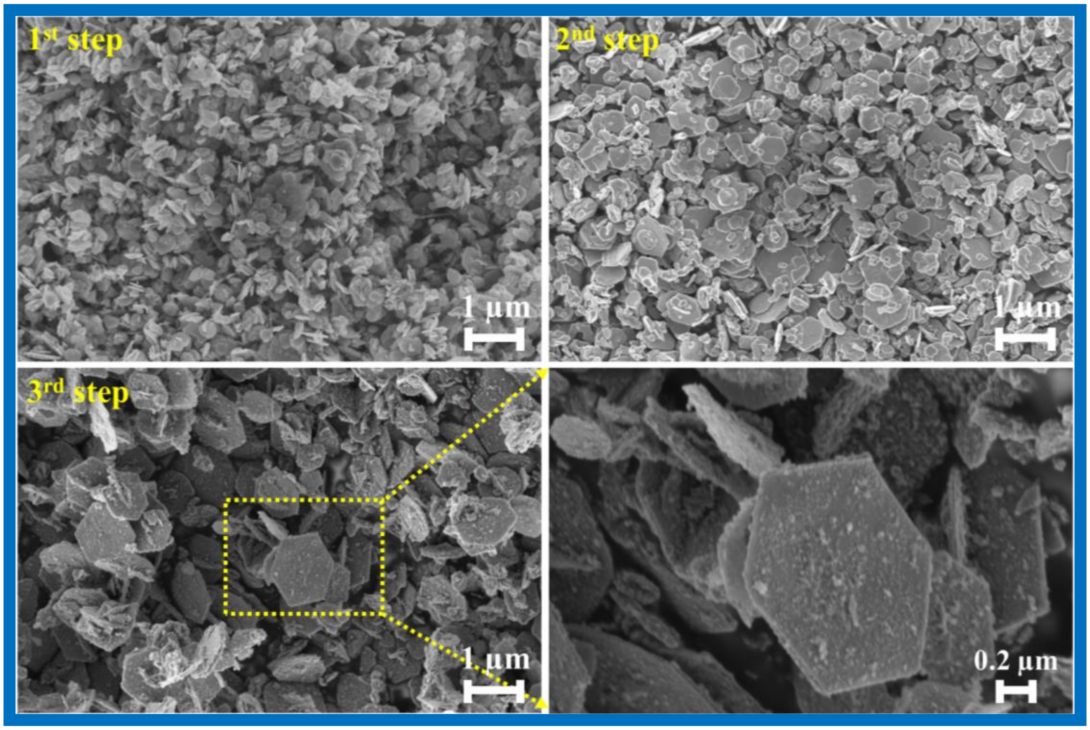

Fig. 4.12. FE-SEM micrographs of CIGSe samples synthesized at different reaction step.

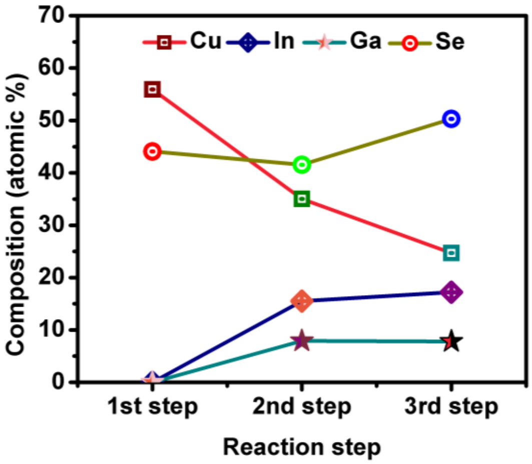

Fig. 4.13. EDS composition of FE-SEM micrographs of CIGSe samples synthesized at different reaction step.

Table 4.1 shows the composition, d-spacing value and its corresponding plane for different reaction steps. TEM image **(Fig. 4.14a)** shows quasi hexagonal flake of 0.2 µm size in the first step (140ºC). STEM-EDS line scan analysis **(Fig. 4.14b)** shows the 1.12:0.88 ratio of Cu and Se **(Table 4.1)**. From the HR-TEM image and FFT **(Fig. 4.14c & d)**, d-spacing values 0.31, 0.28 and 0.20 nm were obtained which are consistent with the (112), (006) and (117) crystal lattice planes of β-CuSe. During the second step (210ºC), TEM image **(Fig. 4.14e)** shows elongation of the hexagonal flakes with the size ranging from 0.2 to 0.5 µm. STEM-EDS line scan analysis **(Fig. 4.14f)** shows the composition of Cu and Se (1.02:0.98), while **Fig. 4.14i** shows the composition of Cu:In:Ga:Se (0.99:0.72:0.28:2.01). The d-spacing values, 0.31, 0.18 and 0.33 nm were calculated from the **Fig. 4.14g,h,j&k**, which correspond to (112) and (118) crystalline planes of β-CuSe and (112) plane of CIGSe respectively (**Table 1**). In the third step (260ºC), TEM image **(Fig. 4.14l)** depicts the proper hexagonal flake with the size of ~ 0.7 µm. STEM-EDS line scan analysis **(Fig. 4.14m)** shows the material composition of Cu:In:Ga:Se (0.98:0.69:0.31:2.02) which is very close to the desired stoichiometry. From **Fig. 4.14n**, lattice fringes were clearly observed along the axis of the flake. From the HR-TEM image and FFT **(Fig. 4.14n&o)**, the d-spacing value of 0.33 nm was observed which ascribed to (112) plane of chalcopyrite CIGSe **[18]**. These results are consistent with the structural analysis as discussed previously **(Fig. 4.11)** which elucidates that β-CuSe (starting phase) is formed at low temperature due to the preferential reaction between Cu and Se. Furthermore, the phase transformation occurs from β-CuSe to single phase CIGSe at a higher temperature since it provides sufficient energy for the cation inter-diffusion and thus expels the starting phase of β-CuSe.

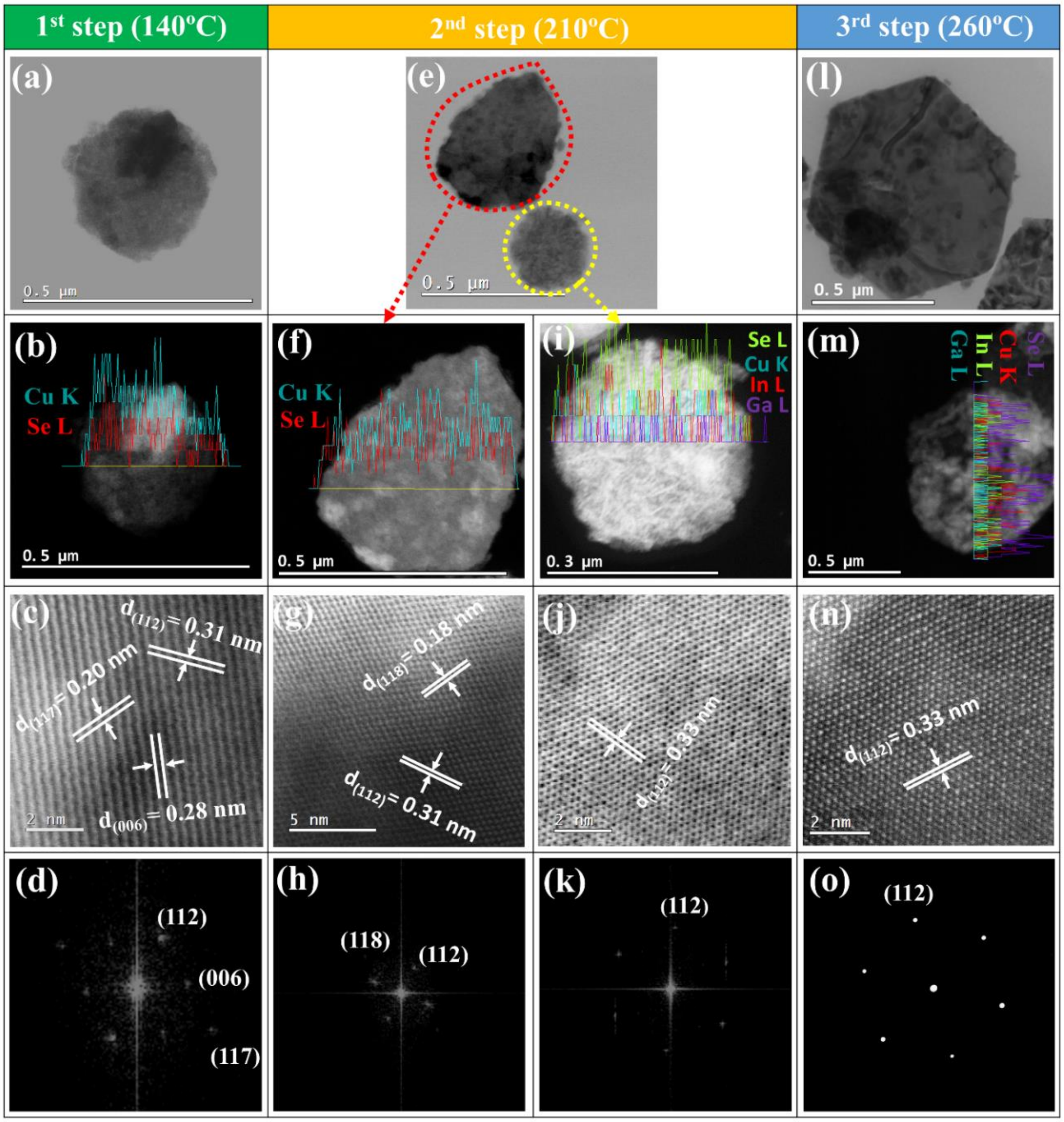

Fig. 4.14. a) & b) TEM image and STEM-EDS line scan of β-CuSe flake, c) & d) HR-TEM image and fast Fourier transform (FFT) (In the first step). e) TEM image of CIGSe and β-CuSe flake, f), g) & h) STEM-EDS, HR-TEM, and FFT of β-CuSe flake. i), j) & k) STEM-EDS line scan, HR-TEM, and FFT of CIGSe flake (During the second step). l) & m) TEM image and STEM-EDS line scan of CIGSe flake, n) & o) HR-TEM image and FFT of CIGSe flake (In the third step).

Table 4.1. STEM-EDS line scan and HR-TEM results of samples synthesized at different reaction steps.

Steps	Phase formation		Composition of Cu/In/Ga/Se in atomic ratio %	d- spacing value of HR-TEM (nm)	Planes
1st	β-CuSe		55.93:0:0:44.07 (1.12:0:0:0.88)	0.31 0.28 0.20	(112) (006) (117)
2nd	Mixed phase of β-CuSe and CIGSe	β-CuSe	51.2:0:0:48.8 (1.02:0:0:0.98)	0.31 0.18	(112) (118)
		CIGSe	25.12:17.9:7.1:49.88 (0.99:0.72:0.28:2.01)	0.33	(112)
3rd	CIGSe		24.7:17.2:7.8:50.3 (0.98:0.69:0.31:2.02)	0.33	(112)

The UV-VIS-NIR absorption spectra of CIGSe samples synthesized at different reaction step is shown in Fig. 4.15. With increases in the reaction steps, there is a redshift towards higher wavelength **(Fig. 4.15a)** and the band gaps were calculated by extrapolating the straight line plot of hν versus $(\alpha h\nu)^2$ **(Fig. 4.15b)**. The calculated band gap values were 1.0, 1.15 and 1.25 eV for 1st, 2nd, and 3rd reaction steps respectively. The sample synthesized in the 1st step showed a band gap value of 1 eV for CuSe [7,8]. The band gap values were increased with increases in the reaction steps due to the incorporation of Ga and In ions into CuSe crystal lattice. These results are in good accordance with the structural and compositional analysis.

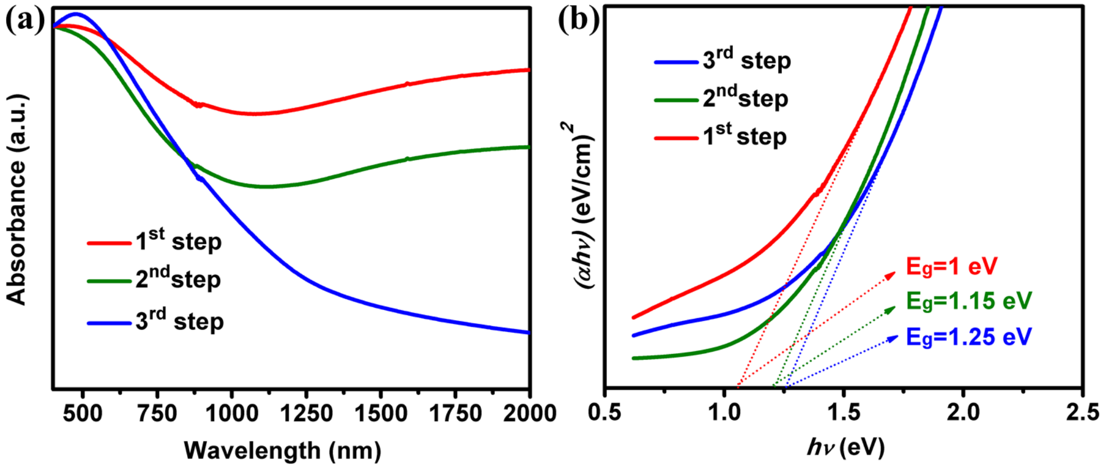

Fig. 4.15. CIGSe samples synthesized at different reaction step (a) UV-VIS-NIR absorption spectra and (b) Band gap spectra.

On the basis of above results, we proposed a plausible growth mechanism of CIGSe sub-micron hexagonal flakes by three step heating-up process which is illustrated in **Fig. 4.16**.

[1]In the first step (140ºC), OLA-copper complexes get decomposed and then monomers containing Cu^+ ions get released, which reacts with Se_x^{2-} ions that result from the dissolution and reduction of Se by OLA, thus forming an orthorhombic crystal structure of β-CuSe which is evident from the structural analysis **(Fig. 4.11)**. According to hard–soft acid–base model **[19]**, the soft base of Se reacts with a soft acid of Cu^+, instead of hard acids such as Ga^{3+} and In^{3+}, forming initially crystalline nuclei which are then followed by the oriented growth of seeds to form β-CuSe at low temperature. OLA not only acts as an efficient stabilizing ligand but also acts like a template-guide for the preferential growth of quasi hexagonal orientation of β-CuSe. The hexagonal flake-like shape of β-CuSe is consistent with the literature **[16]**.

[2]OLA-In and OLA-Ga complexes are more stable at a lower temperature, but as the temperature rises to 210ºC, both Ga^{3+} and In^{3+} ions are set free. There is inward diffusion of both these ions into the as-formed β-CuSe and a partial outward diffusion of Cu^+ which leads to the formation of CIGSe **[20]**. Cu (I) ions in the

CuSe form have high mobility which can facilitate an exchange with other cations (Ga^{3+} and In^{3+}) at relatively higher reaction temperature. The conversion of β-CuSe to CIGSe is a consequence of lattice distortion which can be accomplished by a low energy barrier. The uncontrolled outward diffusion of Cu^{+} and a limited supply of Ga^{3+} and In^{3+} leads to prolonged growth stage causing elongation of β-CuSe **(Fig. 4.14f)**. Moreover, in a few particles the intercalation of cations into CuSe is so enormous that there is the transformation of the geometry from quasi hexagonal to elongated structures to irregular to proper hexagonal ones, which is confirmed from the **Fig. 4.14i.** Hence, the observed mixed phase of β-CuSe and CIGSe is the resultant of incomplete reaction taking place at this temperature, which can also be deduced from the structural analysis **(Fig. 4.11)**.

[3]In the third step (260°C), Ga^{3+} and In^{3+} have released abundantly from OLA complexes, which rearrange themselves in a regulated fashion, to form a hexagonal flake. This chemical transformation occurs from β-CuSe to single phase CIGSe suggests that the higher reaction temperature provides more energy for cation interdiffusion and thus expels the starting phase of β-CuSe. A single phase of CIGSe formation is confirmed by structural analysis **(Fig. 4.11)**. **Fig. 4.14l** shows the proper hexagonal flake-like shape of CIGSe (~0.7 µm) which possess high surface anisotropy. The phase-field model of crystal morphology states that the grain growth of seeds with such high anisotropy in general proceeds to a hexagonal morphology **[21]**. The hexagonal morphology was found in many groups of different materials such as Ag, Au, Cu and TiO_2 **[22–24]**. In the present case, the obtained hexagonal flakes might be due to the presence of a pair of twin planes in a 6 number fold symmetry. It is worth to mention that CIGSe possesses only primitive tetragonal unit system and has no hexagonal symmetry axis. Therefore, hexagonal structures could not be achieved without multiple twinning of the primitive axis, which occurs only under special conditions **[24]**. Hence, our synthetic strategy for this novel CIGSe sub-micron flakes will stand out among other synthesis methods.

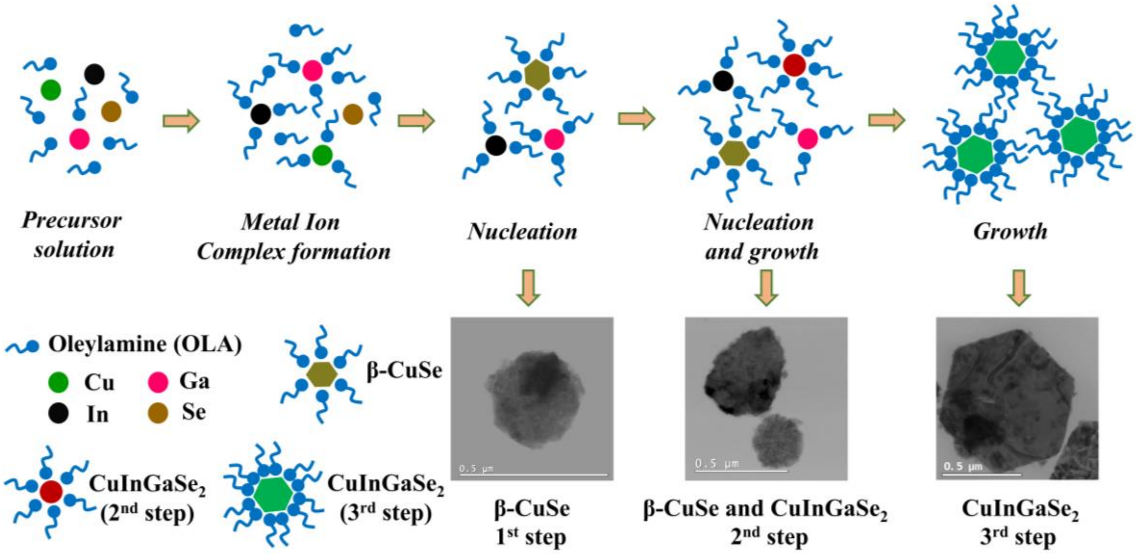

Fig. 4.16. Evolution pathway of CIGSe sub-micron hexagonal flakes synthesized via three step heating-up process.

4.1.4. Large-scale synthesis of CIGSe

We used a facile one-pot heating-up process for the large-scale synthesis of CIGSe hexagonal flakes. In order to test the scalable process, we increased the synthesis volume to 10-fold increases compared to the small scale synthesis as discussed in the previous section. **Fig. 4.17** summarize the results for gram-scale production prepared using Cu:In:Ga:Se precursor ratio of 1:0.7:0.3:2 in 100 mL OLA under a nitrogen atmosphere at 260°C for 4h. XRD spectrum **(Fig. 4.17a)**, Raman spectrum **(Fig. 4.17b)**, HR-TEM image **(Fig. 4.17f)** and SAED pattern **(Fig. 4.17g)** and confirmed that the synthesized sample has chalcopyrite crystal structure of single phase CIGSe. The band gap energy **(Fig. 4.17d)** was determined on the basis of absorbance spectrum **(Fig. 4.17c)** by extra plotting hν versus $(\alpha h\nu)^2$ was 1.25 eV which is in good agreement with the band gap of small scale synthesized CIGSe. The morphology of synthesized CIGSe is the hexagonal flake-like shape **(Fig. 4.17e&i)** with the size ranging from 0.7 to 1 μm as can be seen in FE-SEM micrograph **(Fig. 4.17i)**. As can be seen in **Fig (4.17k-n),** EDS elemental mapping of hexagonal flakes confirmed that Cu, In, Ga, and Se were homogenously distributed **[20]**. **Fig. 4.17h** shows that the EDS composition of Cu:In:Ga:Se were

1:01:0.71:0.29:1.99 which is very close to the targeted value. As a result, one-pot heating-up approach is possible to produce CIGSe in gram-scale (2 gram) with excellent control over crystal phase, morphology, particle size, bandgap energy, and composition.

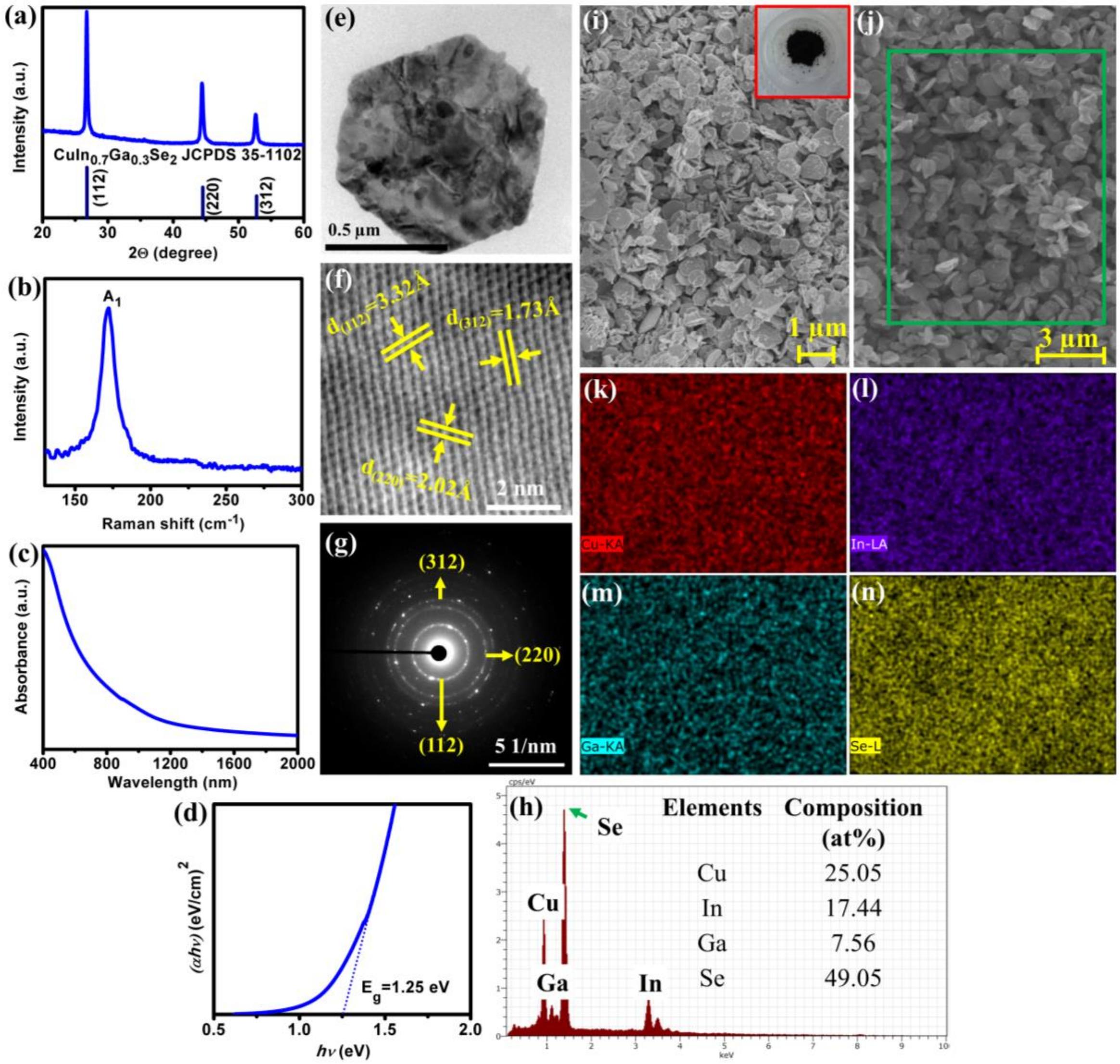

Elements	Composition (at%)
Cu	25.05
In	17.44
Ga	7.56
Se	49.05

Fig. 4.17. Large-scale synthesis of CIGSe at 260°C for 4h (a) XRD spectrum, (b) Raman spectrum, (c) UV-VIS-NIR absorption spectrum, (d) Bandgap spectrum, (e) TEM micrograph, (f) HR-TEM image, (g) SAED pattern, (h) EDS spectrum, (i) FESEM micrograph, (j) FESEM micrograph (green rectangular area is the selected area for mapping) and (k-n) EDS mapping.

4.2.Influence of copper (Cu) concentrations

In this section, we studied the effect of Cu concentration on the structural, morphological, compositional and optical properties of CIGSe powder. Because in high-efficiency solar cells, the CIGSe absorber material has grown slightly Cu-poor condition [Cu/(In+Ga) =0.88 to 0.92]. It is worth to mention that the CIGSe absorber material can be fabricated within a large range of Cu contents. The Cu content has a strong influence on the properties of CIGSe absorber which would affect the solar cell performance. For instance, at low Cu content [Cu/(In+Ga)<0.7], the conductivity of CIGSe film is very low which suppress the shunt paths in such a way that enhances the solar cell performance at low irradiance conditions (Irradiance $E<100\ W/m^2$) **[25]**. Here, the question is how the CIGSe will compensate the Cu vacancies without losing their electronic properties is of great interest. A plausible explanation is that the formation of Ordered Vacancy Compounds (OVC) at low Cu content, which is electronically inactive **[26]** and has a higher bandgap value than stoichiometry CIGSe **[27]**. The CIGSe solar cell prepared at Cu-rich [Cu/(In+Ga)>1] condition showed poor performance due to the formation of highly conductive binary phases such as CuSe, $CuSe_2$, and $Cu_{2-x}Se$ which produces the shunt paths. Investigation of CIGSe absorber material properties with various Cu content is of great interest but only a few reports exist in the literature (only by vacuum method) **[3,28]**. So far, there is still no report for CIGSe absorber with different Cu concentration by solution based approach. So, it's interested to study the effect of Cu concentrations on CIGSe properties by solution based approach.

4.2.1. Results and discussion

$Cu(In_{0.7}Ga_{0.3})Se_2$ powders were synthesized by varying copper concentration via a facile one-pot heating-up process. Cu concentration in the solution was varied such as 0.4, 0.6, 0.8, 1.0 and 1.2 mmol to study their influences on the structural, morphological, compositional, optical properties of CIGSe powder.

XRD patterns of CIGSe samples synthesized at different Cu concentration are shown in **Fig. 4.18a**. For all the samples, (112), (220) and (312) planes were observed which correspond to chalcopyrite crystal structure of CIGSe [JCPDS 35-1102]. Additionally, the sample synthesized with Cu=1.2 showed the (102) plane of CuSe phase at 2ϴ value of 35.58^0 [JCPDS 20-1020]. As the Cu concentration increases, the intensity of CIGSe peaks was increased which indicates an increment in the crystalline and grain size **[28]**. The calculated FWHM for (112) plane decreased from 1.3526 to 0.356^0 with increases in the Cu concentration as shown in **Fig. 4.19**.

Raman spectra of CIGSe samples synthesized at different Cu concentration are shown in **Fig. 4.18b**. All the samples exhibited a prominent peak at around 175.81 cm^{-1} matches to A_1 optical phonon mode of CIGSe. This mode represents the vibration of Se atoms in the x-y plane with cations of Cu, In and Ga is being at rest **[1]**. As the Cu concentration increases, the A_1 mode peaks were getting narrower which reveals the decrement in the defects. With increases in the Cu concentration, the A_1 mode peak was shifted towards lower wavenumber which can be explained by bond-stretching central force constant α calculated by Kumar et al **[29]**. The $\alpha_{III–Se}$ for the group III–Se bonds is larger than $\alpha_{Cu–Se}$ for the Cu–Se bonds. When the Cu<1, III-Se bonds are more and contribution of III-Se bonds are stronger than $\alpha_{Cu–Se}$ **[30]** resulting the A_1 mode peak shifted to higher wavenumber. In addition, mixed B_2/E modes **[2]** of CIGSe at around 228 cm^{-1} was observed. The B_2/E modes represent the vibrations of anions and cations together. Cu-poor samples (Cu<1) showed a broad peak at 155 cm^{-1}, indicates the presence of $Cu_2(In,Ga)_4Se_7$ phase of OVC **[3]** which was not detected by XRD. When the Cu>1, CuSe peak was observed at around 260 cm^{-1} **[3]**. Raman results were in good accordance with the XRD results.

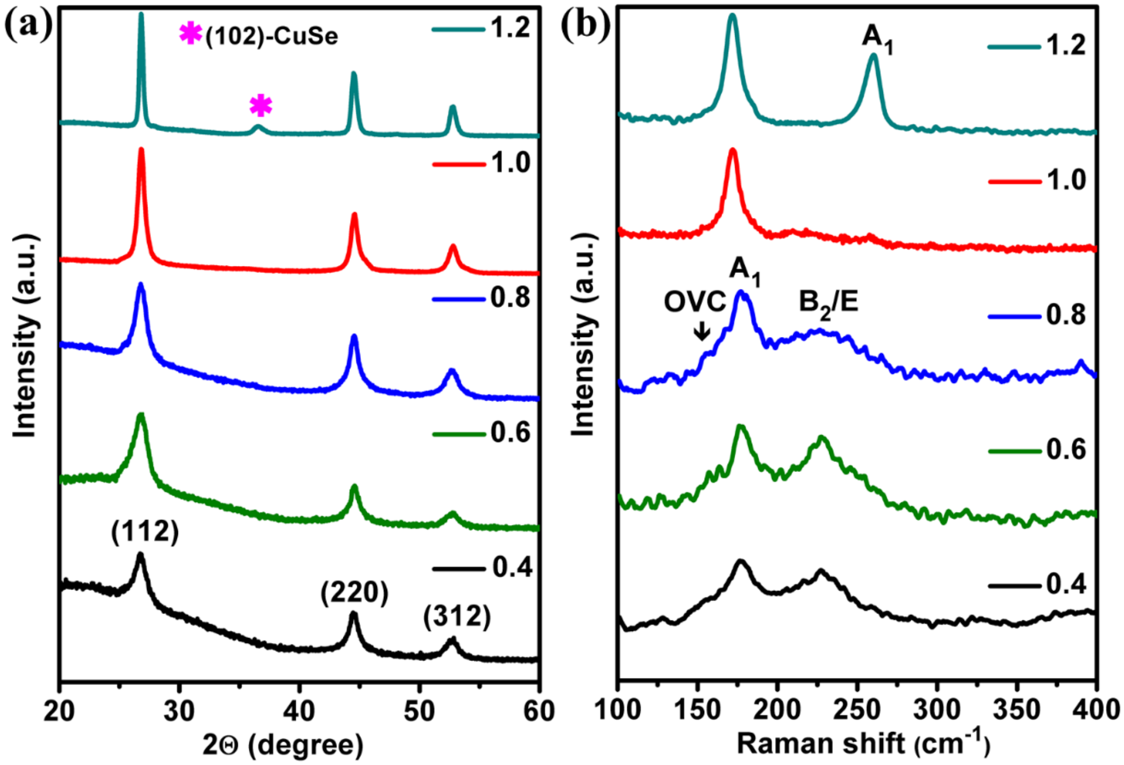

Fig. 4.18. (a) XRD patterns and (b) Raman spectra of synthesized CIGSe samples with different Cu concentration.

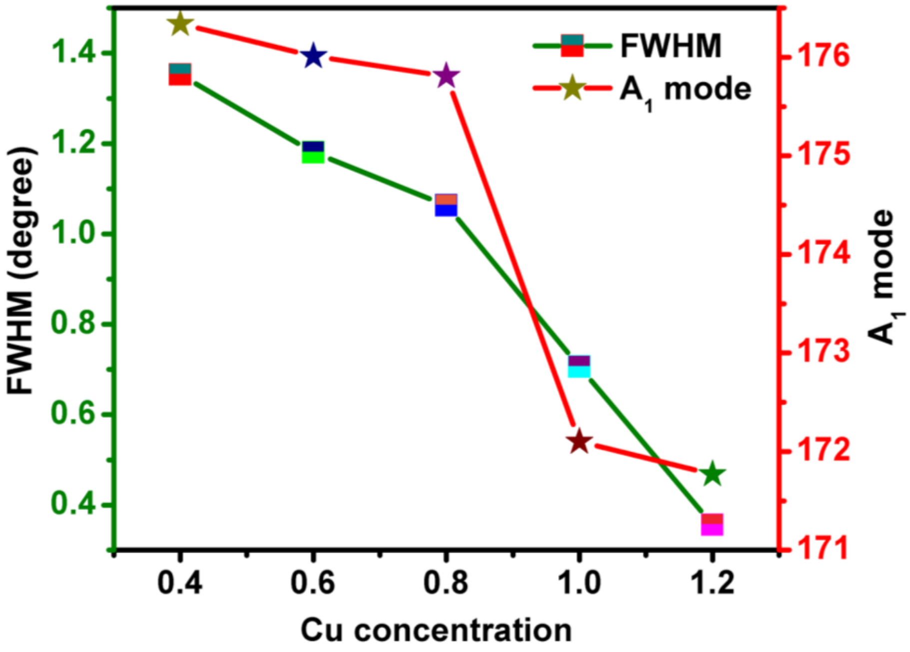

Fig. 4.19. Changes in FWHM and Raman A$_1$ mode as a function of Cu concentration.

FE-SEM and TEM micrographs of synthesized CIGSe samples with different Cu concentration are shown in **Fig. 4.20**. The particle sizes increased from 25 nm to 1 µm with increases in the Cu concentration **[3]**. When the Cu concentration is 0.4, irregular shape of the particles observed with size ranging from 15 to 30 nm as shown in **Fig. 4.20a & f.** As the Cu concentration increased to 0.6, the particles size increased from 25 to 60 nm which can be seen in **Fig. 4.20b & g**. For Cu=0.8, hexagonal flake-like particles were observed with size varies from 500 to 700 nm as shown in **Fig. 4.20c & h**. When the Cu>0.8, hexagonal flake-like particles were seen with size ranging from 900 nm to 1 µm **(Fig. 4.20i & j)**. In addition to that, seed-like particles with a size of 50 nm were observed on the surface of hexagonal flakes as can be seen in **Fig. 4.20d & e**. When the Cu>0.6, the thickness of hexagonal flake increased from 52 to 84 nm. The large sized hexagonal flakes were observed by varying the Cu concentration which has not yet reported. The obtained large sized crystals could reduce the defects and enhance the photo-conversion efficiency of the solar cell.

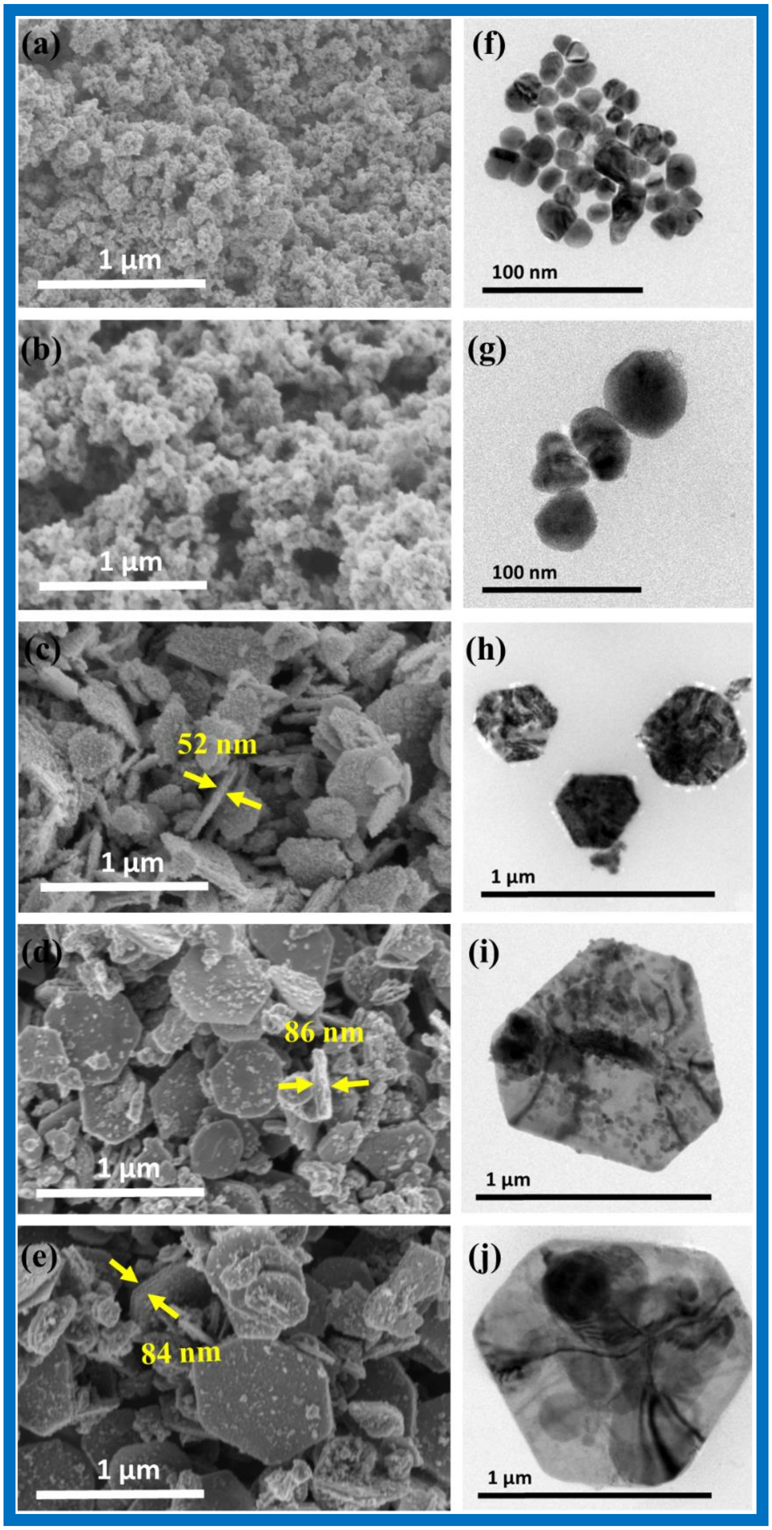

Fig. 4.20. FE-SEM and TEM micrographs of synthesized CIGSe samples with different Cu concentration where (a), (f) Cu=0.4, (b), (g) Cu=0.6, (c), (h) Cu=0.8, (d), (i) Cu=1 and (e), (j) Cu=1.2.

The elemental composition of synthesized CIGSe samples with different Cu concentration is shown in Fig. 4.21a. As the Cu concentration increases, Cu/(In+Ga) and Ga/(In+Ga) ratio were increased as depicted in Fig. 4.21b. The Ga/(In+Ga) ratio increased with increasing Cu concentration which could be due to more CuSe seed formation in the initial stage. We studied the formation mechanism of CIGSe via CuSe seed in our previous work as discussed earlier [7]. So, we believe that the CuSe seeds formation was more with increases in the Cu concentration which readily exchanges the more cation of Ga ions. When Cu>1, the Se content was less (Fig. 4.21a) and an excess Cu leads to the formation of CuSe phase as we observed in the structural analysis (Fig. 4.18b). When Cu<1, In-rich and Cu-poor composition was observed which leads to the formation of OVC as confirmed from Raman analysis. The same behavior was observed by other researchers [3].

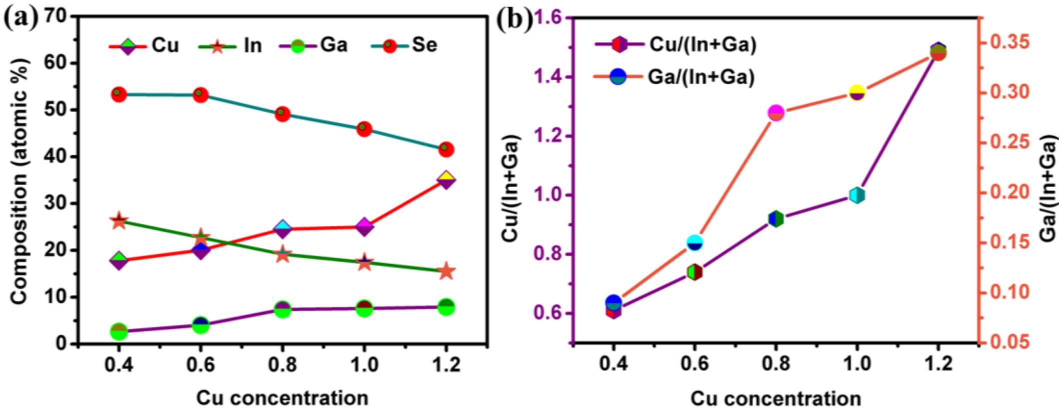

Fig. 4.21 (a) EDS composition of synthesized CIGSe samples with different Cu concentration and (b) the corresponding Cu/(In+Ga) and Ga/(In+Ga) ratio.

The UV-VIS-NIR absorption spectra of synthesized CIGSe samples at different Cu concentration are shown in Fig. 4.22a. The absorption started in near infrared region and it gradually increased to the ultraviolet-visible region. As the Cu content concentration increases, the absorption edge shifts towards higher wavelength [27]. As can be seen in Fig. 4.22b, the calculated band gap of the particles were 1.98, 1.68, 1.37, 1.18 and 0.84 eV for Cu=0.4, 0.6, 0.8, 1.0 and 1.2 respectively. From the Fig. 4.22b, we could observe that the band gap was increased when the samples were Cu-poor (Cu<1) and it is consistent with the reduced density of states near the VBM due to Cu deficiency. In CIGSe, the upper valence band is composed of Cu *3d* and Se *4p* states, changes in the Cu concentration affects the electronic structure. Cu-poor samples (Cu<1) showed increment in the band gap energy due to weaker p-d interaction in the Cu-deficient material which turns the VBM to lower energy position [31]. The stoichiometry (Cu=1) sample exhibited the band gap of 1.18 eV which is in good agreement with the literature [32]. Decrement in the band gap was observed at Cu=1.2, which is due to Cu *3d* and Se *4p* states repel each other which moves the VBM towards higher energy [33].

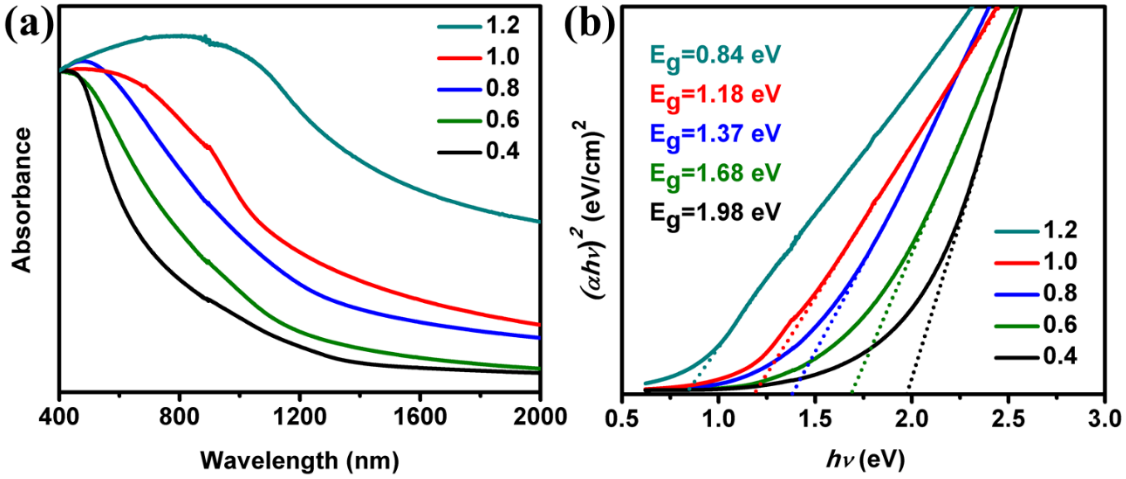

Fig. 4.22. (a) UV-VIS-NIR absorption spectra of synthesized CIGSe samples with different Cu concentration and (b) the corresponding plot of $(\alpha h\nu)^2$ versus ($h\nu$).

4.3.Summary

- ✓ CIGSe submicron particles were synthesized using a facile and economical one-pot process by heating a mixture of metal chlorides and elemental selenium in presence of oleylamine. The effect of reaction parameters such as reaction temperature, reaction time on the formation of phase pure chalcopyrite CIGSe submicron particles with controlled stoichiometry composition were investigated. The formation mechanism of quaternary CIGSe was investigated. Furthermore, we tested the suitability of our strategy for large-scale production by carrying out of gram-scale synthesis.

- ✓ Firstly, CIGSe submicron particles were synthesized by varying the reaction temperatures such as 240, 260, 280 and 300^{0}C by keeping constant reaction time of 4h. It is found that reaction temperature of 260^{0}C is required to form pure phase CIGSe with stoichiometric composition. With increases in the reaction temperature, peak shift was observed from the XRD (towards lower 2Θ angle) and Raman (towards lower wavenumber) which is due to decrement in the Ga content. Lattice constants ***a*** and ***c*** were increased linearly as the reaction time increases. The increases in the lattice parameters is due to substitution of the bigger ionic size of In (0.62 Å) for smaller ionic size of Ga (0.47 Å) which enlarges the unit volume. When the reaction temperature was less than 260^{0}C, Cu-rich composition was obtained which could be due to the high reactivity of Cu. Further increasing the reaction temperature, Ga-poor composition was obtained due to the evaporation of Ga. Therefore, the sample prepared at 260^{0}C showed proper composition which is very close to the targeted value. As the reaction temperature increases, the redshift was observed from the UV-VIS-NIR absorbance spectra and band gap energy decreased from 1.38 to 1.02 eV which is due to decrement in the Ga content. As the reaction temperature increases, particles sizes were decreased from 1.3 to 0.4 μm and this could be due to increases in the nucleation rate which leads to the smaller particles. The changes in the morphology from hexagonal flake to prism could possibly due to variation in the composition.

- ✓ Reaction time is the next parameter to be taken for investigation. For this, CIGSe submicron particles was synthesized at 260^{0}C by varying the reaction time such as 1, 2, 4 and 6h. It is found that the reaction time of 4h is required to get CIGSe with targeted composition. As the reaction time increases, the peak shift has been observed in the XRD (towards higher 2Θ angle) and Raman (towards higher wavenumber) which is due to increment in the Ga content. As the reaction time prolonged to 4h, the lattice constants ***a*** and ***c*** were decreased linearly which is in good agreement with Vegard’s law. The decreases in the lattice constants is due to substitution of the smaller ionic radius of Ga (0.47 Å) for the bigger ionic radius of In (0.62 Å) which leads to shrinkages in the unit volume. EDS analysis showed an increment in the Ga/(In+Ga) ratio as the reaction time increases. The blue shift was observed from the UV-VIS-NIR absorbance spectra and band gap energy increased from 1.01 to 1.29 eV which is due to increment in the Ga content. With increases in the reaction time, the particle size increased from 50 nm to 1.2 µm due to Ostwald ripening.

- ✓ To study the growth mechanism, CIGSe was synthesized at different reaction steps such as 1st step (140°C for 1h), 2nd step (210°C for 1h) and 3rd step (260°C for 4h). Reaction pathway was evaluated for pure phase CIGSe, which is initiated from binary β-CuSe and then subsequently transferred to CIGSe by gradual incorporation of In^{3+} and Ga^{3+} ions into the β-CuSe crystal lattice. Structural results confirmed the sequences of phase transformations of this process are β-CuSe, mixture of β-CuSe as well as CIGSe and CIGSe. Morphology of the particles changed from quasi hexagonal to proper hexagonal shape. The band gap energy increased from 1 to 1.25 eV which is due to the incorporation of more Ga and In ions into CuSe crystal lattice.

- ✓ Later, large-scale synthesis was performed using the small scale procedure by increasing the amount of precursors to 10-fold. CIGSe powder was synthesised in gram-scale (2 gram) while maintaining control over the phase, composition, bandgap energy, particle size, and morphology. Consequently, these results demonstrated the one-pot heating-up process is more suitable for large scale synthesis of CIGSe powder.

- ✓ $Cu(In_{0.7}Ga_{0.3})Se_2$ powders were synthesized by varying Cu concentration using a facile one-pot heating-up process for the first time. Cu concentration in the solution was varied such as 0.4, 0.6, 0.8, 1.0 and 1.2 mmol to study their influences on the structural, morphological, compositional and optical properties of CIGSe powder. Structural analysis showed the formation of OVC compound (Cu<1) and CuSe (Cu>1) along with chalcopyrite CIGSe phase. With increases in the Cu concentration, the morphology of the particles changed from irregular to hexagonal flake-like shape and particle sizes were increased from 15 nm to 1 µm. EDS analysis showed an increment in the Ga/(In+Ga) ratio with increasing Cu concentration. The absorption band edge was shifted to higher wavenumber and optical band gap energy decreased from 1.98 to 0.84 eV as the Cu concentration increases. These results suggested that the Cu concentration plays a vital role in the phase formation, morphology, particles size, band gap energy of solution processed CIGSe particles.

References

[1] A.Chirilă, S.Seyrling, S.Buecheler, D.Guettler, S.Nishiwaki, Y. E. Romanyuk, G.Bilger and A.N. Tiwari, Influence of high growth rates on evaporated Cu(In,Ga)Se_2 layers and solar cells, Prog. Photovolt: Res. Appl. 20 (2012) 209‑216. doi: 10.1002/pip.1122.

[2] J. Liu, D. Zhuang, M. Cao, C. Wang, M. Xie, X. Li, Preparation and Characterization of Cu(In,Ga)Se_2 Thin Films by Selenization of $Cu_{0.8}Ga_{0.2}$ and In_2Se_3 Precursor Films, 2012 (2012). doi:10.1155/2012/149210.

[3] W. Witte, R. Kniese, M. Powalla, Raman investigations of Cu(In,Ga)Se_2 thin films with various copper contents, Thin Solid Films. 517 (2008) 867–869. doi:10.1016/j.tsf.2008.07.011.

[4] O. Arellano-Tánori, M.C. Acosta-Enríquez, R. Ochoa-Landín, R. Iñiguez-Palomares, T. Mendívil-Reynoso, M. Flores-Acosta, S.J. Castillo, Copper-selenide and copper-telluride composites powders sintetized by ionic exchange, Chalcogenide Lett. 11 (2014) 13–19.

[5] V. Izquierdo-Roca, X. Fontané, E. Saucedo, J.S. Jaime-Ferrer, J. Álvarez-García, A. Pérez-Rodríguez, V. Bermudez, J.R. Morante, Process monitoring of chalcopyrite photovoltaic technologies by Raman spectroscopy: an application to low cost electrodeposition based processes, New J. Chem. 35 (2011) 453. doi:10.1039/c0nj00794c.

[6] A. Ben Marai, J. Ben Belgacem, Z. Ben Ayadi, K. Djessas, S. Alaya, Structural and optical properties of $CuIn_{1-x}Ga_xSe_2$ nanoparticles synthesized by solvothermal route, J. Alloys Compd. 658 (2016) 961–966. doi:10.1016/j.jallcom.2015.10.287.

[7] M. Latha, R.A. Devi, S. Velumani, G. Oza, P. Reyes-Figueroa, M. Rohini, I.G. Becerril-Juarez, J. Yi, Synthesis of $CuIn_{1-x}Ga_xSe_2$ Nanoparticles by Thermal Decomposition Method with Tunable Ga Content, J. Nanosci. Nanotechnol. 15 (2015) 8388–8394. doi:10.1166/jnn.2015.11473.

[8] J. Li, Z. Jin, T. Liu, J. Wang, D. Wang, J. Lai, H. Du, L. Cui, Ternary and quaternary chalcopyrite $Cu(In_{1-x}Ga_x)Se_2$ nanocrystals: organoalkali-assisted diethylene glycol solution synthesis and band-gap tuning, CrystEngComm. 15 (2013) 7327. doi:10.1039/c3ce40813b.

[9] M. Ahmadi, S.S. Pramana, L. Xi, C. Boothroyd, Y.M. Lam, S. Mhaisalkar, Evolution pathway of CIGSe nanocrystals for solar cell applications, J. Phys. Chem. C. 116 (2012) 8202–8209. doi:10.1021/jp300187r.

[10] A. Chirilă, S. Buecheler, F. Pianezzi, P. Bloesch, C. Gretener, A.R. Uhl, C. Fella, L. Kranz, J. Perrenoud, S. Seyrling, R. Verma, S. Nishiwaki, Y.E. Romanyuk, G. Bilger, A.N. Tiwari, Highly efficient Cu(In,Ga)Se_2 solar cells grown on flexible polymer films., Nat. Mater. 10 (2011) 857–861. doi:10.1038/nmat3122.

[11] S.-I. Gu, H.-S. Shin, Y.-W. Hong, D.-H. Yeo, S. Nahm, The changes of morphology and composition in $Cu(In_{1-x}Ga_x)Se_2$ powder synthesis by solvothermal method, Met. Mater. Int. 18 (2012) 197–199. doi:10.1007/s12540-012-0026-x.

[12] K.H. Kim, Y.G. Chun, K.H. Yoon, B.O. Park, Synthesis of $CuInGaSe_2$ nanoparticles by low temperature colloidal route, J. Mech. Sci. Technol. 19 (2005) 2085–2090. doi:10.1007/BF02916502.

[13] J.D. Wu, L.T. Wang, C. Gau, Synthesis of $CuInGaSe_2$ nanoparticles by modified polyol route, Sol. Energy Mater. Sol. Cells. 98 (2012) 404–408. doi:10.1016/j.solmat.2011.11.044.

[14] S. Ahn, K. Kim, Y. Chun, K. Yoon, Nucleation and growth of Cu(In,Ga)Se_2 nanoparticles in low temperature colloidal process, Thin Solid Films. 515 (2007) 4036–4040. doi:10.1016/j.tsf.2006.10.102.

[15] W.Wang, H.Shen, X.He, Study on the synthesis and formation mechanism of Cu_2ZnSnS_4 particles by microwave irradiation, Materials Research Bulletin 48 (2013) 3140–3143. doi:10.1117/12.828365

[16] Y. Xie, X. Zheng, X. Jiang, J. Lu, L. Zhu, Sonochemical synthesis and mechanistic study of copper selenides $Cu_{2-x}Se$, beta-CuSe, and Cu_3Se_2., Inorg. Chem. 41 (2002) 387–392. doi:Doi 10.1021/Ic010108v.

[17] Z. Han, D. Zhang, Q. Chen, R. Hong, C. Tao, Y. Huang, Z. Ni, S. Zhuang, Synthesis of single phase chalcopyrite $CuIn_{1-x}Ga_xSe_2$ ($0 \leq x \leq 1$) nanoparticles by one-pot method, Mater. Res. Bull. 51 (2014) 302–308. doi:10.1016/j.materresbull.2013.12.041.

[18] S.N. Malik, S. Mahboob, N. Haider, M. a Malik, P. O'Brien, A colloidal synthesis

of $CuInSe_2$, $CuGaSe_2$ and $CuIn_{1-x}Ga_xSe_2$ nanoparticles from diisopropyldiselenophosphinatometal precursors, Nanoscale. 3 (2011) 5132–5139. doi:10.1039/c1nr10888c.

[19] R.G. Pearson, Hard and Soft Acids and Bases, Journalof Am. Chem. Soc. 85 (1963) 3533–3539. doi:10.1021/ja00905a001.

[20] E. Dilena, Y. Xie, R. Brescia, M. Prato, L. Maserati, R. Krahne, A. Paolella, G. Bertoni, M. Povia, I. Moreels, L. Manna, $CuIn_xGa_{1-x}S_2$ nanocrystals with tunable composition and band gap synthesized via a phosphine-free and scalable procedure, Chem. Mater. 25 (2013) 3180–3187. doi:10.1021/cm401563u.

[21] H. Xu, R. Matkar, T. Kyu, Phase-field modeling on morphological landscape of isotactic polystyrene single crystals, Phys. Rev. E - Stat. Nonlinear, Soft Matter Phys. 72 (2005). doi:10.1103/PhysRevE.72.011804.

[22] C. Lofton, W. Sigmund, Mechanisms controlling crystal habits of gold and silver colloids, Adv. Funct. Mater. 15 (2005) 1197–1208. doi:10.1002/adfm.200400091.

[23] P. Lignier, R. Bellabarba, R.P. Tooze, Scalable strategies for the synthesis of well-defined copper metal and oxide nanocrystals, Chem. Soc. Rev. 41 (2012) 1708. doi:10.1039/c1cs15223h.

[24] E.J. Lee, I. Nam, J. Yi, J.H. Bang, Nanoporous hexagonal TiO_2 superstructure as a multifunctional material for energy conversion and storage, J. Mater. Chem. A. 3 (2015) 3500–3510. doi:10.1039/C4TA05988C.

[25] A. Virtuani, E. Lotter, M. Powalla, U. Rau, J.H. Werner, M. Acciarri, Influence of Cu content on electronic transport and shunting behavior of $Cu(In,Ga)Se_2$ solar cells, J. Appl. Phys. 99 (2006) 1–12. doi:10.1063/1.2159548.

[26] S.B. Zhang, S.-H. Wei, A. Zunger, H. Katayama-Yoshida, Defect physics of the $CuInSe_2$ chalcopyrite semiconductor, Phys. Rev. B. 57 (1998) 9642–9656. doi:10.1103/PhysRevB.57.9642.

[27] S. Minoura, K. Kodera, T. Maekawa, K. Miyazaki, S. Niki, Dielectric function of $Cu(In,Ga)Se_2$ -based polycrystalline materials, 63505 (2013) 22–25.

[28] M.Y. Kim, G. Kim, J. Kim, J.H. Park, D. Lim, Structural and electrical properties of co-evaporated $Cu(In,Ga)Se_2$ thin films with varied Cu contents, Thin Solid Films. 546 (2013) 308–311. doi:10.1016/j.tsf.2013.05.033.

[29] V. Kumar, D. Chandra, of $A^{II}B^{IV}$ C^{V}_{2} and $A^{I}B^{III}C_{2}^{VI}$ Semiconductors, Semiconductors. 37 (1999) 37–46.

[30] C. Xue, D. Papadimitriou, N. Esser, Mapping of gradient composition $Cu_xGa_ySe_2$ film properties using Raman and PL-spectroscopy, J. Phys. D-Applied Phys. 37 (2004) 2267–2273. doi:10.1088/0022-3727/37/16/008.

[31] Sung-Ho Han, C. Persson, F.S. Hasoon, H.A. Al-Thani, A. M. Hermann, and D.H. Levi, Optical properties and electronic structures of $4(CuInSe_2)y$ $(CuIn_5Se_8)_{1-y}$, Phys. Rev. B. **74**, (2006) 085212. doi: 10.1103/PhysRevB.74.085212..

[32] J.E. Jaffe, A. Zunger, Anion displacements and the band-gap anomaly in ternary ABC_2 chalcopyrite semiconductors, Phys. Rev. B. 27 (1983) 5176–5179. doi:10.1103/PhysRevB.27.5176.

[33] J.E. Jaffe, A. Zunger, Electronic structure of the ternary chalcopyrite semiconductors $CuAlS_2$, $CuGaS_2$, $CuInS_2$, $CuAlSe_2$, $CuGaSe_2$, and $CuInSe_2$, Phys. Rev. B. 28 (1983) 5822–5847. doi:10.1103/PhysRevB.28.5822.

Chapter 5

Deposition of films using CIGSe submicron particles synthesized by one-pot heating-up process

As we discussed in **chapter 4**, the $Cu_{0.8}(In_{0.7},Ga_{0.3})Se_2$ (CIGSe) powder synthesized at 260°C for 4h showed chalcopyrite crystal structure along with particles size of ~ 500 nm. Further, we used this CIGSe powder to formulate the ink and films were deposited by–doctor blade method as mentioned in **chapter 3**. In this chapter, we study the influences of CIGSe ink concentrations and pre-annealing temperatures on the morphological properties of CIGSe films. Furthermore, we study the influences of selenization (post annealing) temperatures and sodium chloride (NaCl) treatment on the structural, morphological and compositional properties of CIGSe films. Optical, electrical and optoelectronic properties of selected CIGSe films were also investigated.

5.1.Deposition of CIGSe films

To prepare the films, formulated CIGSe ink was deposited onto soda lime glass (SLG) substrate by doctor blade method. The influences of CIGSe ink concentration, pre-annealing temperatures, selenization temperatures and NaCl treatment were discussed below.

5.1.1. Influence of CIGSe powder concentration and pre-annealing temperatures

During an ink formulation, CIGSe powder concentration was varied such as 100, 75 and 50 mg in 500 µL hexanethiol to obtain the crack-free films with a thickness of ~1-1.5 µm. The as-prepared CIGSe films were pre-annealed in ambient atmosphere to remove the organic solvent that we used during the ink formulation. The pre-annealing temperatures were chosen as 350 and 400°C for 1 min.

Fig. 5.1 shows FE-SEM micrographs of CIGSe films prepared using different CIGSe powder concentration and annealed in air at different temperature.

- **For 100 mg CIGSe powder concentration:** As-prepared film showed few segregated particles along with pin holes. The film annealed at 350°C showed cracks on the surface. As the annealing temperature increased to 400°C, cracks increased while particle segregations reduced.
- **For 75 mg CIGSe powder concentration:** As-prepared film showed smooth surface along with few segregated particles (~ 3.5 µm). Cracks were observed on the surface for the film annealed at 350°C. As the annealing temperature increased to 400°C, cracks increased while particle segregations reduced.
- **For 50 mg CIGSe powder concentration:** As-prepared film showed smooth surface with few segregated particles. Film annealed at 350°C showed very few cracks as compared to other conditions. When the temperature raised to 400°C, cracks increased and particle segregations reduced.

Subsequently, cracks were reduced as the powder concentration reduces which could be due to decrement in the thickness.

As can be seen in **Fig. 5.1** cracks were observed after annealing process for all the CIGSe powder concentration. Formation of cracks could be due to several factors as we mentioned below. The observed cracks could be due to stress generated in the film between annealing and cooling process. Stress could be introduced in the film due to thermal expansion coefficients between the film material and substrate **[1]**. The coefficients of thermal expansion (CTE) of CIGSe and SLG substrate are $(8\text{-}11)\text{x}10^{-6}$ K^{-1} and $9\text{x}10^{-6}$ K^{-1}, respectively **[2]**. The cracks were increased as the annealing temperature increases for all the CIGSe powder concentration **[3–5]**. This might be due to changes in the CTE of CIGSe and SLG substrate. As can be seen in **Fig. 5.2,** cracks were reduced as the film thickness reduces. This behaviour could be due to decrement in the CTE value as a function of film thickness **[6–8]**.

The observed cracks from annealed film could be also due to the shrinkage of CIGSe. When the film annealed at 350 and 400°C, the sulfur and carbon contents were decreased as can be seen in **Fig. 5.3**. The evaporation of the solvent (sulfur) and carbon resulting volume shrinkage in the film. This volume reduction leads to stress which induced cracks during film annealing [9,10]. Finally, the film prepared using 50 mg CIGSe powder and annealed at 350°C showed a smooth surface with very few cracks as compared to other conditions.

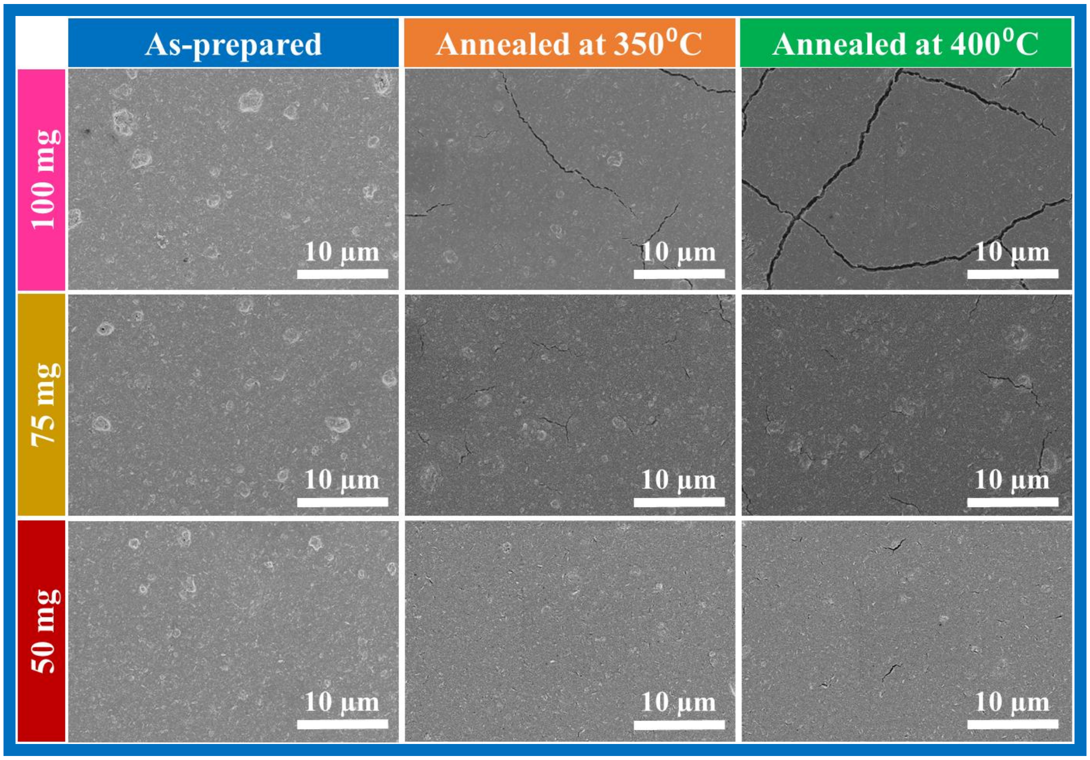

Fig. 5.1. FE-SEM images of CIGSe film for different CIGSe powder concentration and annealing temperature.

Fig. 5.2 shows the thickness of CIGSe films prepared at different CIGSe powder concentration as well as annealed at different temperature. The as-prepared film showed the thickness of 2.60, 2.10 and 1.45 µm for 100, 75 and 50 mg CIGSe powder concentration respectively. The film annealed at 350°C showed the thickness of 2.52, 2 and 1.32 µm for 100, 75 and 50 mg CIGSe powder concentration respectively. The film annealed at 400°C showed the thickness of 2.45, 1.95 and 1.28 µm for 100, 75 and 50 mg CIGSe powder concentration respectively. After annealing, film thickness was reduced as compared to as-prepared film which is due to the evaporation of sulfur and carbon content.

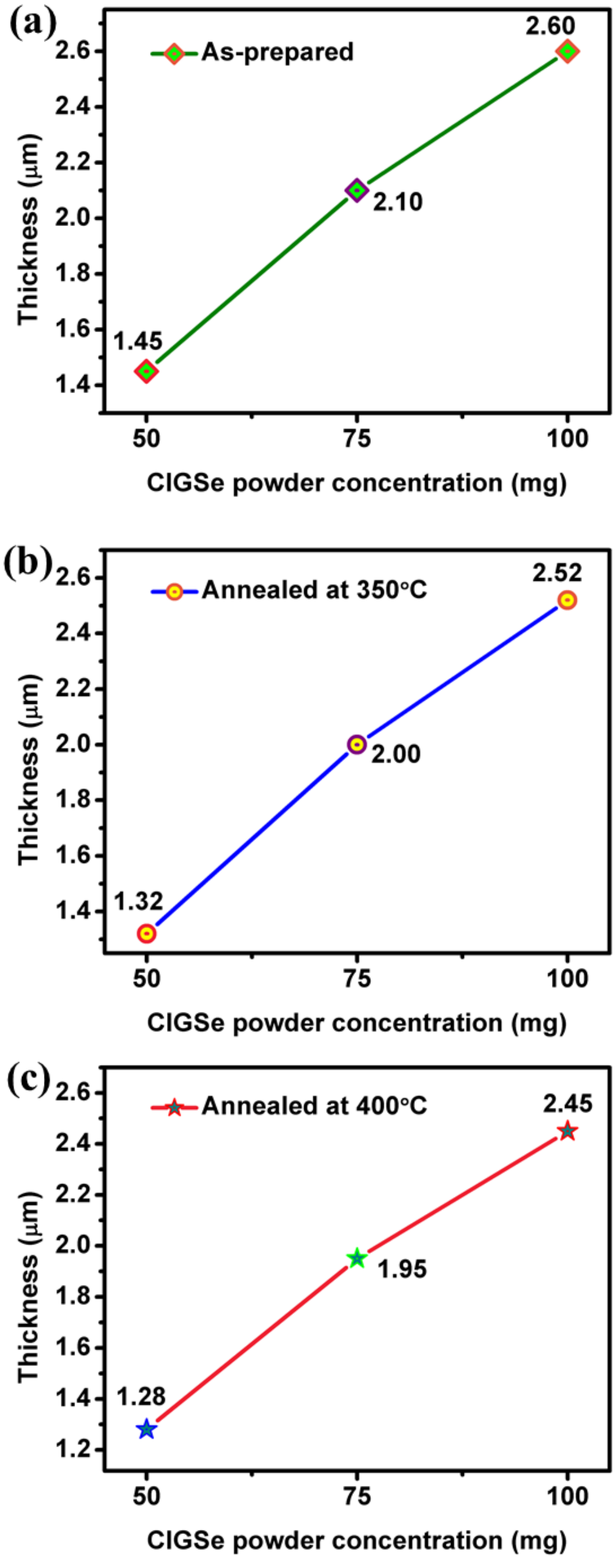

Fig. 5.2. Thickness of CIGSe film for different CIGSe powder concentration and annealing temperature.

The composition of CIGSe films prepared using different CIGSe powder concentration and annealed at different temperature is shown in **Table 5.1**. The observed composition of Cu:In:Ga:Se were similar to the powder (**Chapter 4**) for all the films. The as-prepared film showed the sulfur content of 2.07, 2.39 and 2.89 (at %) for 100, 75 and 50 mg CIGSe powder concentration respectively (**Fig. 5.3**). The observed sulfur content in the film is due to the solvent, used to formulate the ink. The as-prepared film showed carbon content of 46.75, 44.15 and 43.11 (at %) for 100, 75 and 50 mg of CIGSe powder concentration respectively (**Fig. 5.3**). The film annealed at 350 and 400^{o}C showed the decrement in the sulfur and carbon content as compared to as-prepared film.

Table 5.1. EDS composition of CIGSe film for different CIGSe powder concentration and annealing temperature.

Experimental conditions	CIGSe powder concentration (mg)	Composition (at %)				Cu/(In+Ga)	Ga/(In+Ga)
As-prepared	100	22.81	19	6.58	51.50	0.89	0.26
	75	22.49	18.92	6.98	51.60	0.87	0.27
	50	22.98	17.79	7.71	51.5	0.90	0.30
Annealed at 350^{o}C	100	22.79	18.68	6.73	51.79	0.90	0.26
	75	22.85	18.99	6.76	51.35	0.89	0.26
	50	22.65	18.96	6.78	51.55	0.88	0.26
Annealed at 400^{o}C	100	23.39	18.06	7.21	51.34	0.92	0.28
	75	23.16	18.74	6.61	51.47	0.91	0.26
	50	22.47	19.19	6.19	52.14	0.90	0.25

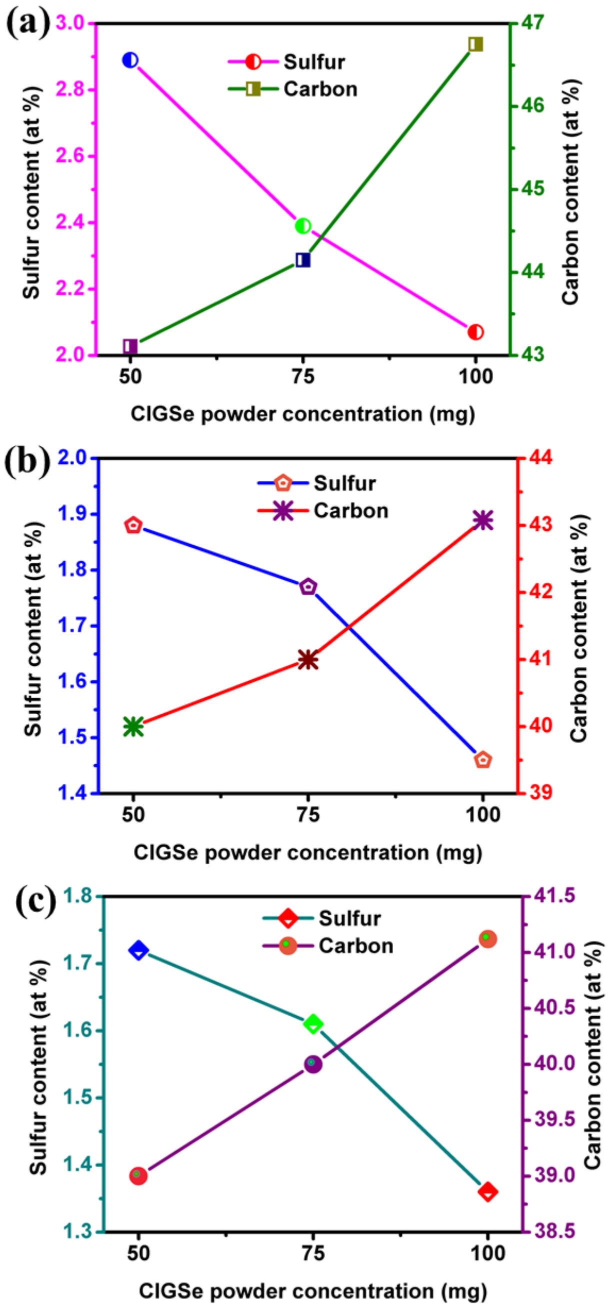

Fig. 5.3. Sulfur and carbon content in CIGSe films (a) As-prepared, (b) Annealed at 350^{o}C and (c) Annealed at 400^{o}C.

5.1.2. Influence of selenization temperatures

Films annealed at 350°C with powder concentration of 50 mg were further used for selenization process. **Fig. 5.4(a)** shows the XRD pattern of annealed and selenized

CIGSe films. The observed (112), (220) and (312) planes correspond to chalcopyrite crystal structure of CIGSe [JCPDS (35-1102)] [11] for all the cases. The calculated FWHM of (112) planes were 0.88, 0.55, 0.54 and 0.53° for annealed (An) at 350°C, selenized (Se)-500, Se-525 and Se-550°C respectively. The FWHM is decreased from 0.88 (annealed) to 0.53° (selenized) which indicates the improvement in the crystallinity after selenization. Raman spectra show the prominent peak at 178 cm^{-1} which correspond to A_1 mode of chalcopyrite structure of CIGSe for all the samples, resulting from vibration of Se anions in the x-y plane with cations of Cu, In and Ga are at rest [12]. As well, B_2/E modes of CIGSe are observed at around 229 cm^{-1} due to vibrations of anions and cations together [13]. All the film showed a broad peak at 155 cm^{-1}, indicates the presence of $Cu_2(In,Ga)_4Se_7$ phase of OVC [14] which was not detected by XRD.

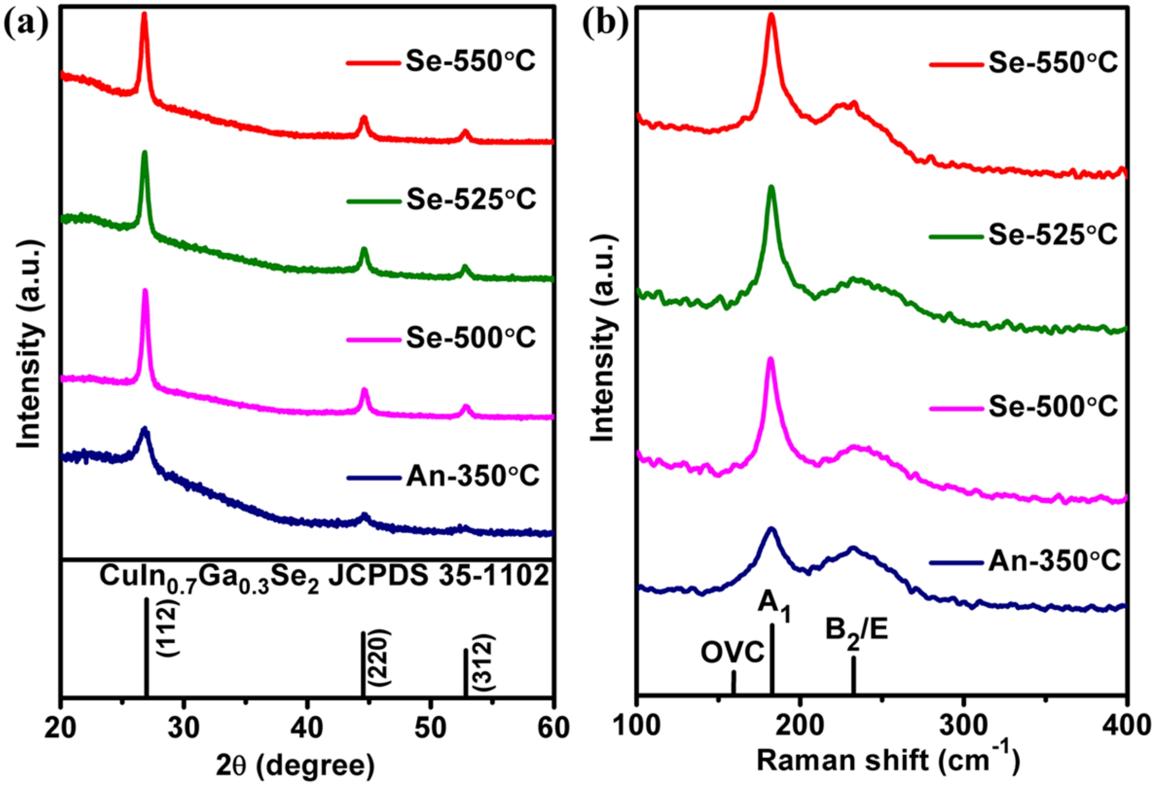

Fig. 5.4. (a) XRD pattern and (b) Raman spectra of annealed and selenized films.

Fig. 5.5 shows the planar and cross sectional FE-SEM images of CIGSe films annealed and selenized at different temperature. Annealed film showed smooth surface along with few cracks. Film selenized at 500°C, exhibited crack-free smooth surface. As the selenization temperature increases, cracks were increased. The observed cracks are due to differences in the thermal expansion coefficient between the CIGSe film and SLG substrate as discussed earlier [2]. Annealed film showed densely packed grains with uniform thickness of 1.32 µm as can be seen from the cross sectional image. After selenization, film thickness decreased from 1.32 to 1.1 µm due to evaporation of carbon and sulfur content as can be seen in **Table 5.3**. After selenization, compact film with slight increment in the grain size was observed as compared to annealed film.

EDS composition of annealed and selenized films are shown in **Table 5.2**. The observed composition for annealed film is similar to the powder. Film selenized at 500°C showed slight increment in the Se content, while Cu/(In+Ga) and Ga/(In+Ga) were remains unchanged. Further increasing selenization temperature, Se content decreased while Cu/(In+Ga) ratio increased.

From the EDS analysis, sulfur content was not detected after selenization and carbon content decreased from ~42 to 30 (at %) as can be seen in **Table 5.3**. As well, sodium content (< 2 at %) was observed which arises from the SLG substrate.

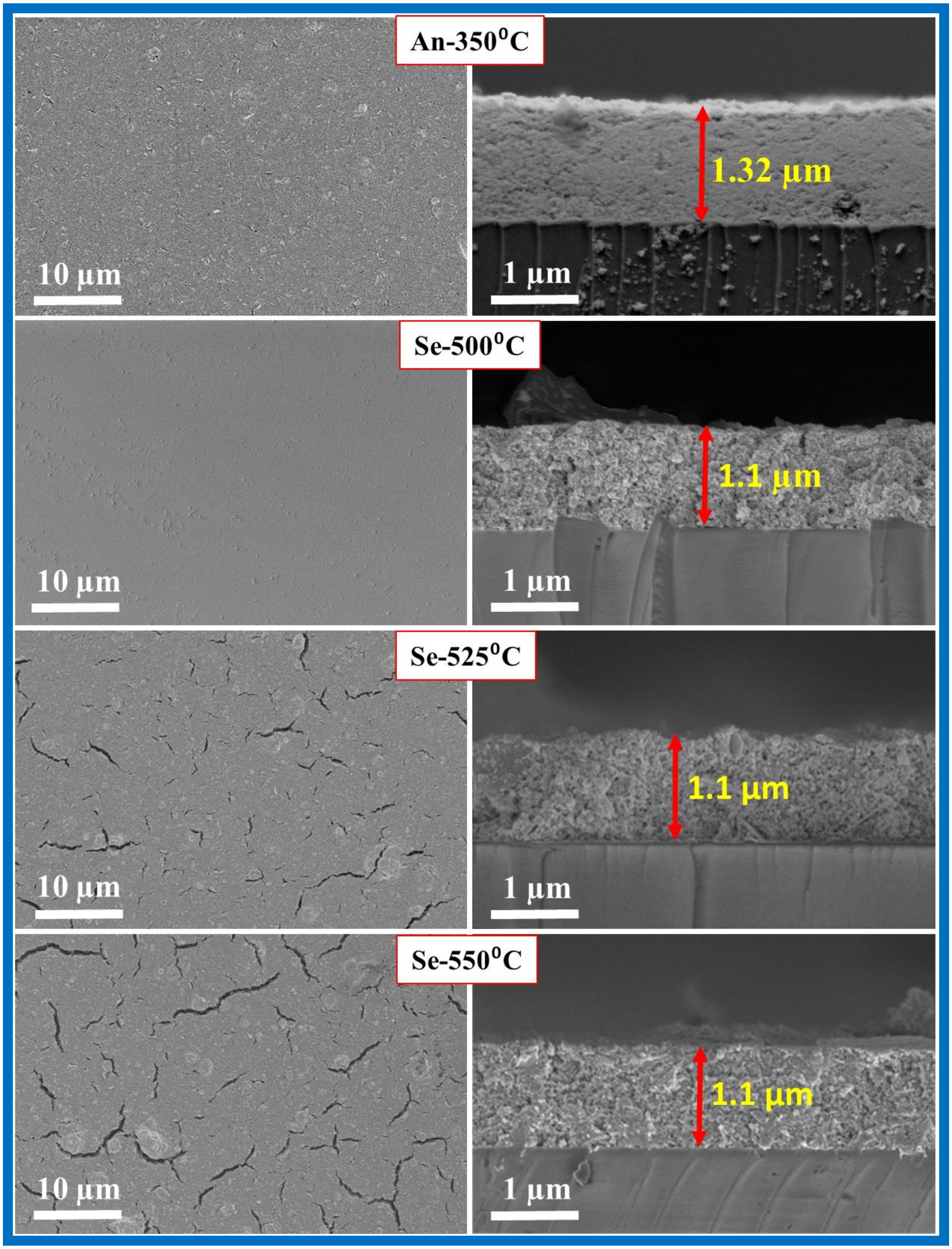

Fig. 5.5. Planar and cross sectional FE-SEM images of annealed and selenized CIGSe films.

Table 5.2. EDS composition of annealed and selenized CIGSe films.

Experimental conditions	Composition (at %)				Cu/ (In+Ga)	Ga/ (In+Ga)
	Cu	In	Ga	Se		
An-350 ℃	22.65	18.96	6.78	51.55	0.88	0.26
Se-500 ℃	19.81	16.14	6.11	57.93	0.89	0.31
Se-525 ℃	22.41	17.26	6.28	54.06	0.95	0.27
Se-550 ℃	22.86	16.87	6.32	53.95	0.98	0.27

Table 5.3. Sulfur, sodium, and carbon content observed from annealed and selenized films.

Experimental conditions	Sulfur (S) (at %)	Sodium (Na) (at %)	Carbon (C) (at %)
An-350 ℃	1.88	0.34	41.9
Se-500 ℃	-	1.62	30.04
Se-525 ℃	-	1.65	30.00
Se-550 ℃	-	1.85	29.97

5.1.3. Influence of NaCl treatment

Before selenization process, the film annealed at 350°C was dipped into 1M NaCl solution for 10 mins and influence of NaCl treatment on the properties of structural, morphological, compositional, optical, electrical and optoelectronic properties of CIGSe film were investigated.

Fig. 5.6 shows the XRD and Raman spectra of CIGSe films annealed at 350°C and selenized with NaCl treatment at different temperature. Fig. 5.6(a) shows the (112),

(220) and (312) planes, correspond to chalcopyrite crystal structure of CIGSe [**JCPDS (35-1102)**] **[11]** for all the samples. The calculated FWHM values of (112) planes are 0.88, 0.42, 0.39 and 0.33° for annealed (An) at 350°C, selenized (Se)-NaCl-500, Se-NaCl-525 and Se-NaCl-550°C respectively. The FWHM was decreased from 0.88 (annealed) to 0.33° (selenized) which indicates that improvement in the crystallinity after selenization. From the **Fig. 5.6(b),** A_1 mode peak of CIGSe was observed at around 178cm^{-1} which arises due to vibration of Se atoms with motionless neighbouring cations of Cu, In, and Ga **[12]**. Additionally, the B_2/E mode of CIGSe peak was observed at around 229 cm^{-1} for all the samples which represent the vibration of anions and cations together **[13]**. For all the cases, a broad peak was observed at 155 cm^{-1} which indicates the presence of $Cu_2(In,Ga)_4Se_7$ phase of OVC **[14]** which was not detected by XRD.

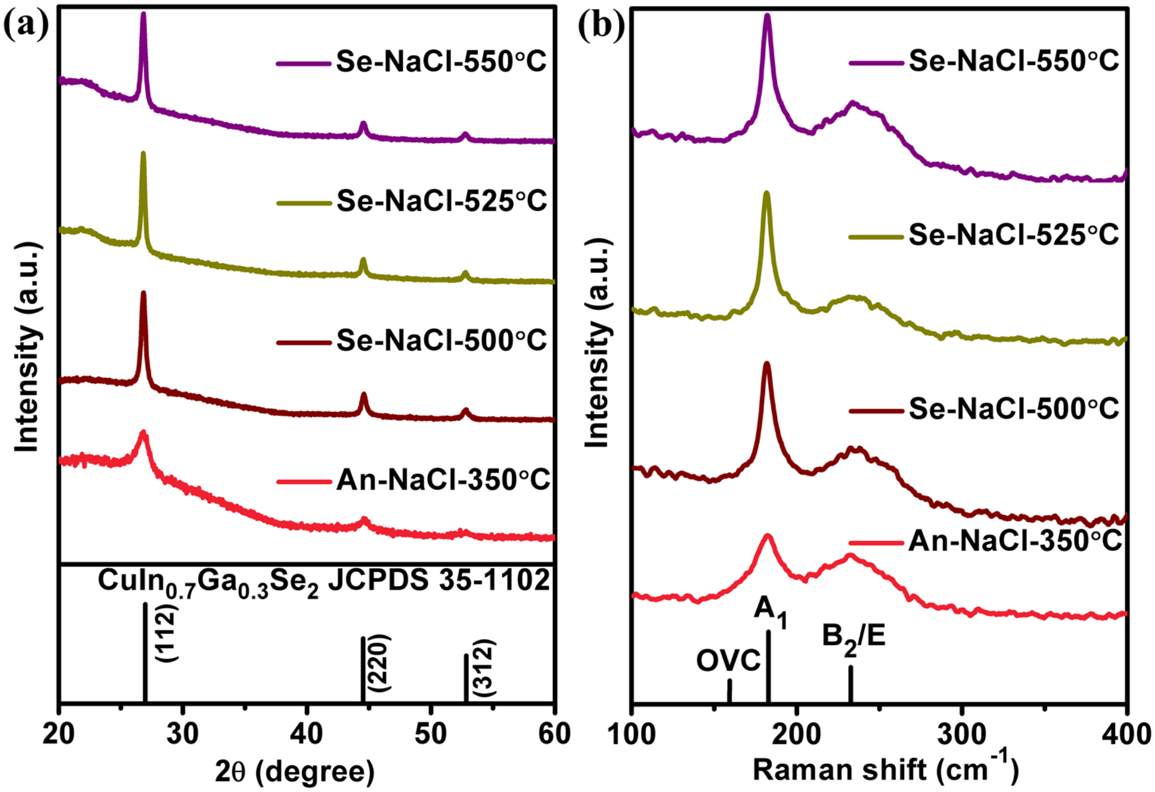

Fig. 5.6. (a) XRD pattern and (b) Raman spectra of annealed and selenized films with NaCl treatment for different temperature.

Fig. 5.7 shows the planar and cross sectional FE-SEM images of CIGSe films annealed at 350°C and selenized with NaCl for different temperature. At 350°C annealed film showed smooth surface along with very few cracks. The film selenized at 500°C showed very smooth and crack-free surface. As the selenization temperature increases cracks were increased which is due to differences in thermal expansion between the CIGSe film and SLG substrate as we discussed earlier [2]. The film annealed at 350°C showed uniform film thickness of 1.32 µm as can be seen from the cross sectional view of FE-SEM image. The film thickness reduced from 1.32 to 1 µm after selenization, which is due to evaporation of carbon and sulfur content as shown in Table 5.4. Compact and densely packed grains were observed for the film selenized at 500°C. As the selenization temperature increases, grain size as well as cracks increased.

As can be seen in Table 5.4, annealed film has similar composition as like powder. Film selenized at 500°C, showed slight increment in the Se content while Cu/(In+Ga) and Ga/(In+Ga) remains unchanged. The Cu/(In+Ga) ratio increased while Se content decreased with increases in the selenization temperature. After selenization, the carbon content decreased from ~42 to 30 (at %) and the sulfur content was not observed as shown in Table 5.5. The ~5 at % of sodium content was observed due to NaCl treatment and SLG substrate.

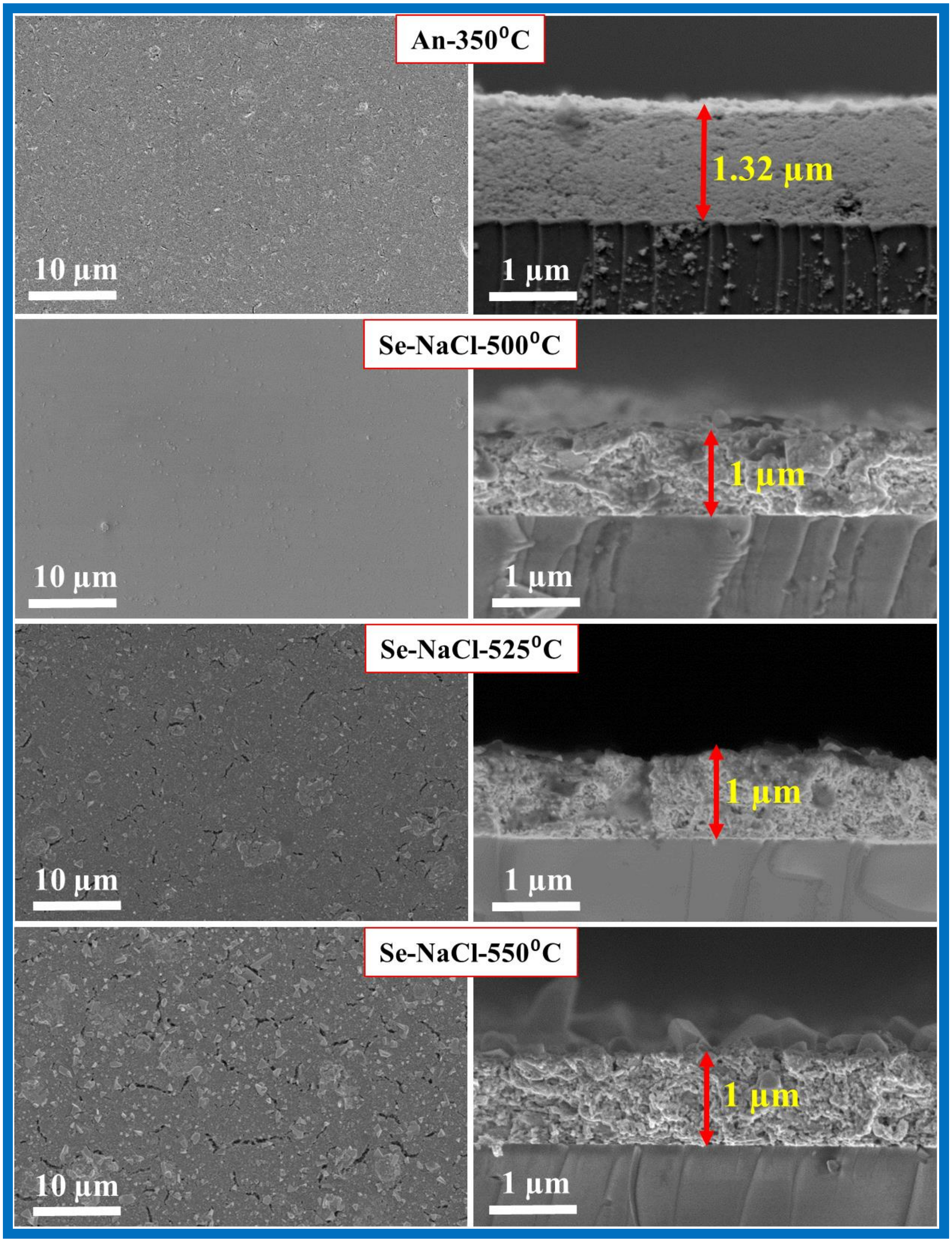

Fig. 5.7. Planar and cross sectional FE-SEM images of annealed and selenized CIGSe films with NaCl treatment for different temperature.

Table 5.4. EDS composition of CIGSe film annealed and selenized with NaCl treatment for different temperature.

Experimental conditions	Composition (at %)				Cu/ (In+Ga)	Ga/ (In+Ga)
	Cu	In	Ga	Se		
An-350 ℃	22.65	18.96	6.78	51.55	0.88	0.26
Se-NaCl-500 ℃	20.29	16.55	5.98	57.17	0.90	0.28
Se-NaCl-525 ℃	22.90	17.14	6.46	53.49	0.96	0.27
Se-NaCl-550 ℃	22.95	17.42	6.60	53.03	0.95	0.27

Table 5.5. Sulfur, sodium, and carbon content observed from the film annealed and selenized with NaCl treatment for different temperature.

Experimental conditions	Sulfur (S) (at %)	Sodium (Na) (at %)	Carbon (C) (at %)
An-350 ℃	1.88	0.34	41.9
Se-NaCl-500 ℃	-	5.31	31.05
Se-NaCl-525 ℃	-	5.6	30.82
Se-NaCl-550 ℃	-	5.08	30.01

Based on the above results, it's clear that Na has great influence on the structural and morphological properties. FWHM is decreased from 0.88 (An) to 0.42 (Se -NaCl-500°C) as can be observed from the structural analysis, which indicates the improvement in the crystallinity. FE-SEM images of film selenized with NaCl treatment showed increment in the grains size than selenized without NaCl treatment. The film selenized with NaCl treatment at 525 and 550°C showed 1 µm grains with fewer cracks on the surface as compared to film selenized without NaCl treatment. This improvement could be due to effective selenization process [15]. During the selenization process, elemental

Se provided by Se vapors react with Na which is in the CIGSe film leads polyselenide phases of Na_2Se_x around the CIGSe grains which subsequently act as a Se source [15]. These polyselenide phases react with metal cations of CIGSe promotes the grain growth and crystallization of CIGSe. Also, these polyselenide phases around CIGSe grains acts as a catalyst by supplying more Se than in Na-free samples and thus leading to a more efficient selenization [16].

5.1.4. Optical, electrical and optoelectronic properties of CIGSe films

Based on the above results, we have selected three best samples named as annealed at 350°C (An-350°C), selenized at 500°C (Se-500°C) and selenized with NaCl treatment at 500°C (Se-NaCl-500°C) for optical, electrical and optoelectronic analysis.

The optical absorption spectra of CIGSe films are shown in Fig. 5.8(a). The absorption started in the near infra-red region and gradually raised towards UV-Visible region for all the CIGSe films [17]. The band gap was calculated using Tauc plot by extra plotting the hν versus $(\alpha h\nu)^2$ as shown in Fig. 5.8(b). The calculated band gap values for An-350°C, Se-500°C and Se-NaCl-500°C were 1.36, 1.34 and 1.31 eV respectively.

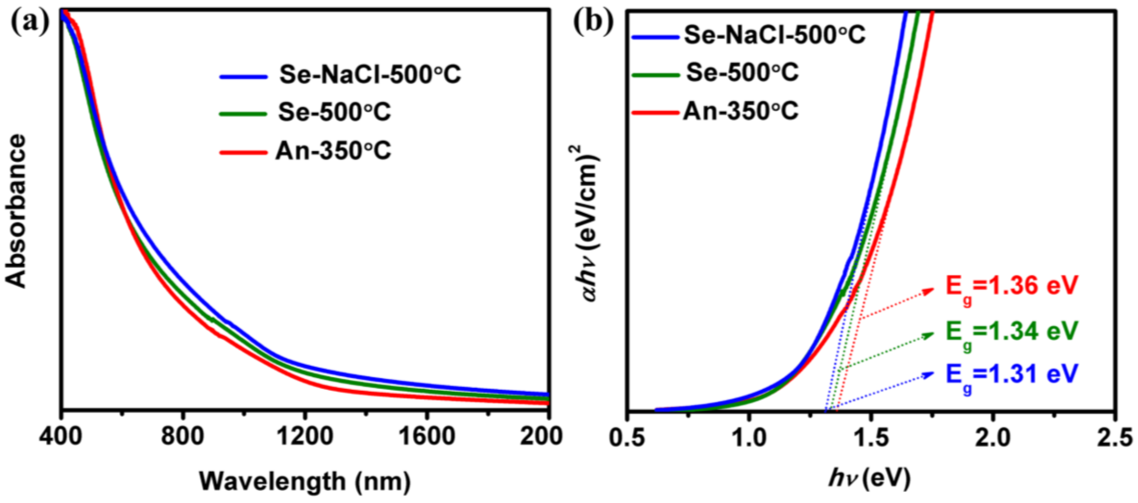

Fig. 5.8. (a) UV-VIS-NIR absorption spectra and (b) Corresponding band gap of CIGSe films.

The conductivity type, carrier concentration, mobility and resistivity of CIGSe films are given in the **Table 5.6**. All the CIGSe films showed P-type conductivity with the carrier concentration in the order between 10^{17} and 10^{18} cm^{-3}. The mobility of CIGSe films were 1.26, 2.12 and 3.62 cm^2/Vs for An-350°C, Se-500°C, and Se-NaCl-500°C, respectively. After selenization, carrier concentration increased while resistivity of films decreased from 53 to 36 Ωcm. This could be due to an enhancement in the grain size as we observed from the FE-SEM images **[18]**. The optimum carrier concentration required for CIGSe solar cell applications are in the order between 10^{16} and 10^{18} **[19]**. It is remarkable that the prepared CIGSe films exposed the carrier concentration in the order of 10^{17-18} cm^{-3}, indicating their potential application in the field of solar cells. After selenization, the mobility increased while resistivity decreased which could be due to increment in the grain size as observed from FE-SEM analysis. Increase in grain size reduces the grain boundary density and thus leads to increases the conductivity (decreases the resistivity). Hence the mobility of charge carrier increases **[20]**. In addition, these results prove that the prepared CIGSe films possess nearly similar electrical properties as vacuum deposited films **[21,22]**. Thus, it could be a possible way to scale-up the non-vacuum based CIGSe film deposition.

Table 5.6. Conductivity type, carrier concentration, mobility, and resistivity of CIGSe films.

Experimental conditions	Type of conductivity	Carrier concentration (cm^{-3})	Mobility (cm^2/Vs)	Resistivity (Ωcm)
An-350 ℃	P	1.62×10^{17}	1.26	53
Se-500 ℃	P	2.47×10^{17}	2.12	45
Se-NaCl-500 ℃	P	4.91×10^{18}	3.62	36

To perform I-V measurement, gold (Au) circular contacts with a diameter of 0.1 cm was deposited by thermal evaporation method onto CIGSe film. I-V measurements were carried out between two Au contacts separated by 0.2 cm. A voltage of 10 V was applied across the two Au contacts as shown in **Fig. 5.9**. The resulting current flows across the film between two contacts were measured. I-V measurement of CIGSe film was done in dark and under an illumination of light (tungsten lamp, 300 W) shown in Fig. 5.10. The current increases linearly with the voltage, which implies the ohmic nature of the Au contacts as reported by other researchers [23]. The photoconductivity of the CIGSe film can be expressed by ΔI (the current difference in the dark and under illumination at a given bias voltage) [24]. The photoconductivity of An-350°C, Se-500°C, and Se-NaCl-500°C films were 2.35, 3.91 and 4.39-fold, respectively. After selenization, CIGSe films showed an increment in the photoconductivity which could be due to the smooth surface of the film along with increment in the grain size. The illumination excites electrons in the valence band to the conduction band and then increases the holes in the CIGSe, which enhances the conductivity of the film. According to the literature, CIGSe films made out of nano-sized particles did not show high photoconductivity [25]. This is due to the presence of small grains leading to a high density of grain boundaries that can serve as recombination centers. In the present work, the exposed photo current could be due to the low density of grain boundaries because of large sized grains which are beneficial to reduce the recombination rate of carriers. The result of photo conductivity also reveals, the synthesized CIGSe sub-micron sized grains have a great potential to be used as an absorber layer in the photovoltaic devices.

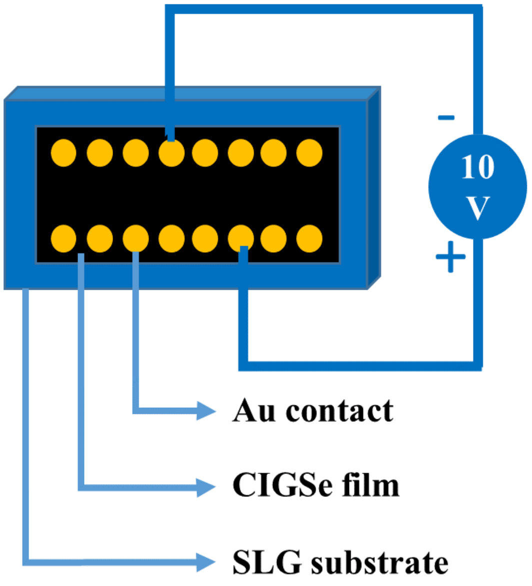

Fig. 5.9. Schematic representation of I-V measurement.

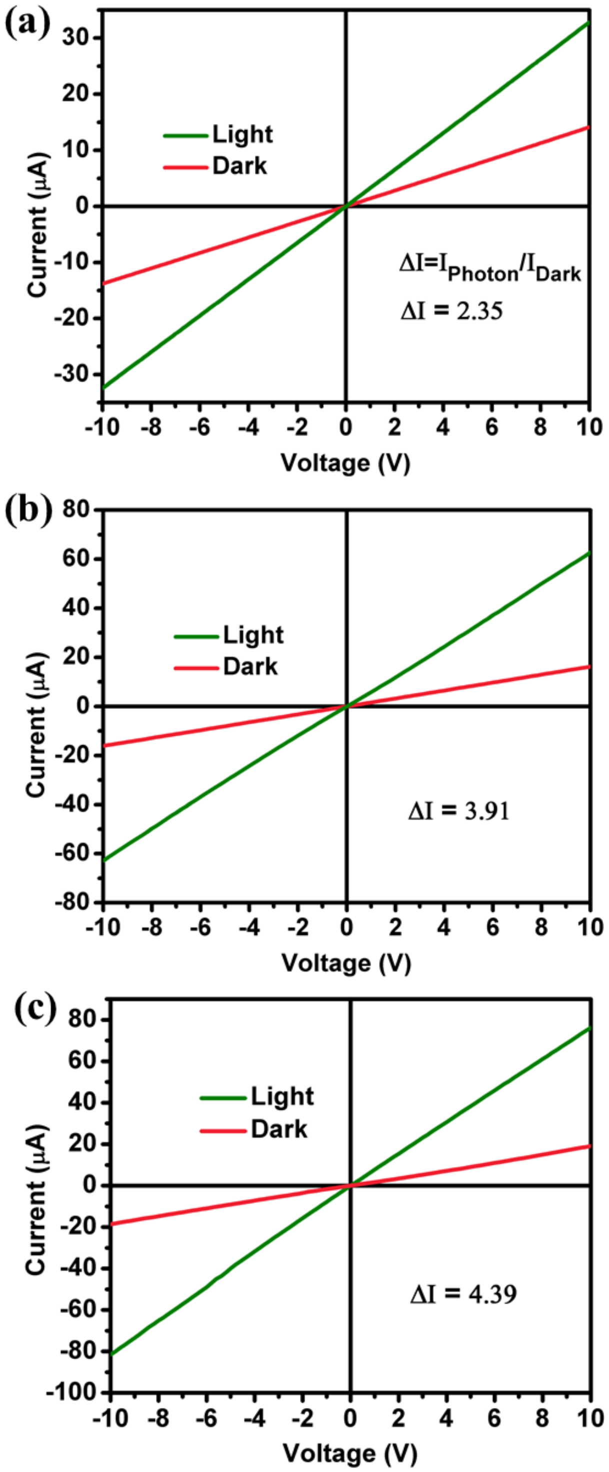

Fig. 5.10. I-V curve of CIGSe films (a) An-350°C, (b) Se-500°C and (c) Se-NaCl-500°C.

5.2.Summary

- ✓ Films were prepared by doctor blade method using the $Cu_{0.8}(In_{0.7},Ga_{0.3})Se_2$ submicron particles synthesized at 260°C for 4h. CIGSe ink concentration and air annealing temperature were optimized to get crack-free films with thickness of ~1 µm.
- ✓ Firstly, CIGSe powder concentration was varied such as 50, 75 and 100 mg in 500 µL hexanethiol. With increases in the powder concentration, cracks were increased due to increases in the CTE value of CIGSe. The film thickness increased from 1.45 to 2.60 µm as the powder concentration increases. Sulfur content decreased while carbon content increased with increases in the powder concentration. Air annealing temperatures of CIGSe films were varied such as 350 and 400°C. The cracks were increased as the annealing temperature increases for all the CIGSe powder concentration. This might be due to changes in the CTE of CIGSe and SLG substrate. Also, the observed cracks after annealing could be due to the shrinkage of CIGSe. With increases in the air annealing temperature, the sulfur and carbon contents were decreased. The thickness of CIGSe films reduced as the annealing temperature increases which is due to evaporation of sulfur and carbon content.
- ✓ The CIGSe film annealed at 350°C was used for selenization process. The selenization temperature was varied such as 500, 525 and 550°C for 20 mins. The calculated FWHM decreased from 0.88 (annealed) to 0.53° (selenized) which indicates the improvement in the crystallite and grain size. After selenization, film thickness decreased from 1.32 to 1.1 µm because of evaporation of carbon and sulfur content. The film selenized at 500°C showed crack-free smooth surface. As the selenization temperature increases, cracks were increased which is due to the differences in the thermal expansion between the CIGSe film and SLG substrate. After selenization, the carbon content decreased from ~42 to 30 (at %).
- ✓ The NaCl treatment was performed for the film annealed at 350°C before selenization process. The selenization was carried out for different temperature such as 500, 525 and 550°C. The FWHM of (112) plane was decreased from 0.88 (annealed) to 0.33° (selenized). After selenization, thickness of the films was

decreased from 1.32 to 1 µm due to evaporation of carbon and sulfur content. The film selenized at 500°C showed smooth and crack-free surface. As the selenization temperature increases, cracks were increased due to difference thermal expansion between the CIGSe film and SLG substrate. The carbon content decreased from ~42 to 30 (at %) after selenization. The 5 at % of sodium was observed due to NaCl treatment and SLG substrate.

- ✓ The UV-VIS-NIR absorption spectra, hall measurement, and I-V characteristics were carried out for the films annealed at 350°C, selenized at 500°C and selenized with NaCl treatment at 500°C. All these films showed nearly similar bandgap of ~ 1.35 eV which is optimum for absorber material in CIGSe solar cells. The selenized film showed increment in the carrier concentration which could be due to the enhancement in grain size as observed from the FE-SEM images. After selenization, the mobility increased while resistivity decreased which could be due to increament in the grain size as observed from FE-SEM analysis. Increases in the grain size reduces the grain boundary density and thus leads to increases the conductivity. After selenization, CIGSe films showed high photo-current response which could be due to the improvement in the mobility and decrement in the resistivity.

References

[1] W. Fang, C.-Y. Lo, On the thermal expansion coefficients of thin films, Sensors Actuators A Phys. 84 (2000) 310–314. doi:10.1016/S0924-4247(00)00311-3.

[2] F. Kessler, D. Rudmann, Technological aspects of flexible CIGS solar cells and modules, Sol. Energy. 77 (2004) 685–695. doi:10.1016/j.solener.2004.04.010.

[3] P. De Lima-Neto, A.N. Correia, G.L. Vaz, P.N.S. Casciano, Morphological, structural, microhardness and corrosion characterisations of electrodeposited Ni-Mo and Cr coatings, J. Braz. Chem. Soc. 21 (2010) 1968–1976. doi:10.1590/S0103-50532010001000024.

[4] E.-H.A. Mohamed, The Effect of Annealing Treatments on Spherulitic Morphology and Physical Ageing on Glass Transition of Poly Lactic Acid (PLLA), Mater. Sci. Appl. 2 (2011) 439–443. doi:10.4236/msa.2011.25058.

[5] P. De Lima-Neto, A.N. Correia, G.P. Da Silva, Structural and morphological investigations of the electrodeposited Cr and Ni-Cr-P coatings and their electrochemical behaviors in chloride aqueous medium, J. Braz. Chem. Soc. 17 (2006) 1419–1427. doi:10.1590/S0103-50532006000700032.

[6] S. Guo, I. Lundström, H. Arwin, Temperature sensitivity and thermal expansion coefficient of benzocyclobutene thin films studied with ellipsometry, Appl. Phys. Lett. 68 (1996) 1910–1912. doi:10.1063/1.116291.

[7] https://www.google.com/patents/WO2015056001A1?cl=en.

[8] https://www.google.com/patents/US20100236616.

[9] C. Liewhiran, S. Phanichphant, Improvement of flame-made ZnO nanoparticulate thick film morphology for ethanol sensing, Sensors. 7 (2007) 650–675. doi:Doi 10.3390/S7050650.

[10] P. Xu, A.S. Mujumdar, B. Yu, Drying-Induced Cracks in Thin Film Fabricated from Colloidal Dispersions, Dry. Technol. 27 (2009) 636–652. doi:10.1080/07373930902820804.

[11] Z. Han, D. Zhang, Q. Chen, R. Hong, C. Tao, Y. Huang, Z. Ni, S. Zhuang, Synthesis of single phase chalcopyrite $CuIn_{1-x}Ga_xSe_2$ ($0 \leq x \leq 1$) nanoparticles by one-pot method, Mater. Res. Bull. 51 (2014) 302–308.

doi:10.1016/j.materresbull.2013.12.041.

[12] A.Chirilă, S.Seyrling, S.Buecheler, D.Guettler, S.Nishiwaki, Y. E. Romanyuk, G.Bilger and A.N. Tiwari, Influence of high growth rates on evaporated Cu(In,Ga)Se_2 layers and solar cells, Prog. Photovolt: Res. Appl. 20 (2012) 209–216. doi: 10.1002/pip.1122.

[13] J. Liu, D.M. Zhuang, M.J. Cao, C.Y. Wang, M. Xie, X.L. Li, Preparation and characterization of Cu(In,Ga)Se_2 thin films by selenization of $Cu_{0.8}Ga_{0.2}$ and In_2Se_3 precursor films, Int. J. Photoenergy. 2012 (2012). doi:10.1155/2012/149210.

[14] W. Witte, R. Kniese, M. Powalla, Raman investigations of Cu(In,Ga)Se_2 thin films with various copper contents, Thin Solid Films. 517 (2008) 867–869. doi:10.1016/j.tsf.2008.07.011.

[15] D. Braunger, D. Hariskos, G. Bilger, U. Rau, H.W. Schock, Influence of sodium on the growth of polycrystalline Cu(In,Ga)Se_2 thin films, Thin Solid Films. 361 (2000) 161–166. doi:10.1016/S0040-6090(99)00777-4.

[16] F. Hergert, S. Jost, R. Hock, M. Purwins, J. Palm, Formation reactions of chalcopyrite compounds and the role of sodium doping, Thin Solid Films. 515 (2007) 5843–5847. doi:10.1016/j.tsf.2006.12.037.

[17] J. Li, Z. Jin, T. Liu, J. Wang, D. Wang, J. Lai, H. Du, L. Cui, Ternary and quaternary chalcopyrite $Cu(In_{1-x}Ga_x)Se_2$ nanocrystals: organoalkali-assisted diethylene glycol solution synthesis and band-gap tuning, CrystEngComm. 15 (2013) 7327. doi:10.1039/c3ce40813b.

[18] M.G. Tsai, H.T. Tung, I.G. Chen, C.C. Chen, Y.F. Wu, X.D. Qi, Y. Hwu, C.Y. Lin, P.H. Wu, C.W. Cheng, Annealing Effect on the Properties of $Cu(In_{0.7}Ga_{0.3})Se_2$ Thin Films Grown by Femtosecond Pulsed Laser Deposition, J. Am. Ceram. Soc. 96 (2013) 2419–2423. doi:10.1111/jace.12422.

[19] M. Turcu, U. Rau, Compositional trends of defect energies, band alignments, and recombination mechanisms in the Cu(In,Ga)$(Se,S)_2$ alloy system, Thin Solid Films. 431–432 (2003) 158–162. doi:10.1016/S0040-6090(03)00225-6.

[20] Z. Seboui, A. Gassoumi, Y. Cuminal, N.K. Turki, The post-growth effect on the properties of Cu_2ZnSnS_4 thin films, J. Renew. Sustain. Energy. 7 (2015) 1–11.

doi:10.1063/1.4908063.

[21] L. Zhang, F. Liu, F. Li, Q. He, B. Li, C. Li, Structural, optical and electrical properties of low-temperature deposition Cu(In_xGa_{1-x})Se_2 thin films, Sol. Energy Mater. Sol. Cells. 99 (2012) 356–361. doi:10.1016/j.solmat.2012.01.002.

[22] S.U. Park, R. Sharma, K. Ashok, S. Kang, J.K. Sim, C.R. Lee, A study on composition, structure and optical properties of copper-poor CIGS thin film deposited by sequential sputtering of CuGa/In and In/(CuGaIn) precursors, J. Cryst. Growth. 359 (2012) 1–10. doi:10.1016/j.jcrysgro.2012.08.013.

[23] S. Sarkar, K. Bhattacharjee, G.C. Das, K.K. Chattopadhyay, Self-sacrificial template directed hydrothermal route to kesterite-Cu_2ZnSnS_4 microspheres and study of their photo response properties, CrystEngComm. 16 (2014) 2634. doi:10.1039/c3ce42229a.

[24] M. Li, W.-H. Zhou, J. Guo, Y.-L. Zhou, Z.-L. Hou, J. Jiao, Z.-J. Zhou, Z.-L. Du, S.-X. Wu, Synthesis of Pure Metastable Wurtzite CZTS Nanocrystals by Facile One-Pot Method, (2012). doi:10.1021/jp307346k.

[25] M.G. Panthani, V. Akhavan, B.W. Goodfellow, J.P. Schmidtke, L. Dunn, A. Dodabalapur, P.F. Barbara, B. A. Korgel, Synthesis of $CuInS_2$, $CuInSe_2$, and Cu(In_xGa_{1-x})Se_2 (CIGS) Nanocrystal “Inks” for Printable Photovoltaics, 2 (2008) 16770–16777. doi/abs/10.1021/ja805845q.

Chapter 6

Hot injection synthesis of CIGSe nanoparticles and deposition of films

In this chapter, we discuss about the synthesis of $Cu(In,Ga)Se_2$ (CIGSe) nanoparticles by low temperature hot injection process. We studied the effect of reaction parameters such as reaction temperature and reaction time. Furthermore, the reaction mechanism of CIGSe was proposed. Several properties of CIGSe nanoparticles was studied using characterization techniques such as XRD, Raman, FE-SEM, TEM, EDS, UV-VIS-NIR and XPS.

The films are prepared using optimized CIGSe nanoparticles. Then, various properties of CIGSe films was examined using characterization techniques such as XRD, FE-SEM, EDS, UV-VIS-NIR, Hall effect and current-voltage (I-V) measurement.

6.1. Synthesis of CIGSe nanoparticles

CIGSe nanoparticles was synthesized by optimizing the most important reaction parameters such as reaction temperature and reaction time. The prime objective of this optimization is to get pure phase CIGSe while maintaining stoichiometric composition. We have successfully synthesized CIGSe nanoparticles at 180°C with reaction time of 16h.

6.1.1. Influence of reaction temperature

XRD pattern of CIGSe samples synthesized at different reaction temperature are shown in **Fig. 6.1**. For all the samples, (112), (220) and (312) planes were observed which corresponds to chalcopyrite crystal structure of CIGSe. With decreases in the reaction temperature, diffraction peaks of CIGSe was shifted to higher 2ϴ values which indicates the increment in the Ga content as can be observed from the EDS analysis [**Fig. 6.5(a)**]. To see the diffraction peak shift clearly, the magnified view of (112) plane is shown in **Fig. 6.1(b)**. A peak of (220) plane is not symmetric towards higher 2ϴ value which is due to compositional deviation in the CIGSe. In addition to that, the peak observed at 2ϴ value of 31.11° matches to (006) plane of β-CuSe (JCPDS-27-0184) which is due to Cu-rich composition as can be seen in Fig. 6.5(b).

The average crystallite size (L) was calculated using Scherrer formula [1]:

$$L = \frac{K\lambda}{\beta \cos\theta} \quad - - - - - - - - \rightarrow (1)$$

where, K is a constant (0.9), λ is the X-ray wavelength (1.5406 Å), β is the Full Width Half Maximum (FWHM) and Θ is the diffraction angle from XRD spectrum. The calculated crystallite size of synthesized CIGSe samples at different reaction temperature is shown in Fig. 6.2. From the figure, it is clear that the crystallite size increased from 24.58 to 36.04 nm as the reaction temperature increases. This results are in good accordance with FE-SEM results which shows an increment in the grain size as a function of reaction temperature.

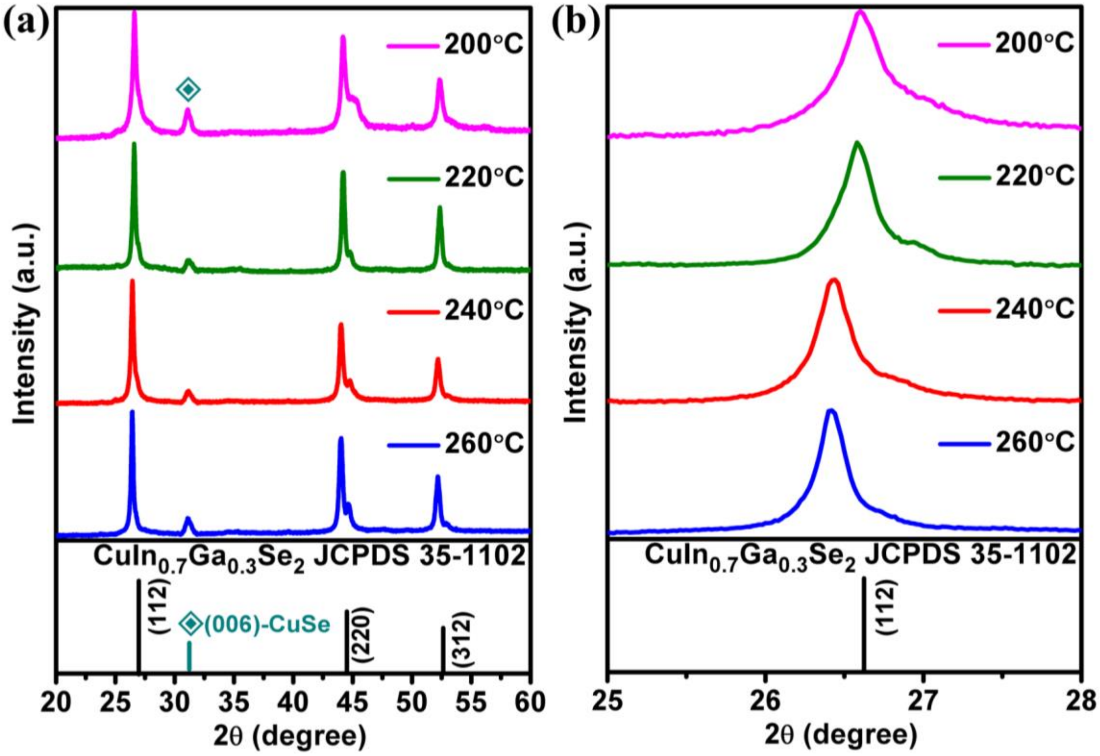

Fig. 6.1. (a) XRD pattern of synthesized CIGSe samples at different reaction temperature and (b) Magnified view of (112) plane.

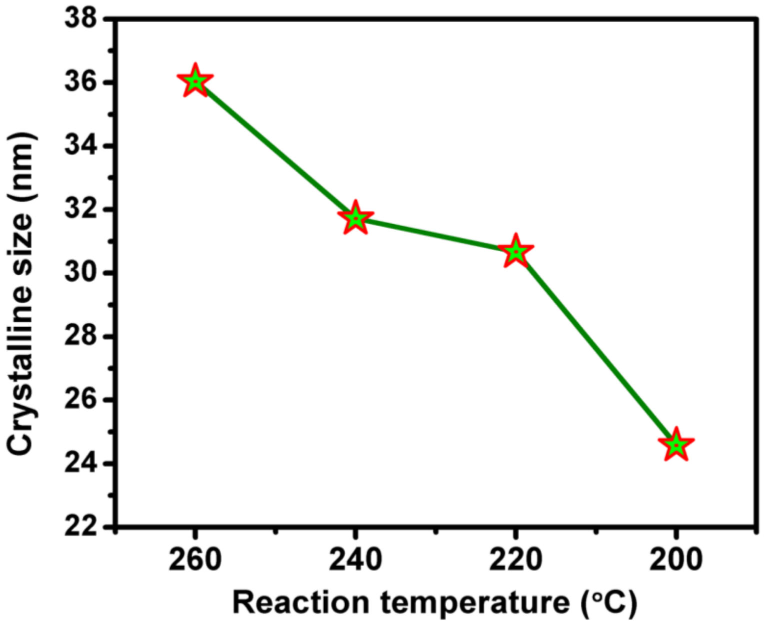

Fig. 6.2. Crystallite size of synthesized CIGSe samples at different reaction temperature.

Raman analysis was further used to confirm the phase purity of CIGSe samples. Fig. 6.3 shows the Raman spectra of synthesized CIGSe samples at different reaction temperature. All the samples showed a peak at around 173 cm^{-1}, corresponds to chalcopyrite crystal structure of A_1 mode [2]. Basically, A_1 mode is a pure anionic mode in which Se atoms vibrate with motionless neighbouring cations. As the reaction temperature decreases, the A_1 mode peak is gradually shifted to higher wavenumber which is due to increases in the Ga content [3,4]. Additionally, A_1 mode of CuSe peak was observed at 258 cm^{-1} for all the samples because of Cu-rich composition [5,6]. As the reaction temperature decreases, intensity of CuSe peak increased which is due to increment in Cu content as can be seen in Fig. 6.5(a). The increases in the Cu content is might be due to higher reactivity of Cu at lower reaction temperature.

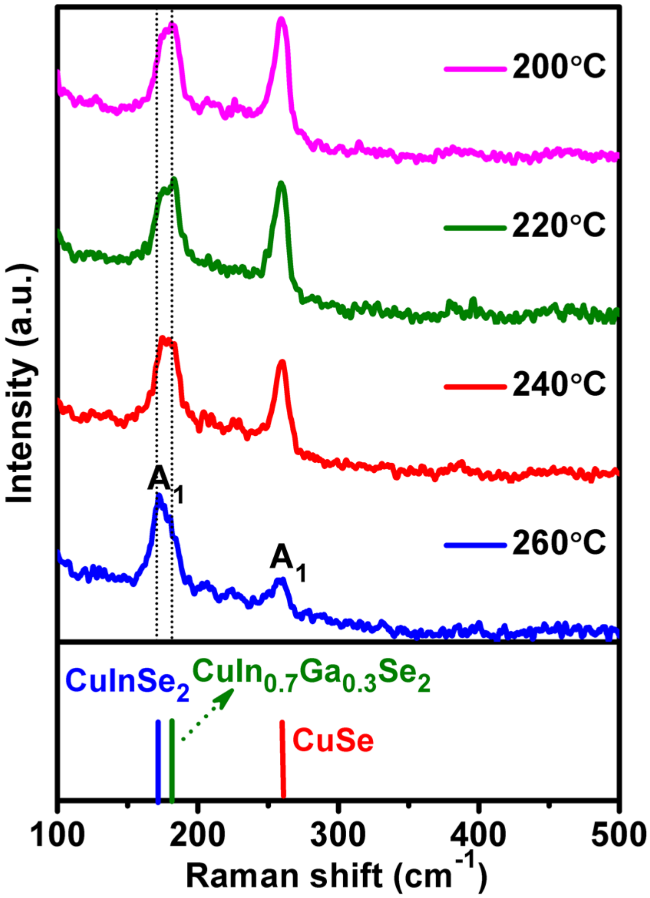

Fig. 6.3. Raman spectra of synthesized CIGSe samples at different reaction temperature.

FE-SEM images of synthesized CIGSe samples at different reaction temperature are shown in **Fig. 6.4**. With decreases in the reaction temperature, particles sizes were decreased from 40 to 25 nm. The reactivity of precursor might be decreasing as the reaction temperature decrease which could inhibit the growth of the crystals **[7]**. EDS composition of CIGSe samples synthesized at different reaction temperature is shown in **Fig. 6.5(a)**. As the reaction temperature decreases, Cu content increased while Se content decreased which leads to the formation of CuSe phase as evidenced from structural analysis. Besides, Ga content increases as a function of reaction temperature which led to the peak shift in structural analysis. The Cu/(In+Ga) and Ga/(In+Ga) ratios was calculated from the EDS composition [**Fig. 6.5(a)**]. From the **Fig. 6.5(b)**, increment in the Cu/(In+Ga) ratio was observed due to increases in the Cu reactivity as Cu has higher reactivity at lower reaction temperature. When the reaction temperature was greater than 200°C, the Ga-poor composition was observed [8]. The structural and compositional analysis reveals the increment in the Ga content as the reaction temperature decreases.

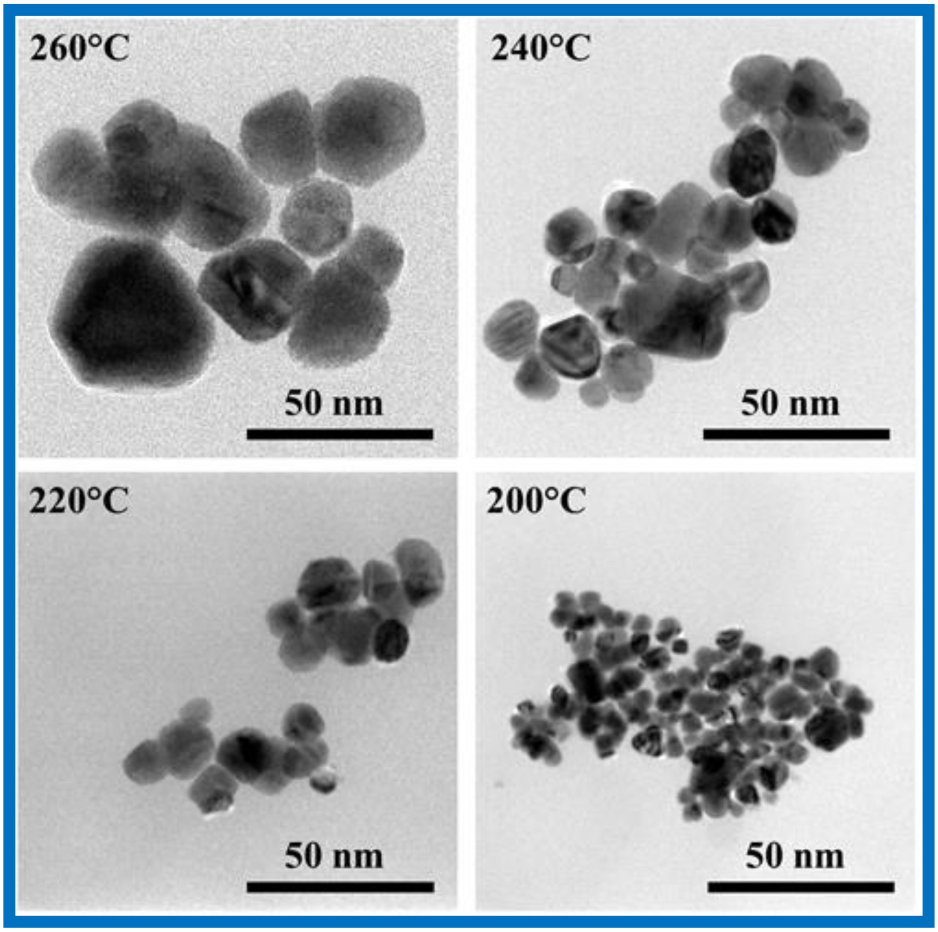

Fig. 6.4. FE-SEM images of synthesized CIGSe samples at different reaction temperature.

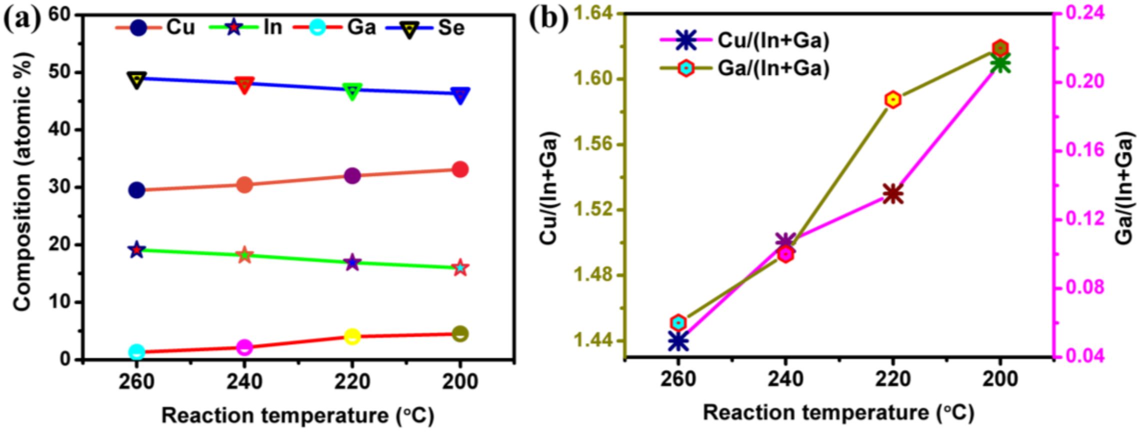

Fig. 6.5. (a) EDS composition of synthesized CIGSe samples at different reaction temperature and (b) corresponding Cu/(In+Ga) and Ga/(In+Ga) ratio.

6.1.2. Influence of reaction time

As we discussed in the previous section, 180°C is considered to be an optimum temperature which we used for further experiments. The aliquots were withdrawn at regular intervals from 0 min to 24h to study the growth and formation mechanism of CIGSe. **Fig. 6.6** shows the XRD pattern of CIGSe samples synthesized at different reaction time. At 0 min, (006), (133), (028) and (206) planes were observed which matches well with orthorhombic crystal structure of β-CuSe phase (**JCPDS-27-0184**) **[9]**. As the reaction time prolonged to 10 min, (112), (220) and (312) planes were observed which correspond to chalcopyrite crystal structure of CIGSe. However, peak position of these planes were shifted towards lower 2ϴ values from JCPDS data **(35-1102)** which indicates the lower Ga content. In addition to that, the (006), (133), (028) planes for β-CuSe phase was observed. **Fig. 6.7(a)** shows the magnified view in the 2ϴ range from 47 to 50° to see clearly the presence of (133) and (028) β-CuSe planes. When the reaction time was between 20 min and 2h, β-CuSe planes of (133), (028) and (206) were disappeared as can be seen in **Fig. 6.6** and **Fig. 6.7(b)**. The XRD pattern of sample synthesized at reaction time between 20 min and 2h are shown in **Fig. 6.7(b)** to determine the less intense peaks. From the figure, peak splitting was observed for (112) and (220) planes which is due to the deviation in the Ga content. Additionally, we observed (006) plane of β-CuSe phase because of Cu-rich composition. As the reaction time increased to 4h, β-CuSe plane was disappeared and peak splitting of CIGSe was observed which strongly indicates the different Ga content distribution. When the reaction time further increased to 16h, formation of pure phase CIGSe was confirmed by presence of single narrow peak. Moreover, all the peak position were well indexed with JCPDS data (35-1102). The XRD results confirmed that the β-CuSe is acted as seed to form the pure phase CIGSe.

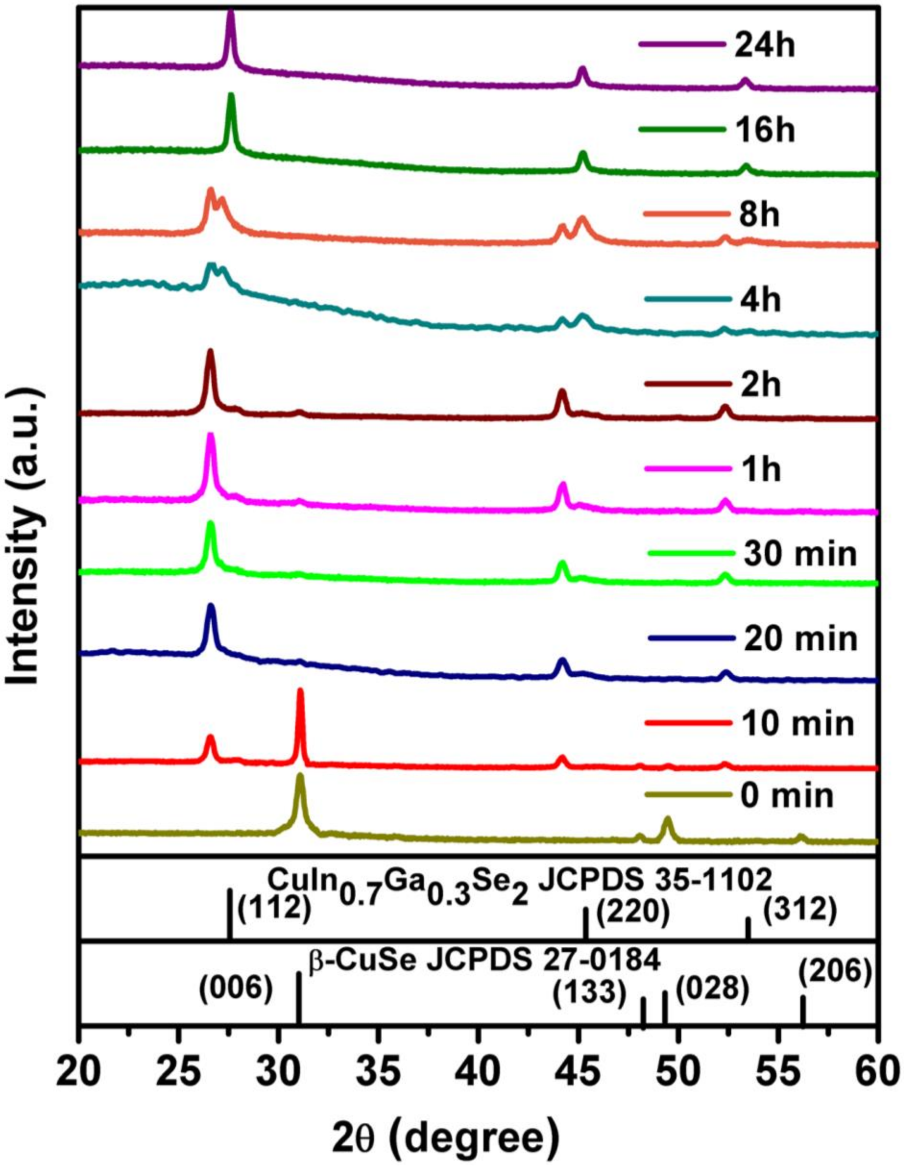

Fig. 6.6. XRD pattern of synthesized CIGSe samples at different reaction time.

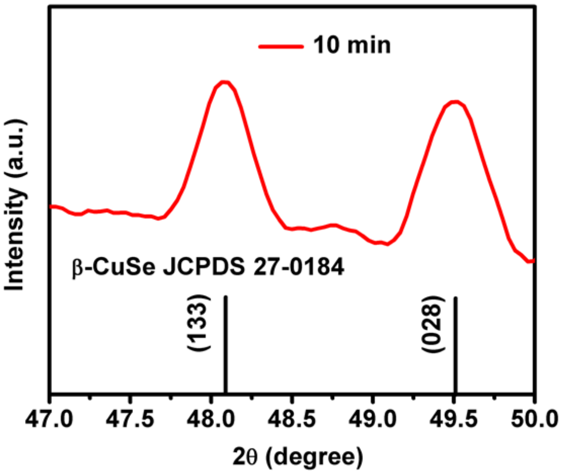

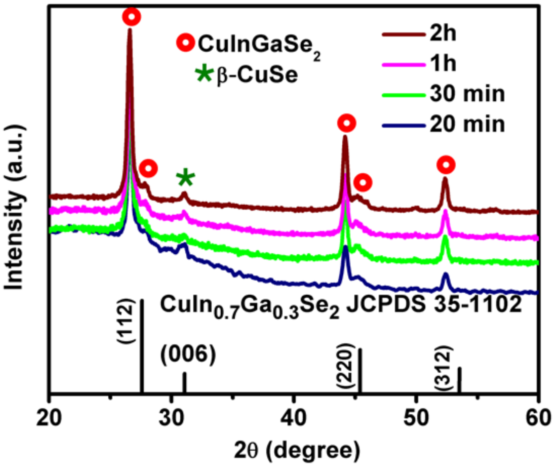

Fig. 6.7. (a) XRD spectrum of magnified view of 2Ө range from 47 to 50° for the sample synthesized at 10 min and (b) XRD pattern of synthesized CIGSe samples at reaction time from 20 min to 2h.

Raman analysis was used to further investigate the phase formation of CIGSe samples. Fig. 6.8 shows the Raman spectra of synthesized CIGSe samples at different reaction time. At 0 min, a peak observed at around 258 cm^{-1} which corresponds to A_1 mode of CuSe [5,6]. By prolonging the reaction time to 10 min, CuSe and CIGSe (less intense) peaks were observed as can be seen in Fig. 6.8. The sample synthesized at 10 min is shown in Fig. 6.9 in order to see a less intensity peak clearly. When the reaction time is between 20 min and 8h, we observed the A_1 mode peak of CIGSe [2] as well as CuSe [5,6]. As the reaction time increases up to 8 h, intensity of CuSe peak decreased while CIGSe peak increased which is due to the phase conversion from CuSe to CIGSe. Besides, the observed CIGSe peak has splitting because of variation in the Ga content. When the reaction time increase to 16h, the splitted CIGSe peak appeared as a narrow and pure CIGSe phase was confirmed. As well as, we could observe the peak shift towards higher wavenumber due to increment in the Ga content [3,4]. Further increasing the reaction time to 24h, significant difference was not observed. The observed CIGSe peak correspond to A_1 mode which arises due to vibration of Se atoms along with motionless neighbouring cations of Cu, In and Ga [2]. These results are good accordance with XRD results where we observed the formation of CIGSe through β-CuSe nuclei.

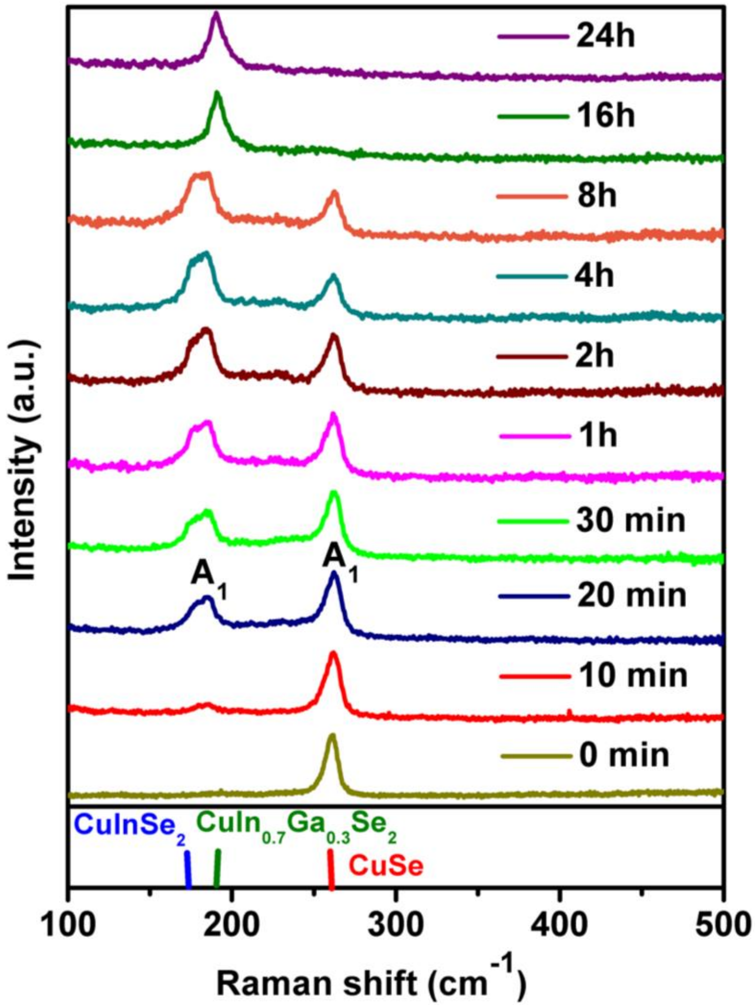

Fig. 6.8. Raman spectra of synthesized CIGSe samples at different reaction time.

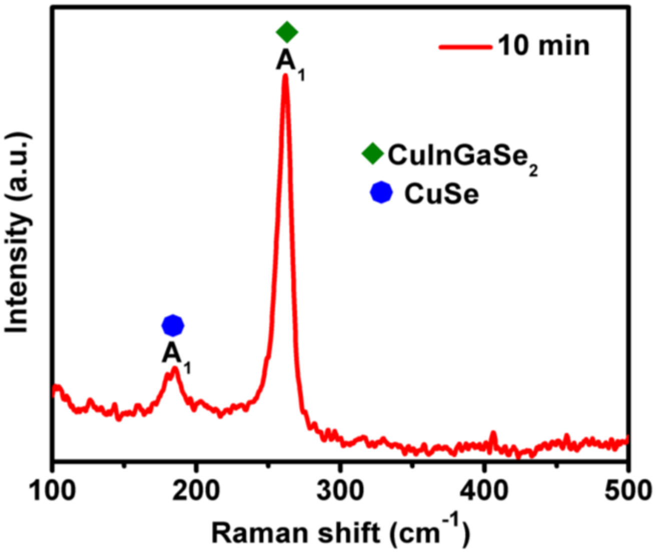

Fig. 6.9. Raman spectrum of synthesized CIGSe sample at 10 min of reaction time.

FE-SEM images of synthesized CIGSe samples at different reaction time are shown in **Fig. 6.10**. From the figure, it is clear that the nanoparticles size is increased from 10 to 48 nm with increasing the reaction time. Increases in the nanoparticles size could be due to Ostwald ripening **[10,11]**, in which the larger crystals grow at the expense of the dissolution of smaller crystals. EDS composition of CIGSe samples synthesized at different reaction time is shown in **Fig. 6.11(a)**. As the reaction time increases, Cu content decreased while Se content increased. When the reaction time was at 0 min, the In and Ga contents were not observed because this reaction time is not enough to realize Ga^{3+} and In^{3+} ions from the metal complex of OLA-Ga and OLA-In respectively. With increasing reaction time, In and Ga contents were gradually increased. The Cu/(In+Ga) and Ga/(In+Ga) ratios are shown in **Fig. 6.11(b)**. The Cu/(In+Ga) ratio decreased gradually while Ga/(In+Ga) ratio increased steadily. At 0 min, high Cu/(In+Ga) ratio was observed which is due to higher reactivity of Cu at lesser reaction time. By prolonging the reaction time, the reactivity of In and Ga were increased. These compositional changes leads to the formation of CIGSe with different composition as well as secondary phase of CuSe at less reaction time (<16h). The stoichiometric composition was observed at 16h. Thus, the structural and compositional analysis confirmed that the phase conversion occurs from CuSe to CIGSe.

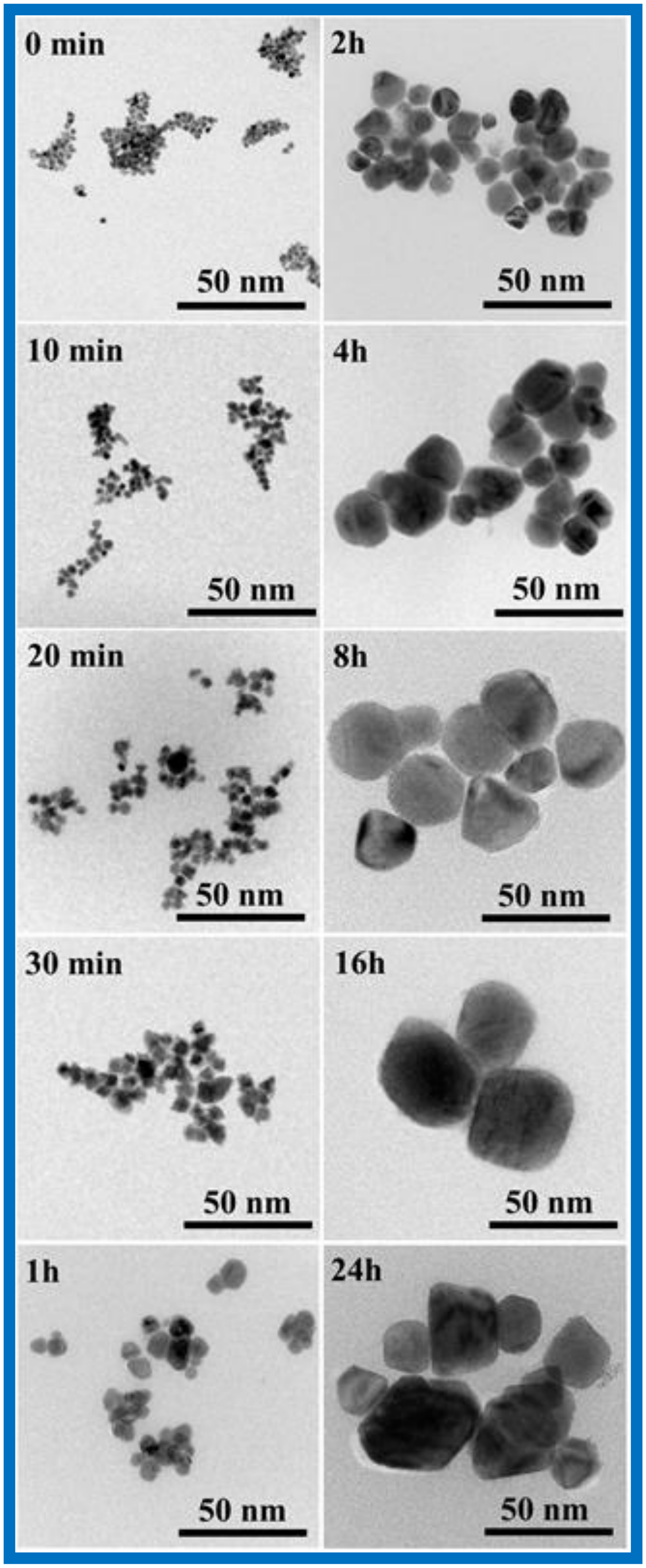

Fig. 6.10. TEM images of synthesized CIGSe samples at different reaction time.

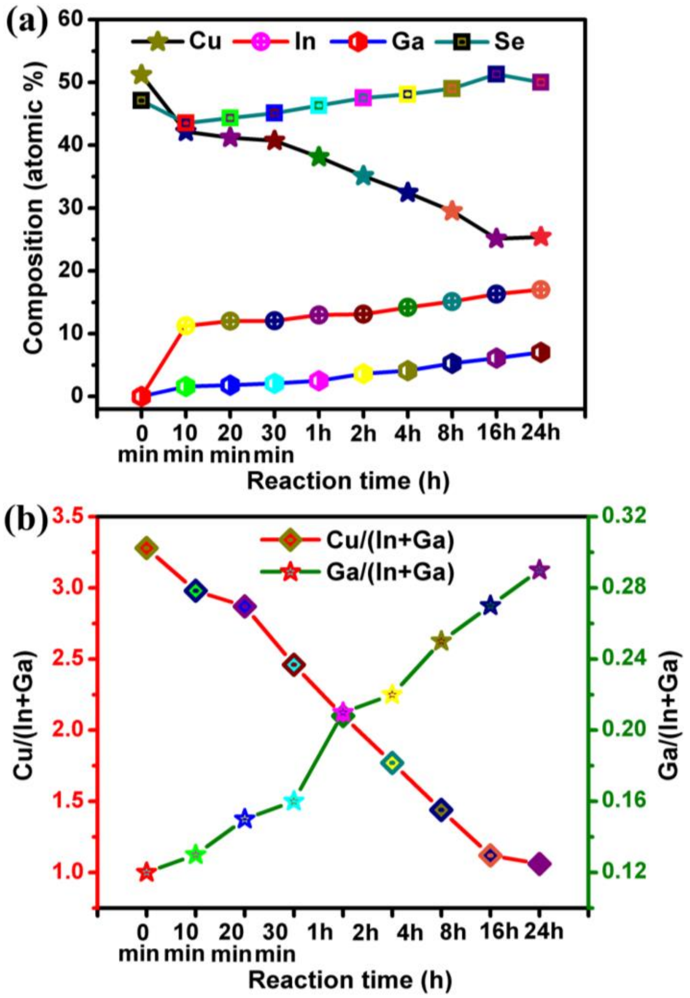

Fig. 6.11. (a) EDS composition of synthesized CIGSe samples at different reaction time and (b) corresponding Cu/(In+Ga) and Ga/(In+Ga) ratio.

FE-SEM-EDS elemental mapping of CIGSe sample synthesized at 180°C for 16h is shown in Fig. 6.12(a-e). The homogenous distribution of Cu, In, Ga and Se-elements in the nanoparticles without any segregation was observed from Fig. 6.12(b-e). The observed elemental composition of Cu:In:Ga:Se from the Fig. 6.12(f) is close to the targeted composition. The SAED pattern [Fig. 6.12(g)] showed the three diffraction rings and HR-TEM image [Fig. 6.12(h)] showed the interplanar d-spacing values of 3.31, 2.03 and 1.72 Å which correspond to (112), (220) and (312) planes of chalcopyrite CIGSe, [12] consistent with XRD analysis.

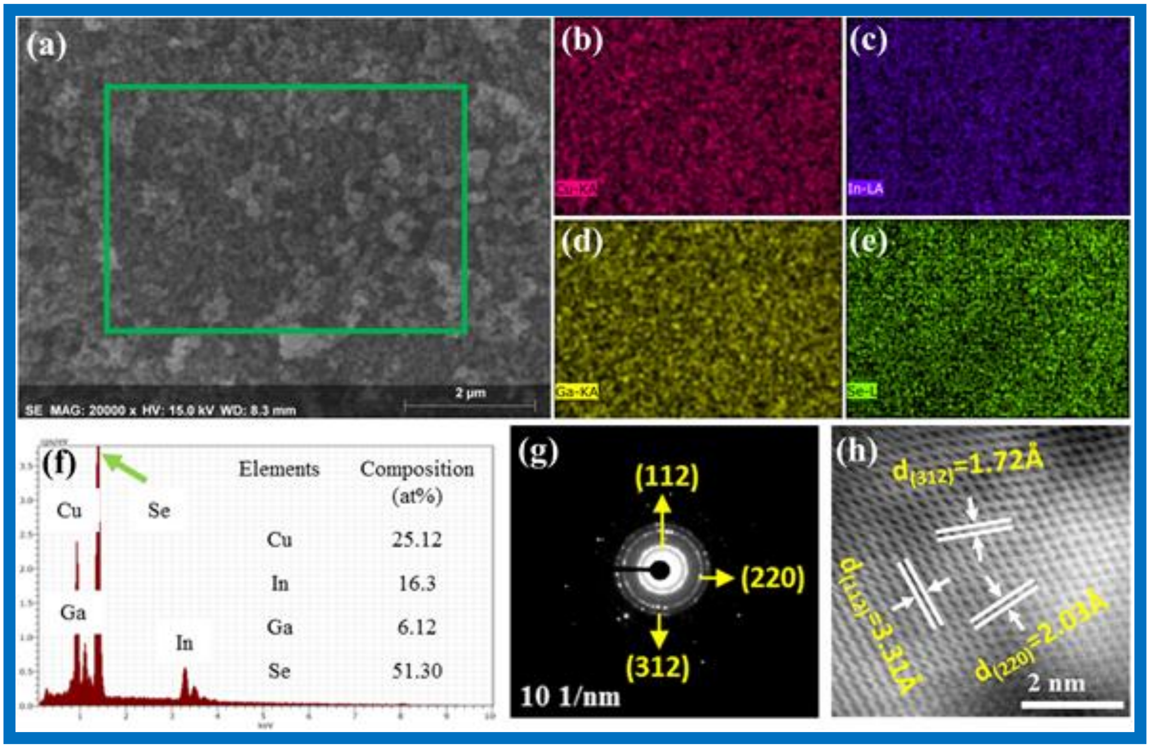

Elements	Composition (at%)
Cu	25.12
In	16.3
Ga	6.12
Se	51.30

Fig. 6.12. CIGSe sample synthesized at 180°C for 16h (a) FE-SEM micrograph, (b-e) EDS mapping, (f) EDS spectrum, (g) SAED pattern and (h) HR-TEM image.

Fig. 6.13(a) shows the UV-VIS-NIR absorption spectrum of CIGSe sample synthesized at 180°C for 16h. From the figure, the absorption started in the near infrared region and it increased gradually towards ultra violet visible region which is in good accordance with literature [4,13].

The optical bandgap energy was calculated using following formula:

$$(\alpha h\vartheta)^2 = \alpha(h\vartheta - Eg) - - - - \rightarrow (1)$$

where, α is a absorption co-efficient, $h\nu$ is the photon energy and E_g is the optical bandgap energy. The optical bandgap energy was calculated by extra plotting the linear plot of $(\alpha h\nu)^2$ versus hν as shown in Fig. 6.13(b). The obtained optical bandgap energy of 1.24 eV is an optimum value for CIGSe solar cell application [14]. The valence states of CIGSe sample synthesized at 180°C for 16h was examined by XPS analysis. Fig.

6.13(c) showed the Cu 2p spectrum in which two peaks were appeared at 932.7 and 952.5 eV, correspond to Cu $2p_{3/2}$ and Cu $2p_{1/2}$ respectively. The binding energies of In 3d were observed at 444.8 (In $3d_{5/2}$) and 953 (In $3d_{5/2}$) eV from the Fig. 6.13(d) [15]. For Ga 3d, two peaks were observed at 17.5 (In 4d) and 18.1 eV (Ga 3d). The binding energy of Se $3d^{5/2}$ and Se $3d^{3/2}$ were 54.7 and 54 eV respectively, which matches with selenium (Se 3d) in CIGSe [16].

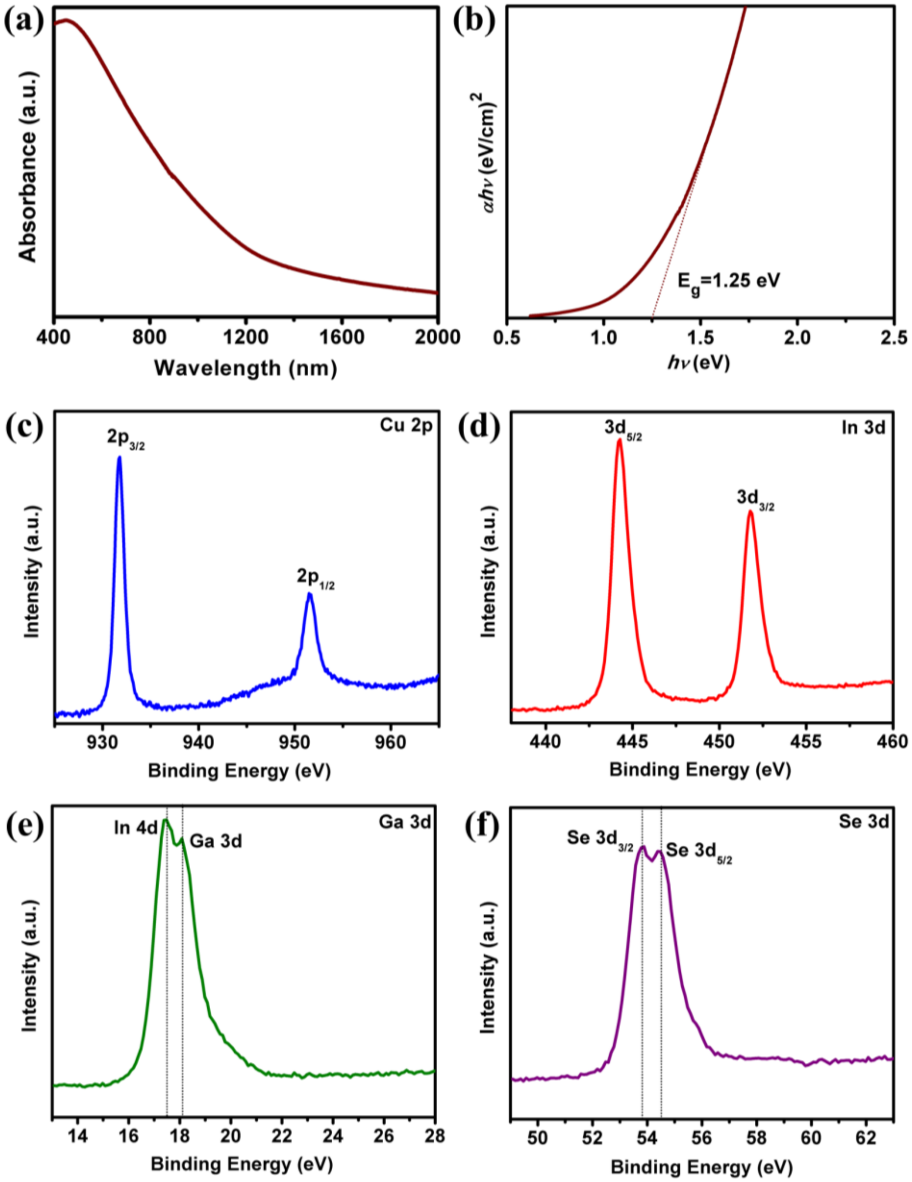

Fig. 6.13. CIGSe sample synthesized at 180°C for 16h (a) UV-VIS-NIR absorption spectrum, (b) corresponding band gap of hν versus $(\alpha h\nu)^2$ and (c-f) XPS spectra.

6.1.3. Formation mechanism of CIGSe

On the basis of above results, we proposed a possible growth mechanism of the CIGSe nanoparticles as illustrated in **Fig. 6.14**. The reaction pathway of phase pure CIGSe nanoparticles as following:

[1] *The formation of CuSe nuclei was observed.*
[2] *Then, mixed phase formation of CuSe and CIGSe was observed.*
[3] *Finally, formation of pure phase CIGSe nanoparticles was observed.*

→At 0 min, the β-CuSe phase formation was observed from the structural analysis **(Fig. 6.6 & 6.8)**. According to hard–soft acid–base model **[17]**, the soft base of Se reacted with a soft acid of Cu^+, instead of hard acids such as Ga^{3+} and In^{3+}, leading to the formation of β-CuSe at low temperature with less reaction time.

→As the reaction time increases from 10 min to 8h, the as-formed β-CuSe are subjected to inward diffusion of Ga^{3+} and In^{3+} ions and a partial outward diffusion of Cu^+ which leads to the formation of CIGSe **[7]**. Because of, Cu (I) ions in the CuSe have high mobility which can facilitate an exchange with other cations (Ga^{3+} and In^{3+}). Thus, the observed mixed phase of β-CuSe and CIGSe reveal that the incomplete reaction in this stage **(Fig. 6.6 & 6.8)**.

→When the reaction time above 8h, phase transformation occurs from β-CuSe to pure phase CIGSe which suggests that the longer reaction time provides more energy for cation inter diffusion and thus expel the starting phase β-CuSe.

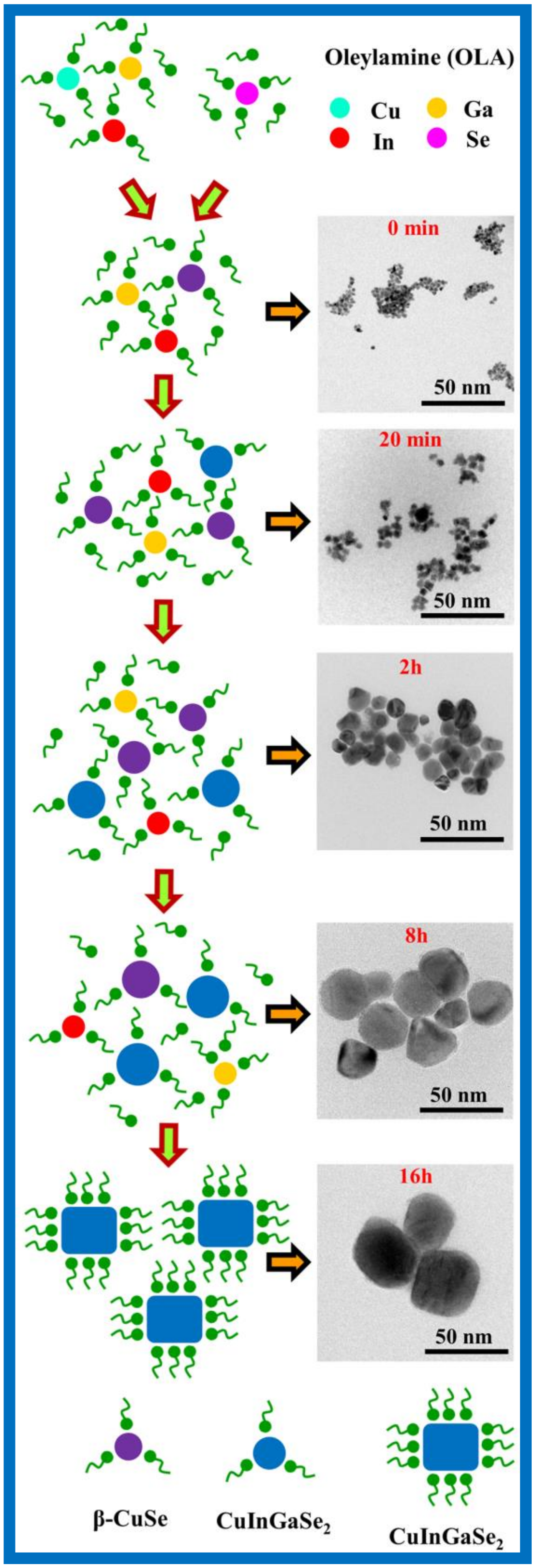

Fig. 6.14. Time dependent evolution pathway of CIGSe nanoparticles synthesized via hot injection process.

6.2. Deposition of CIGSe films

Based on the above results, we have chosen the CIGSe powder synthesized at 180°C-16h for further film deposition. The CIGSe ink was formulated by dispersing 50 mg of CIGSe powder in 500 μL hexanethiol (**chapter 5**). Then, the CIGSe ink was deposited onto SLG substrate by doctor blade method as mentioned in **chapter 3**.

6.2.1. Annealing and selenization of CIGSe films

Here, the temperature that we used for annealing and selenization are 350°C and 500°C respectively, which we already optimized in **chapter 5.** The prepared CIGSe film was annealed at 350°C (An-350°C) and selenized at 500°C (Se-500°C) and selenized with NaCl treatment at 500°C (Se-NaCl-500°C).

Fig. 6.15 shows the XRD pattern of CIGSe films. For all the samples, (112), (220) and (312) planes were observed which correspond to chalcopyrite crystal structure of CIGSe [**JCPDS 35-1102**]. The calculated FWHM for (112) plane were 0.340, 0.338 and 0.35° for An-350°C, Se-500°C and Se-NaCl-500°C respectively.

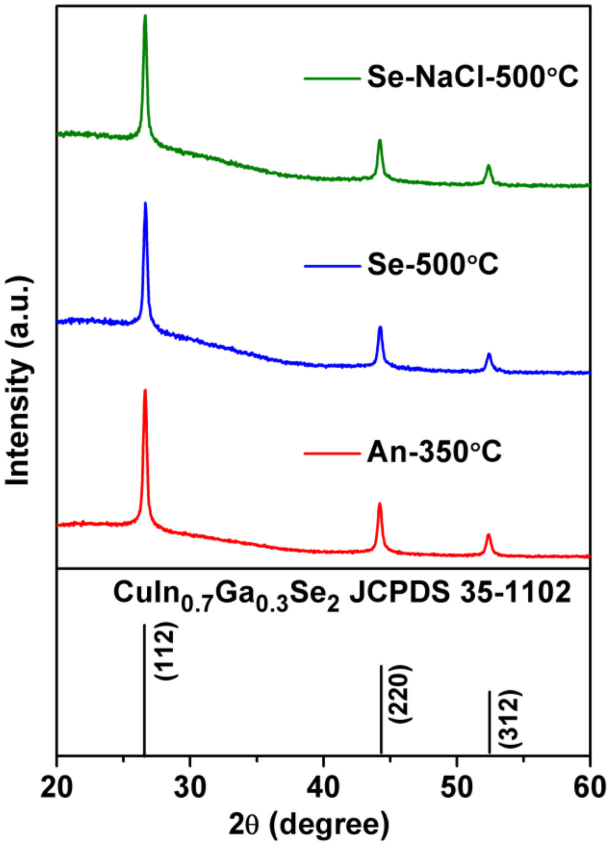

Fig. 6.15. XRD pattern of An-350^{o}C, Se-500^{o}C and Se-NaCl-500^{o}C CIGSe films.

The planar and cross sectional FE-SEM images of An-350^{0}C, Se-500^{0}C and Se-NaCl-500^{0}C films are shown in Fig. 6.16. All the films showed smooth surface with a few cracks and pin holes. After selenization, bigger grains were observed on the surface of the films with size ranging from 0.3 to 1 µm. The film annealed at 350^{0}C showed uniform film thickness of ~1.42 µm as can be seen from the cross sectional view of FE-SEM image. The film thickness was reduced from 1.42 to ~1 µm after selenization, due to evaporation of carbon and sulfur content as shown in Table 6.2. The film selenized with NaCl-treatment at 500^{0}C showed compact and densely packed grains.

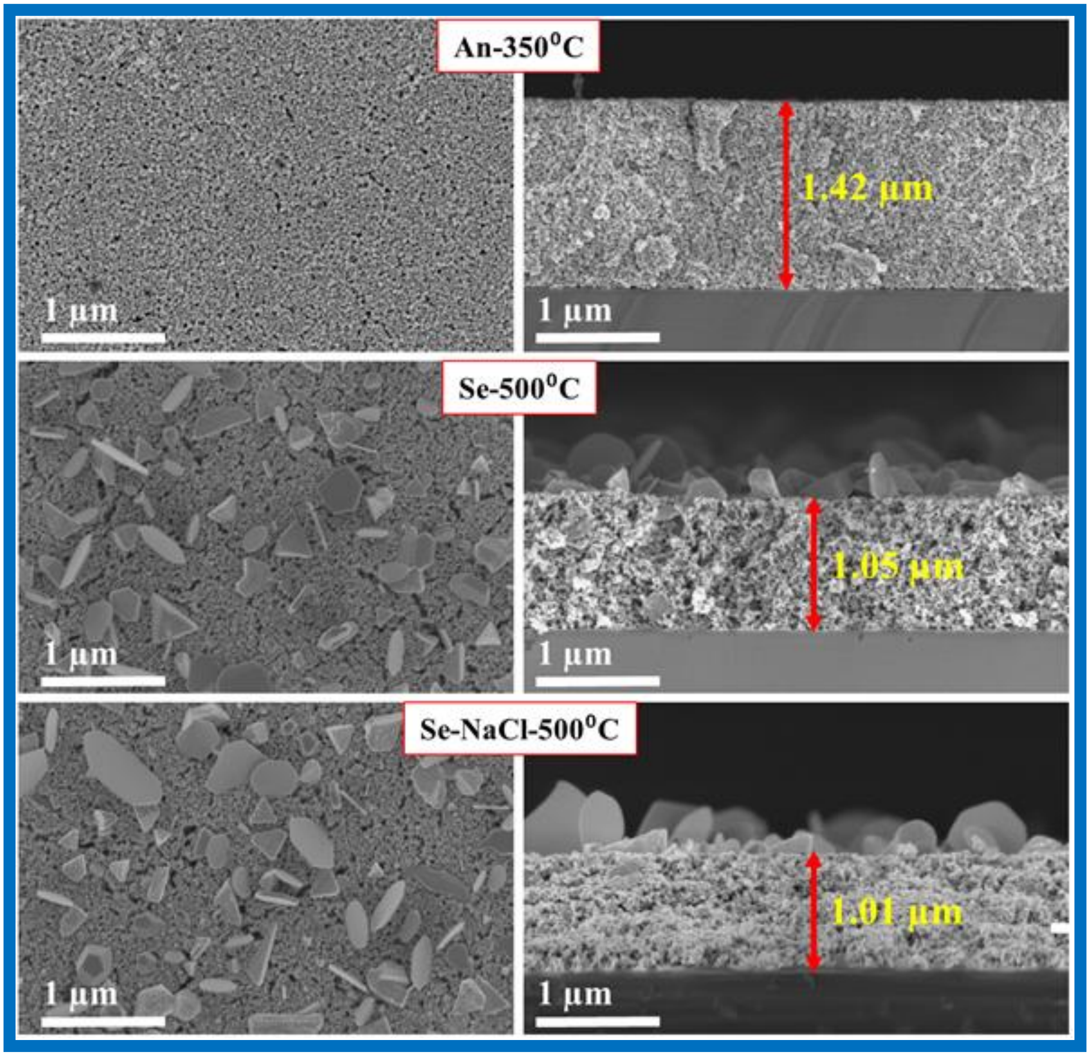

Fig. 6.16. Planar and cross sectional FE-SEM images of An-350°C, Se-500°C and Se-NaCl-500°C CIGSe films.

EDS composition of CIGSe films are shown in **Table 6.1**. The observed elemental composition and Cu/(In+Ga) and Ga/(In+Ga) ratio are very close to the powder, for all the samples. **Table 6.2** shows sulfur, sodium and carbon content in the CIGSe films. The film An-350°C showed less than 2 (at %) of sulfur content which is because of the solvent (hexanethiol) used for the ink formulation. After selenization, sulfur content was not detected by EDS and carbon content decreased from ~42 to 30 (at %). The observed sodium content was 0.32, 1.52 and 6.34 for An-350°C, Se-500°C and Se-NaCl-500°C films respectively. The high sodium content was observed for Se-NaCl-500^{0}C film because of NaCl treatment.

Table 6.1. EDS composition of CIGSe films.

Experimental conditions	**Composition (at %)**				**Cu/**	**Ga/**
	Cu	**In**	**Ga**	**Se**	**(In+Ga)**	**(In+Ga)**
An-350 ℃	25.13	18.79	6	46.08	1.01	0.24
Se-500 ℃	25.72	18.59	6.20	48.49	1.04	0.25
Se-NaCl-500 ℃	25.54	18.68	6.11	48.67	1.03	0.24

Table 6.2. Sulfur, sodium and carbon content in the CIGSe films.

Experimental conditions	**Sulfur (S) (at %)**	**Sodium (Na) (at %)**	**Carbon (C) (at %)**
An-350 ℃	1.78	0.32	42.01
Se-500 ℃	-	1.52	31.02
Se-NaCl-500 ℃	-	6.34	30.75

Fig. 6.17(a) shows the optical absorption spectra of CIGSe films. The absorption initiated in the near infra-red region and gradually increased towards UV-Visible region for all the CIGSe films **[14]**. The band gap was calculated using Tauc plot by extra plotting the hν versus $(\alpha h\nu)^2$ as shown in **Fig. 6.17(b)**. The obtained band gap of 1.17, 1.22 and 1.24 eV for An-350, Se-500 and Se-NaCl-500^{0}C respectively.

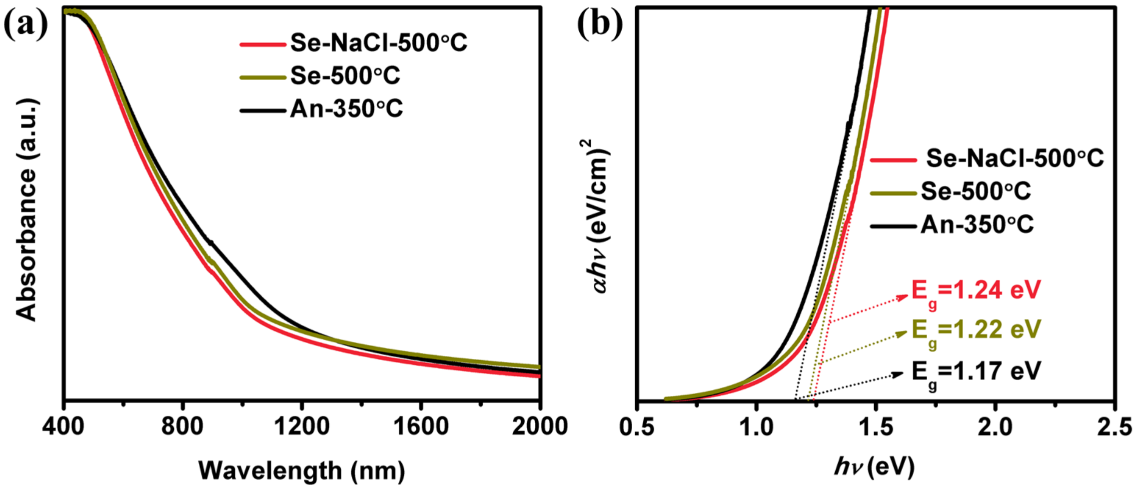

Fig. 6.17. (a) UV-VIS-NIR absorption spectra and (b) Band gap spectra of CIGSe films.

Table 6.3 shows the conductivity type, carrier concentration, mobility and resistivity of CIGSe films. All the CIGSe films showed P-type conductivity with the carrier concentration in the order between 10^{17} and 10^{18} cm^{-3}. The resistivity of CIGSe films decreased from 81 to 76 Ωcm after selenization. The mobility of CIGSe films were 0.18, 0.21 and 0.23 cm^2/Vs for An-350ºC, Se-500ºC, and Se-NaCl-500ºC, respectively. As we discussed in chapter 5, after selenization, the carrier concentration was increased which can be due to the enhancement in grain size as observed from the FE-SEM images [18]. Slightly, mobility increased and resistivity decreased after selenization. In this work, less mobility and high resistivity were observed as compared to the film prepared using submicron particles (one-pot heating-up method). Because, submicron particles showed densely packed large sized (~500 nm) grains which has less grain boundaries such a way that reduces the height of the potential barrier as we discussed in chapter 5 [19]. From the cross-sectional FE-SEM images (Fig. 6.16), it can be seen that, all the films consist of smaller grains (~50 nm) which contributes higher density of grain boundaries that act as barrier for the flow of charge carriers. This leads to higher resistivity and lower mobility of charge carriers [20].

Table 6.3. Conductivity type, carrier concentration, mobility and resistivity of CIGSe films.

Experimental conditions	Type of conductivity	Carrier concentration (cm^{-3})	Mobility (cm^2/Vs)	Resistivity (Ωcm)
An-350 ℃	P	1.42×10^{17}	0.18	81
Se-500 ℃	P	1.52×10^{17}	0.21	78
Se-NaCl-500 ℃	P	2.12×10^{18}	0.23	76

The photoconductivity measurement was performed as mentioned in **chapter 5**. I-V measurement of CIGSe films was done in dark and under an illumination of light is shown in **Fig. 6.18**. The calculated photoconductivity of An-350^{0}C, Se-500^{0}C, and Se-NaCl-500^{0}C films were 1.17, 1.23 and 1.30 fold, respectively. After selenization, CIGSe films showed slight improvement in the photoconductivity as compared to annealed film which could be due to minor increment in the grain size. In this work, all the films exhibited very less photocurrent (nA) than the films discussed in **Chapter 5**. This is due to the presence of smaller grains which leads to a high density of grain boundaries that can serve as recombination centers **[21]**.

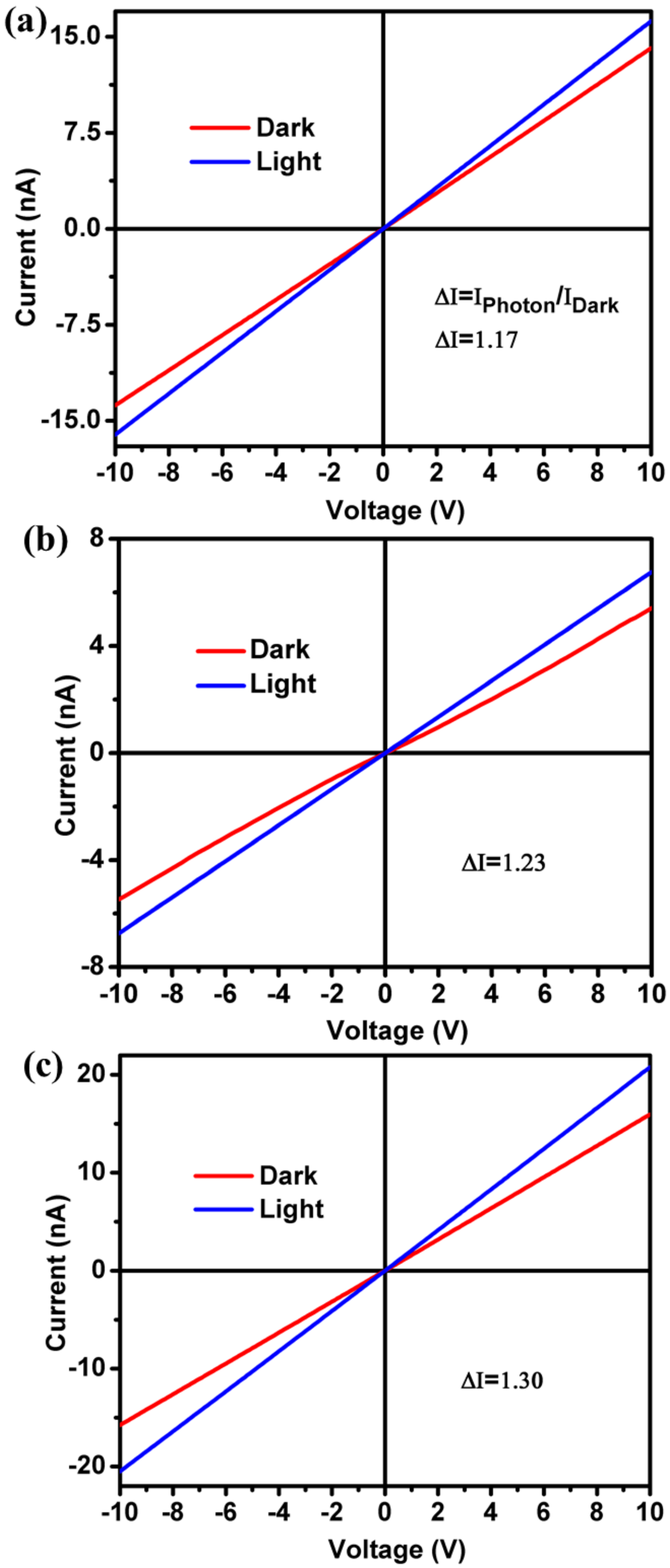

Fig. 6.18. I-V curve of CIGSe films (a) An-350^{0}C, (b) Se-500^{0}C and (c) Se-NaCl-500^{0}C.

6.3. Summary

- CIGSe nanoparticles were synthesized using metal chlorides and elemental selenium in presence of oleylamine at relatively low temperature by hot injection process. The effect of reaction parameters such as reaction temperature, reaction time on the formation of pure phase chalcopyrite CIGSe nanoparticles, with controlled stoichiometry composition were investigated. The formation mechanism of quaternary CIGSe was also studied.
- Initially, CIGSe nanoparticles were synthesized by varying the reaction temperature such as 260, 240, 220 and 200°C by keeping constant reaction time of 4h. As the reaction temperature decreases, CIGSe peaks were shifted to higher 2Θ values, which indicates an increment in the Ga content. In addition to that, β-CuSe phase observed for all the samples, which is due to Cu-rich composition. The crystallite size was decreased from 36.04 to 24.58 nm as the reaction temperature decreases. The irregular shape and inhomogeneous particle size distribution were observed which could be due to wide range of compositional distribution and multiphase formation. The particles sizes were decreased from 40 to 25 nm as the reaction temperature decreases due to decrement in the reactivity of precursor which might inhibit the growth of particles. With decreases in the reaction temperature, Cu/(In+Ga) ratio increased as Cu has higher reactivity at lower reaction temperature. When the reaction temperature was >200°C, the Ga-poor composition observed which is due to the evaporation of Ga.
- Next, the aliquots were withdrawn at regular interval from 0 min to 24h at 180^{0}C to study the growth and formation mechanism of CIGSe nanoparticles. At 0 min, formation of orthorhombic crystal structure of β-CuSe phase was observed. As the reaction time increases up to 8h, mixed phase formation of β-CuSe and CIGSe were observed. Further increasing the reaction time to 16h, formation of pure phase CIGSe was obtained. These results confirmed that the β-CuSe is acted as a seed to form the pure phase CIGSe. The nanoparticles size increased from 10 to 48 nm with increasing the reaction time due to Ostwald ripening. The In and Ga contents were not observed at 0 min, because this reaction time is not enough to realize Ga^{3+} and

In^{3+} ions from the metal complex of OLA-Ga and OLA-In respectively. As the reaction time increases, the In and Ga contents were gradually increased. Finally, stoichiometric composition of CIGSe was obtained at 16h. FE-SEM-EDS elemental mapping of CIGSe powder synthesized at 180°C for 16h showed the homogenous distribution of Cu, In, Ga and Se in the nanoparticles without any segregation. The SAED pattern showed three diffraction rings and HR-TEM image showed the interplanar d-spacing values of 3.31, 2.03 and 1.72 Å, correspond to (112), (220) and (312) planes of chalcopyrite CIGSe which further confirms the phase purity of CIGSe. The CIGSe nanoparticles synthesized at 180°C for 16h showed the optical bandgap energy of 1.24 eV. The valence states of CIGSe nanoparticles synthesized at 180°C for 16h was examined by XPS analysis. Reaction pathway was evaluated for pure phase CIGSe, which is initiated from binary β-CuSe and then subsequently transferred to CIGSe by gradual incorporation of In^{3+} and Ga^{3+} ions into the β-CuSe crystal lattice.

- ✓ Furthermore, CIGSe nanoparticles synthesized at 180°C for 16h were used for film preparation. Ink was formulated by dispersing 50 mg of CIGSe powder in 500 μL hexanethiol. Subsequently, the ink was coated as a film onto SLG substrate and annealed at 350°C under atmospheric condition for 1 min. Afterwards, the films were selenized at 500°C for 20 mins with and without NaCl treatment. All the films showed the (112), (220) and (312) planes which correspond to chalcopyrite crystal structure of CIGSe. The FWHM for (112) plane decreased from 0.340, 0.338 and 0.335^0 after selenization. All the films showed smooth surface with few cracks and pin holes. The selenized films showed bigger grains on the surface of the films with size ranging from 0.3 to 1 μm. The film thickness was reduced from 1.42 to ~1 μm after selenization due to the evaporation of carbon and sulfur content. The observed elemental composition of Cu:In:Ga:Se were close to the powder. After selenization, the carbon content decreased from ~42 to 30 (at %). The high sodium content was observed for Se-NaCl-500^0C film because of NaCl treatment.
- ✓ All the films showed nearly similar bandgap of 1.25 eV which could be due to similar composition. All the films showed P-type conductivity with carrier concentration in the order between 10^{17} and 10^{18} cm^{-3}. All the films showed higher

resistivity and lower mobility. From the cross-sectional FE-SEM images, it can be seen that, all the films consist of smaller grains (~50 nm) which contributes to higher density of grain boundaries that act as barrier for the flow of charge carriers. This leads to higher resistivity and lower mobility of charge carriers. The calculated photoconductivity of An-350^{0}C, Se-500^{0}C, and Se-NaCl-500^{0}C films were 1.17, 1.23 and 1.30 fold, respectively. The observed less photoconductivity is due to the presence of smaller grains, leading to a high density of grain boundaries that can serve as recombination centres.

References

[1] A. Monshi, M.R. Foroughi, M.R. Monshi, Modified Scherrer equation to estimate more accurately nano-crystallite size using XRD, World J. Nano Sci. Eng. 2 (2012) 154. doi:10.4236/wjnse.2012.23020.

[2] J. Liu, D.M. Zhuang, M.J. Cao, C.Y. Wang, M. Xie, X.L. Li, Preparation and characterization of Cu(In,Ga)Se_2 thin films by selenization of $Cu_{0.8}Ga_{0.2}$ and In_2Se_3 precursor films, Int. J. Photoenergy. 2012 (2012). doi:10.1155/2012/149210.

[3] M. Latha, R.A. Devi, S. Velumani, G. Oza, P. Reyes-Figueroa, M. Rohini, I.G. Becerril-Juarez, J. Yi, Synthesis of $CuIn_{1-x}Ga_xSe_2$ Nanoparticles by Thermal Decomposition Method with Tunable Ga Content, J. Nanosci. Nanotechnol. 15 (2015) 8388–8394. doi:10.1166/jnn.2015.11473.

[4] J. Li, Z. Jin, T. Liu, J. Wang, D. Wang, J. Lai, H. Du, L. Cui, Ternary and quaternary chalcopyrite $Cu(In_{1-x}Ga_x)Se_2$ nanocrystals: organoalkali-assisted diethylene glycol solution synthesis and band-gap tuning, CrystEngComm. 15 (2013) 7327. doi:10.1039/c3ce40813b.

[5] V. Izquierdo-Roca, X. Fontané, E. Saucedo, J.S. Jaime-Ferrer, J. Álvarez-García, A. Pérez-Rodríguez, V. Bermudez, J.R. Morante, Process monitoring of chalcopyrite photovoltaic technologies by Raman spectroscopy: an application to low cost electrodeposition based processes, New J. Chem. 35 (2011) 453. doi:10.1039/c0nj00794c.

[6] O. Arellano-Tánori, M.C. Acosta-Enríquez, R. Ochoa-Landín, R. Iñiguez-Palomares, T. Mendívil-Reynoso, M. Flores-Acosta, S.J. Castillo, Copper-selenide and copper-telluride composites powders sintetized by ionic exchange, Chalcogenide Lett. 11 (2014) 13–19.

[7] E. Dilena, Y. Xie, R. Brescia, M. Prato, L. Maserati, R. Krahne, A. Paolella, G. Bertoni, M. Povia, I. Moreels, L. Manna, $CuIn_xGa_{1-x}S_2$ nanocrystals with tunable composition and band gap synthesized via a phosphine-free and scalable procedure, Chem. Mater. 25 (2013) 3180–3187. doi:10.1021/cm401563u.

[8] https://en.wikipedia.org/wiki/Gallium_trichloride.

[9] Y. Xie, X. Zheng, X. Jiang, J. Lu, L. Zhu, Sonochemical synthesis and

mechanistic study of copper selenides $Cu_{(2-x)}Se$, beta-CuSe, and Cu_3Se_2., Inorg. Chem. 41 (2002) 387–392. doi:Doi 10.1021/Ic010108v.

[10] W. Wang, H. Shen, X. He, Study on the synthesis and formation mechanism of Cu_2ZnSnS_4 particles by microwave irradiation, Materials Research Bulletin 48 (2013) 3140–3143. doi: S0025540813003516.

[11] S. Ahn, K. Kim, Y. Chun, K. Yoon, Nucleation and growth of Cu(In,Ga)Se_2 nanoparticles in low temperature colloidal process, Thin Solid Films. 515 (2007) 4036–4040. doi:10.1016/j.tsf.2006.10.102.

[12] S.N. Malik, S. Mahboob, N. Haider, M. a Malik, P. O'Brien, A colloidal synthesis of $CuInSe_2$, $CuGaSe_2$ and $CuIn_{1-x}Ga_xSe_2$ nanoparticles from diisopropyldiselenophosphinatometal precursors, Nanoscale. 3 (2011) 5132–5139. doi:10.1039/c1nr10888c.

[13] M. Ahmadi, S.S. Pramana, L. Xi, C. Boothroyd, Y.M. Lam, S. Mhaisalkar, Evolution pathway of CIGSe nanocrystals for solar cell applications, J. Phys. Chem. C. 116 (2012) 8202–8209. doi:10.1021/jp300187r.

[14] A. Chirilă, S. Buecheler, F. Pianezzi, P. Bloesch, C. Gretener, A.R. Uhl, C. Fella, L. Kranz, J. Perrenoud, S. Seyrling, R. Verma, S. Nishiwaki, Y.E. Romanyuk, G. Bilger, A.N. Tiwari, Highly efficient Cu(In,Ga)Se_2 solar cells grown on flexible polymer films., Nat. Mater. 10 (2011) 857–861. doi:10.1038/nmat3122.

[15] C. Calderón, P. Bartolo-Pérez, O. Rodríguez, G. Gordillo, Phase identification and XPS studies of Cu(In,Ga)Se_2 thin films, Microelectronics J. 39 (2008) 1324–1326. doi:10.1016/j.mejo.2008.01.071.

[16] C. Platzer-Björkman, P. Zabierowski, J. Pettersson, T. Törndahl, M. Edoff, Improved fill factor and open circuit voltage by crystalline selenium at the Cu(In,Ga)Se_2/buffer layer interface in thin film solar cells, Prog. Photovoltaics Res. Appl. 18 (2010) 249–256. doi:10.1002/pip.957.

[17] R.G. Pearson, Hard and Soft Acids and Bases, Journalof Am. Chem. Soc. 85 (1963) 3533–3539. doi:10.1021/ja00905a001.

[18] M.G. Tsai, H.T. Tung, I.G. Chen, C.C. Chen, Y.F. Wu, X.D. Qi, Y. Hwu, C.Y. Lin, P.H. Wu, C.W. Cheng, Annealing Effect on the Properties of $Cu(In_{0.7}Ga_{0.3})Se_2$ Thin Films Grown by Femtosecond Pulsed Laser Deposition, J.

Am. Ceram. Soc. 96 (2013) 2419–2423. doi:10.1111/jace.12422.

[19] P.K. Mishra, V. Dave, R. Chandra, J.N. Prasad, A.K. Choudhary, Effect of processing parameter on structural, optical and electrical properties of photovoltaic chalcogenide nanostructured RF magnetron sputtered thin absorbing films, Mater. Sci. Semicond. Process. 25 (2014) 307–319. doi:10.1016/j.mssp.2014.01.021.

[20] D. Bhattacharyya, S. Chaudhuri, A.K. Pal, Electrical conduction at low temperatures and ZnTe films, Mater. Chem. Phys. 584 (1995).

[21] M.G. Panthani, V. Akhavan, B. Goodfellow, J.P. Schmidtke, L. Dunn, A. Dodabalapur, P.F. Barbara, B. a. Korgel, Synthesis of $CuInS_2$, $CuInSe_2$, and $Cu(In_xGa_{1-x})Se_2$ (CIGS) nanocrystal “inks” for printable photovoltaics, J. Am. Chem. Soc. 130 (2008) 16770–16777. doi:10.1021/ja805845q.

Chapter 7

Conclusions

This thesis is devoted towards a synthesis of pure phase CIGSe submicron and nanoparticles by chemical techniques, followed by preparation of films using cost-effective deposition method.

- The CIGSe submicron and nanoparticles were successfully synthesized by using one-pot heating up and hot injection process, respectively. The CIGSe films were deposited by doctor blade method. The selenization process was carried out to improve the properties of as-prepared films. All the CIGSe films exhibited unique chalcopyrite phase. The structural, morphological and compositional properties of all the CIGSe films were investigated. The CIGSe film deposited from submicron particles exhibited improved structural, morphological, electrical and opto electronic properties as compared to nanoparticles.

- One of the prime objective of this thesis is to synthesis single phase CIGSe submicron particles by using one-pot heating-up process. It was successfully achieved by optimization of reaction parameters such as reaction temperature and time. The various properties of synthesized CIGSe submicron particles were investigated by XRD, Raman, FE-SEM, EDS and UV-VIS-NIR analysis. The obtained results are as follows:

    - With increases in the reaction temperature, Ga-poor samples were obtained.
    - The incorporation of Ga was strongly influenced by reaction time.
    - The formation mechanism of pure phase CIGSe was investigated, which was initiated from binary β-CuSe and then subsequently transferred to CIGSe by gradual incorporation of In^{3+} and Ga^{3+} ions into the β-CuSe crystal lattice.

  - Large-scale CIGSe synthesis was performed using the small scale procedure by increasing the amount of precursors to 10-fold. The ~2 gram CIGSe powder was successfully synthesized while maintaining control over the phase, composition, band gap energy, particle size, and morphology.
  - The influence of Cu concentration on the various properties of CIGSe particles was investigated. The Cu concentration has great impact on phase formation, particle size, particles morphology and optical band gap energy.

- The second objective of this thesis is the preparation of CIGSe films using submicron particles ink. The CIGSe films were successfully prepared by doctor blade method and physical properties of films were investigated.

  - The CIGSe powder concentration was varied during ink formulation to achieve crack free films with the thickness of ~1 μm.
  - The as-prepared CIGSe films were subjected to annealing at 350 and 400°C in ambient atmosphere to remove the organic solvent, followed by heat treatment at 500°C under Se atmosphere (Selenization) to enhance the grain growth.
  - The cracks were increased as the annealing temperature increases, due to stress generated in the film.
  - The selenization process was carried out for the CIGSe films annealed at 350°C in air. The influence of selenization temperature on the structural, morphological and compositional properties of CIGSe films were investigated. The thickness of the CIGSe film decreased because of evaporation of carbon. From the structural analysis, increment in the crystallite size observed as the selenization temperature increases. When the selenization temperature exceeds above 500°C, the cracks were appeared due to stress. After selenization, carbon content in the CIGSe film decreased from 42 (annealed) to 30 at %.

- Before selenization, the NaCl treatment was applied for annealed CIGSe films at 350°C in air. The NaCl treated CIGSe films showed increment in the grain size. The CIGSe films exhibited decreases in the resistivity and increases in the carrier concentration by one order magnitude. Also, it showed good photo response property nearly 4.39-fold. We conclude that CIGSe films selenized with NaCl treatment showed better crystallinity, electrical and opto electronic properties.

* The other important objective of this work is dedicated towards synthesis of CIGSe nanoparticles by hot injection process followed by preparation of films.

- The pure phase CIGSe nanoparticles were successfully synthesized by optimizing reaction temperature and time.
- The mixed phase of CIGSe and CuSe were observed for all the reaction temperature due to Cu-rich composition. With increases in the reaction temperature, the Ga poor samples were obtained due to evaporation of Ga.
- The formation mechanism of pure phase CIGSe nanoparticles were studied by gradual incorporation of Ga^{3+} and In^{3+} ions into the β-CuSe crystal lattice.
- The CIGSe films were prepared using nanoparticles ink and annealed at 350°C in air. Subsequently, these films were selenized at 500°C. After selenization, carbon content decreased from 42 to 30 at % which led to reduce the film thickness. Bigger grains was observed on the surface of the films. The optical, electrical and optoelectronic properties were almost similar in all the CIGSe films.
- We conclude that electrical and opto-electronic properties of CIGSe films made from nanoparticles were inferior due to smaller sized grains and pinholes.

Scope for future work

The present thesis work is dedicated towards preparation of CIGSe films from submicron and nanoparticles solution. The CIGSe films prepared from submicron particles showed superior properties than nanoparticles. Based on the results, the important issues in the nanoparticles based CIGSe films such as (i) presence of pores (ii), smaller sized grains. The following technical facts could favour the improvement of the CIGSe absorber layer properties.

- Deposition of CIGSe on Mo substrate and optimizing the selenization process.
- Deposition of hybrid layers of CIGSe films under Cu-poor and Cu-rich composition.
- Selenization of CIGS films.

Suggested hybrid CIGSe absorber layer

One way to enhance the grain growth in the CIGSe absorber layer, hybrid absorber can be prepared using Cu-poor and Cu-rich composition as illustrated in **Fig. 7.1**.

Fig. 7.1. Hybrid CIGSe absorber layer.

Selenization of CIGS absorber layer

The selenization of CIGS layer could increase the grain growth and eliminate the pores in the absorber layer as shown in **Fig. 7.2**.

Fig. 7.2. Selenization of CIGS absorber layer.

Publications and conference presentations

Publications

Peer-reviewed journals

1. **M. Latha**, R. Aruna Devi, S. Velumani, Goldie Oza, P. Reyes-Figueroa, M. Rohini, I. G. Becerril-Juarez, and Junsin Yi "Synthesis of $CuIn_{1-x}Ga_xSe_2$ Nanoparticles by Thermal Decomposition Method with Tunable Ga Content" ***Journal of Nanoscience and Nanotechnology*** 15 **(2015)** 8388–8394.
2. R. Aruna Devi, **M. Latha**, S. Velumani, Goldie Oza, P. Reyes-Figueroa, M. Rohini, I. G. Becerril-Juarez, Jae-Hyeong Lee and Junsin Yi "Synthesis and characterization of cadmium sulfide nanoparticles by chemical precipitation method" ***Journal of Nanoscience and Nanotechnology*** 15 **(2015)** 8434–8439.
3. M. Rohini, P. Reyes, S. Velumani, **M. Latha**, Goldie Oza, I. Becerril-Juarez, R. Asomoza "Parametric optimization of Mechanochemical process for synthesis of $Cu(In,Ga)_{0.5}Se_2$ nanoparticles" ***Materials Science in Semiconductor Processing*** 37 **(2015)** 151–158.

Conference publications

1. **M. Latha**, R. Aruna Devi, P. Reyes-Figueroa, M. Rohini, S. Velumani, Adolfo Tavira Fuentes, Miguel Galván Arellano and F. Javier Ramírez Aponte "Influence of Reaction Time on $Cu(In,Ga)Se_2$ Particles Synthesis by Thermal Decomposition Method". 10.1109/ICEEE.2016.7751251.

2. R. Aruna Devi, **M. Latha**, P. Reyes-Figueroa, M. Rohini, S. Velumani, Adolfo Tavira Fuentes, Miguel Galván Arellano F. Javier Ramírez Aponte and Jaime Santoyo-Salazar "Facile One Pot Synthesis of Single Phase Kesterite Cu_2ZnSnS_4 Nanocrystals" 10.1109/ICEEE.2016.7751250.

Articles under preparation

1. **M. Latha**, R. Aruna Devi and S. Velumani "Influence of Cu concentration on the properties of solution processed $Cu(In,Ga)Se_2$ particles".
2. **M. Latha**, R. Aruna Devi and S. Velumani "Scalable synthesis of quaternary $Cu(In,Ga)Se_2$ submicron flakes with composition control and morphology change".
3. **M. Latha**, R. Aruna Devi, S. Velumani, F. A. Pulgarín Agudelo, O. Vigil-Galán and José Á. Chávez "Influence of heat treatment on the CIGSe films prepared using submicron particles".
4. **M. Latha**, R. Aruna Devi, S. Velumani, J. Santoyo-Salazar "Low temperature synthesis of quaternary $Cu(In,Ga)Se_2$ nanoparticles".

Conferences

Oral and poster presentations

1. **M. Latha**, R. Aruna Devi and S. Velumani "Influence of Cu Concentration on the Optical Properties of $Cu(In,Ga)Se_2$ Nanoparticles**"** MRS FALL MEETING & EXHIBIT, November 27 - December 2, 2016, Boston, Massachusetts. **(Oral)**

2. **M. Latha**, R. Aruna Devi and S. Velumani **"**Solution-Based Synthesis of $Cu(In_{1-x}Ga_x)Se_2$ Nanocrystals with Tunable Optical Properties**"** MRS FALL MEETING & EXHIBIT, November 27 - December 2, 2016, Boston, Massachusetts. **(Poster)**

3. **M. Latha**, R. Aruna Devi, P. Reyes-Figueroa, M. Rohini, S. Velumani, Adolfo Tavira Fuentes, Miguel Galván Arellano and F. Javier Ramírez Aponte "Influence of Reaction Time on $Cu(In,Ga)Se_2$ Particles Synthesis by Thermal Decomposition Method" 13th International conference on Electrical Engineering, Computing

Science and Automatic Control, September 26-30 2016, Mexico City, Mexico. **(Oral)**

4. **M. Latha**, R. Aruna Devi, P. Reyes-Figueroa, M. Rohini, Goldie Oza and S. Velumani "SELENIZATION OF DOCTOR BLADED Cu(In,Ga)Se_2 THIN FILMS USING SUBMICRON PARTICLES FOR SOLAR CELL APPLICATIONS" XXV International Materials Research Congress, IMRC 2016 August 14-19, Cancun, Mexico. **(Oral)**
5. **M. Latha**, R. Aruna Devi, P. Reyes-Figueroa, M. Rohini, Goldie Oza and S. Velumani "FACILE ONE POT SYNTHESIS OF Cu(In,Ga)Se_2 SUBMICRON PARTICLES: INFLUENCE OF Cu CONCENTRATIONS" XXV International Materials Research Congress, IMRC 2016 August 14-19, Cancun, Mexico. **(Poster)**
6. **M. Latha**, R. Aruna Devi, P. Reyes-Figueroa, M. Rohini, , Goldie Oza and S. Velumani "SYNTHESIS OF $CuIn_{1-x}Ga_xSe_2$ NANOSTRUCTURES BY THERMAL DECOMPOSITION METHOD WITH TUNABLE OPTICAL PROPERTIES" XXIV International Materials Research Congress, IMRC 2015 August 16-20, Cancun, Mexico. **(Oral)**
7. **M. Latha**, R. Aruna Devi, P. Reyes-Figueroa, M. Rohini, Goldie Oza and S. Velumani "ONE-POT SYNTHESIS OF $CuInSe_2$ NANOSTRUCTURES FOR SOLAR CELL APPLICATIONS" XXIV International Materials Research Congress, IMRC 2015 August 16-20, Cancun, Mexico. **(Poster)**
8. **M. Latha**, R.Aruna Devi, S. Velumani, I.G. Becerril-Juarez, Hyoensik Park and Junsin Yi "FORMATION MECHANISM OF $CuIn_{0.7}Ga_{0.3}Se_2$ NANOPARTICLES BY THERMAL DECOMPOSITION METHOD" Global Photovoltaic Conference, International Symposium on Photovoltaics (ISP 2014) November 10-11, BEXCO, Busan, Korea. **(Poster)**
9. **M. Latha**, R.Aruna Devi, S. Velumani, I.G. Becerril-Juarez, R. Asomoza and Junsin Yi "TIME-DEPENDENT CIGS NANOPARTICLE SYNTHESIS BY HOT INJECTION METHOD FOR SOLAR CELL APPLICATIONS" XXIII International Materials Research Congress, IMRC 2014, August 17-21, Cancun, Mexico. **(Poster)**

10. **M. Latha**, R.Aruna Devi, S. Velumani, I.G. Becerril-Juarez, R. Asomoza and Junsin Yi " IMPACT OF TEMPERATURE ON CIGS NANOPARTICLE SYNTHESIS BY HOT INJECTION METHOD FOR SOLAR CELL APPLICATIONS" XXIII International Materials Research Congress, IMRC 2014, August 17-21, Cancun, Mexico. **(Oral)**
11. **M. Latha**, Seunghwan Lee, Duy Phong Pham, R.Aruna Devi, S. Velumani and I.G. Becerril-Juarez "SYNTHESIS AND CHARACTERIZATION OF CIGS NANOPARTICLES BY HOT INJECTION METHOD FOR SOLAR CELL APPLICATIONS" International Conference on Microelectronics and Plasma Technology, ICMAP 2014, July 8-11, Gunsan, Korea. **(Poster)**
12. **M. Latha,** S. Velumani, M. Rohini, Ignacio G Becerril, R. Asomoza "SYNTHESIS AND CHARACTERIZATION OF CIGS NANOPARTICLES BY CHEMICAL METHOD FOR SOLAR CELL APPLICATION" XXII International Materials Research Congress, IMRC 2013, August 11-15, Cancun, Mexico. **(Poster)**